SIMULATION OF STRONG EARTHQUAKE MOTION WITH CONTAINED-EXPLOSION LINE SOURCE ARRAYS

Single-Source and Array Tests at Camp Parks

Final Report

December 1979

By: J. R. Bruce
    H. E. Lindberg
    G. R. Abrahamson

SRI International
333 Ravenswood Avenue
Menlo Park, California 94025
(415) 326-6200
Cable: SRI INTL MPK
TWX: 910-373-1246

EAS INFORMATION RESOURCES
NATIONAL SCIENCE FOUNDATION

SIMULATION OF STRONG EARTHQUAKE MOTION WITH CONTAINED-EXPLOSION LINE SOURCE ARRAYS

Single-Source and Array Tests at Camp Parks

Final Report

December 1979

By: J. R. Bruce
    H. E. Lindberg
    G. R. Abrahamson

Endorsement
Co-Principal
Investigator

G. R. ABRAHAMSON

Director, Poulter Laboratory

Endorsement
Co-Principal
Investigator

H. E. LINDBERG

Staff Scientist

iA

INTENTIONALLY BLANK

ii

ABSTRACT

This report describes the second year of an NSF-sponsored program to develop a technique which uses explosives to simulate strong level, earthquake-like ground motion. The long range objective is in-situ testing of soil-structure interaction and of structures with complex internal equipment systems. The technique will be applicable to buildings, nuclear reactors, pipelines, power lines, dams, bridges and tunnels.

The technique produces ground motion by simultaneous firing of a planar array of vertical line sources. The controlled release of high-pressure explosion products within each source allows controlled pressurization of the surrounding soil. In this way, both the amplitude and frequency content are controlled at levels suitable for testing with the array close to the test structure. This opens the possibility of in-situ testing at high levels of ground motion with a minimum of explosive and with little disturbance to the surroundings.

During this year, tests were performed with an array of ten 1/3-scale sources. Tests were also performed with single sources, both in 1/3 scale and full scale. A quasistatic theory was developed to predict both single source and array response. The 1/3-scale array test results, when compared to 1/3-scale single source test results, showed a more than order magnitude increase in ground motion. The quasistatic theory predicted this result and compared favorably with both the single-source and array tests. Extrapolation of these results to full scale showed an 80 x 40 ft array can produce accelerations of 0.6 g, velocities of 1 ft/s, and displacements of about 1 in. at frequencies of 3 to 5 hz, a useful level of ground motion for structural testing.

In a new two-year program proposed to begin in early 1980, tests are planned with a full-scale array. The ability to produce multiple detonations within each source will be added. By the end of the program, the entire array will be tested in a 3-pulse-per-test mode. A 30 x 30 ft test area will be available for structural testing during the program.

INTENTIONALLY BLANK

iv

CONTENTS

ILLUSTRATIONS

ILLUSTRATIONS (continued)

ix

ILLUSTRATIONS (continued)

TABLES

I INTRODUCTION AND SUMMARY

A. Background and Need

The need for an in-situ test technique to aid in the design of earthquake-resistant structures has long been recognized. This need has become more acute with the development of nuclear reactors, greater population concentrations, and the more efficient designs that are made possible by computer technology. During the past two and a half years, SRI International (formerly Stanford Research Institute) has been conducting a program funded by the National Science Foundation to develop an explosive method for testing in-situ structures at strong earthquake levels. The technique will be applicable to buildings, nuclear reactors, pipelines, power lines, dams, bridges, and tunnels.

The technique produces earthquake-like ground motion by simultaneous firing of a planar array of vertical line sources placed in the soil near the test structure. The key feature of each line source is a cylindrical steel canister in which the charge is fired. Controlling the release of the high-pressure explosion products from this canister allows controlled pressurization of the surrounding soil. In this way, both the amplitude and frequency content are controlled at levels suitable for testing with the array close to the test structure. This opens the possibility of in-situ testing at high levels of earth motion with a minimum amount of explosive and with little disturbance to the surroundings. The duration of the simulated earthquake motion can be controlled by delayed multiple firing within each line source and between groups of line sources.

For testing a 30-ft-base structure, the array would probably measure about 80 ft wide and 40 ft deep. It would consist of 10 to 20 line sources placed in vertical bore holes 40 ft deep and spaced on 5- to 10-ft centers, and it would be placed about 20 ft from the structure to be tested. Figure 1 shows one application of the array: testing of

1
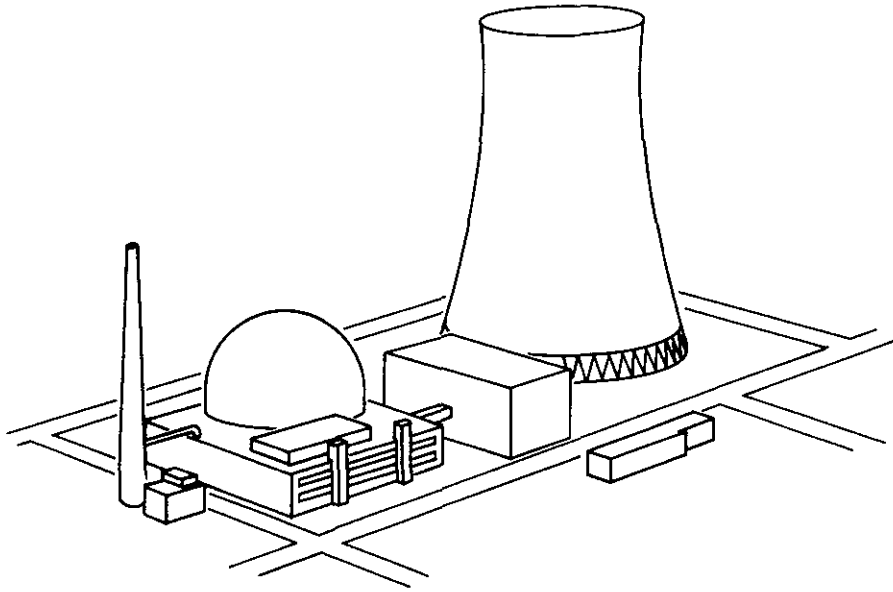
(a) NUCLEAR POWER PLANT
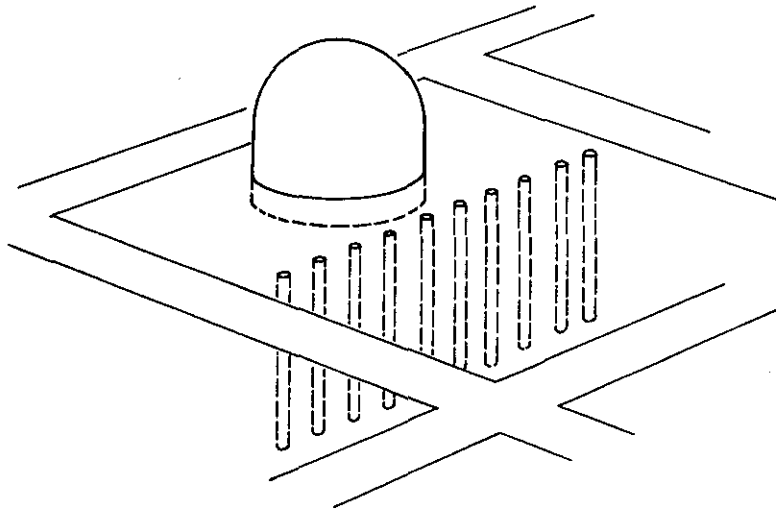
(b) SCALE MODEL TESTING OF CONTAINMENT
    BUILDING

MA-7556-1A

FIGURE 1   APPLICATION OF ARRAY TO NUCLEAR REACTOR TESTING

a scale model of a nuclear reactor containment building. For a 80 x
40 ft array, the reactor containment building would be approximately
1/5 scale. Other structures of less sizable dimensions could be tested
at full-scale with a similar array. Larger arrays can be built as
needed. Results of the current program show that, in general, the
array width should be 2 to 3 times the plan dimension of the test
structure.

In this report we refer to the 80 x 40 ft array as a full-scale
array. It is the smallest and therefore most economical size array
that could probably be used to test full-scale structures, substructures,
and equipment at ground motion amplitudes and frequencies resembling
actual earthquake ground motion. However, it is not the largest array
that could be built; arrays 3 or 4 times the size of the 80 x 40 ft
array are within conventional construction capabilities. Nonethelss,
their cost would have to be weighed against the need. An 80 x 40 ft
array capable of a single detonation costs about $80,000 for construction
and fielding, with the cost per test about $5,000. Material costs
(about 50% of the total cost) increase roughly as the cube of the scale
factor, and labor costs probably increase at about the square of the
scale factor. Thus an 160 x 80 ft array would cost about $500,000.
(All of these costs are exclusive of instrumentation, engineering, and
site development costs, which vary according to the application). When
such arrays are built, they can be considered to be testing laboratories
because they can be used repeatedly, as long as testing at the site is
desired.

In this report we also refer to a 1/3-scale array. As its name
implies this array is approximately one third the scale of the "full-
scale" array. It was built and tested to develop and refine the hard-
ware and to understand the response characteristics of the contained
explosion line source array technique in an economical manner.

3

During the first year of the program (Grant ENV 76-23273, November 1976 to October 1977) we achieved the following:

- Developed reusable hardware for producing contained explosions in a 1/3-scale line source

- Incorporated instrumentation for hardware diagnostics and output measurements

- Demonstrated repeatability of results

- Obtained reasonable accelerations

- Obtained reasonable frequencies.

These results are described in detail in the SRI final report for that year.[1]

B. Current Research Program

The second research program (Grant PFR78-00993, in effect since July 1978) consists of four tasks:

(1) Perform a series of array tests using 10 line sources at 1/3 scale to validate array calculations, and to demonstrate energy coupling and ground motion control in array geometry

(2) Design and test a single full-scale line source to confirm the frequency content, pulse duration, and acceleration levels predicted from the 1/3-scale source measurements

(3) Perform theoretical analyses to predict ground motion amplitude

(4) Conduct further developmental investigations to improve line source performance

This report describes results of the second program.

C. Summary of Results

In Task 1, seven 1/3-scale array tests were performed. In addition to these tests, single-source tests at 1/3-scale were performed to allow direct comparison between a single source and the array. The objectives of these tests series were to (1) compare earth motion from a single source and from an array, (2) observe the effect on earth

4

motion of nonlinear interaction between sources in the array at plastic
soil response levels, (3) test our ability to control pulse shape and
frequency, (4) compare observed earth motion with motion predicted by
simple theory, and (5) test experimental procedures and source integrity
for reuse of the array in several tests.

The results showed that soil velocity and displacement for an array
test are more than an order of magnitude larger than for a single-source
test. The following results were typical of all seven 1/3-scale array
tests.

- The ground motion is uniform along the 12-ft length of
  the instrumented area[*] (along a line parallel to the
  array).

- The ground motion attenuates about 30% across the 10-ft
  width of the instrumented area (along a line perpen-
  dicular to the array).

- The ground motion at the mid-depth of the array has a
  slightly faster rise-time and is slightly lower in amplitude
  than that near the surface.

- The soil displacement and stress follow the source pressure-
  time history in shape.

- The primary frequency of the ground motion is in the 8 to
  15 Hz range. (This scales to 3 to 5 Hz for a full-scale
  array).

At a 10-ft standoff from the 1/3-scale array, in a test with a
total of 6.2 lb of charge, the peak accelerations were 3.5g at the mid-
depth of the array and 2g near the surface; the peak velocities were
7 in./s at mid-depth and 12 in./s near the surface; and the peak dis-
placements were 0.2 in. at mid-depth and 0.4 in. near the surface. At
full-scale (a 80 x 40 ft array), the corresponding near-surface motions
would scale to a peak acceleration of 0.6g, a peak velocity of 12 in./s
and a peak displacement 1.2 in. These are useful levels for structural

---

[*]The instrumented area is an area 10 x 12 ft, centered on the array
centerline at a standoff of 6 ft from the array to the edge of the test
area. This is the area of nearly uniform motion where a test structure
would be located.

5

testing. The charge weight at full-scale would be 120 lb. In short, the 1/3-scale array tests showed that the ground motion was fairly uniform over the test area, that the fundamental period of soil displacement and stress follows the rise and fall of the source pressure, and that ground motion frequencies and amplitudes are at useful levels for structural testing.

In Task 2, only one full-scale line source test was performed because the central charge canister failed on the initial test. We attribute this failure to a rapid explosion rather than a burning of the full-scale propellant charge. The test showed that a full-scale line source can be built, handled, and placed in the ground, and gave us experience in these activities. We believe that no significant changes are necessary in the line source design; the problem can be corrected by simply changing the charge grain size and configuration.

Under Task 3, we developed a quasi-static theory for use in understanding the operation of the single source and the array. For the single source, we employed a static, plane strain, elastic-plastic solution for a pressurized circular hole to predict the displacement and stress field around the source. The measured source pressure was used as the theoretical internal loading. For the array, a static plane strain elastic solution for a pressurized ellipical hole, with its major diameter equal to the array length and its minor diameter equal to the source spacing, was used to predict the displacement and stress field around the array. The internal loading on the ellipse was related to the measured source pressure by using an elastic-plastic finite element computer calculation that accounted for the interaction of the sources and for the finite length of the array.

The theory predicted the response of the soil both for a single source and an array. It accurately predicted the more than order-of-magnitude enhancement in soil displacement for the array as compared to a single source. Both the theory and the array tests show that a critical source pressure for the array exists, below which the soil displacement increases slowly as the source pressure is increased and

6

above which the soil displacement increases rapidly as the source pressure is increased. The theory shows that the critical pressure is that for which the plastic radius around each source in the array approaches its neighbor. At this and higher pressure, the array acts like a slit in the earth rather than a series of individual sources. Therefore, further increases in pressure produce ground motion more efficiently.

Also under Task 3, we applied geometric scaling laws to the 1/3-scale array test results to estimate the ground motion around a full-scale array, for both a single detonation and for three detonations spaced at 1-s intervals for the full-scale array. Response spectra were then calculated for these estimated ground motions, and these spectra were compared to an envelope response spectrum statistically obtained by Newmark, Blume, and Kapur from actual earthquake time histories.[2] The comparison shows good agreement in shape at frequencies higher than 2 Hz. At frequencies lower than 2 Hz, the amplitude of the array spectra is lower than the Newmark, Blume, and Kapur spectrum. The decline for the array is caused by the limited displacements that it can produce (a few inches) compared with the larger displacements in actual earthquakes at frequencies lower than 2 Hz. In structures for which frequencies lower than 2 Hz are important, the structure can be tested at some smaller scale factor, a larger array can be built, or both can be done.

The major outcome of the Task 4 investigations was the development and use of propellants as the charge in the line source. Use of propellant allows smaller charge canisters, together with larger charge amounts, than would be possible with explosive. However, as we learned in the full-scale line source tests, more study of the propellant charge behavior is necessary.

8

II DESCRIPTION OF EXPERIMENTAL APPARATUS

A. Four-Inch-Diameter Line Source

Figure 2 displays the 4-in.-diameter line source used for both single source and array tests. The source is one-third of the full-scale line source that we envision is required for array tests that will shake a 30 x 30 ft test area at full-scale earthquake levels. The most important feature of each line source is a high-strength central steel canister that contains an explosive or propellant charge.[*] The reaction products are vented at a controlled rate into an expandable rubber bladder rugged enough to withstand repeat tests with expansions as large as twice the initial bladder diameter.

The bladder is 4-in. O.D. with a 0.5-in. wall and is fabricated from 40 durometer pure gum rubber. To keep the bladder from leaking, steel bladder supports are fitted to the top and bottom. A thick rubber sleeve prevents the rubber from tearing at these steel supports. The expandable portion of the rubber bladder is 11 ft long.

Vent plugs are fitted into ports in the canister. The plugs redirect the flow from the canister along the axis of the bladder so that the hot explosive gases do not burn the rubber, and also allow the canister vent area to be readily changed.

We have made two significant changes in this line source from the one developed during the first year of work. First, a Mylar diaphragm was added at the top of the source which is ruptured by a small explosive cord (detonated independently from the primary charge) to allow the controlled release of the gas from the bladder. In this way each

---

[*]Two types of charge, Primacord explosive and Blue Dot gun powder, were used. Primacord is a plastic cord containing a central core of pentaerythritol tetranitrate (PETN), produced by the Ensign-Bickford Company. Blue Dot is a granular double-based propellant made from a mixture of nitrocellulose and nitroglycerin. It is produced by the Hercules Company and commonly sold as shotgun powder.

9

Mylar Diaphram

Initiator Lead

2'.5'

Rubber Sleeve

Pressure Gage

Explosive or Propellant Charge

Rubber Bladder
(3 in. I.D. x 4 in. O.D.)

Vent Plug Ports

11.7'

Steel Canister
(1.75 in. I.D. x 2.50 in. O.D.)

15.5

Rubber Sleeve

Scale — inches
0   4   8   12
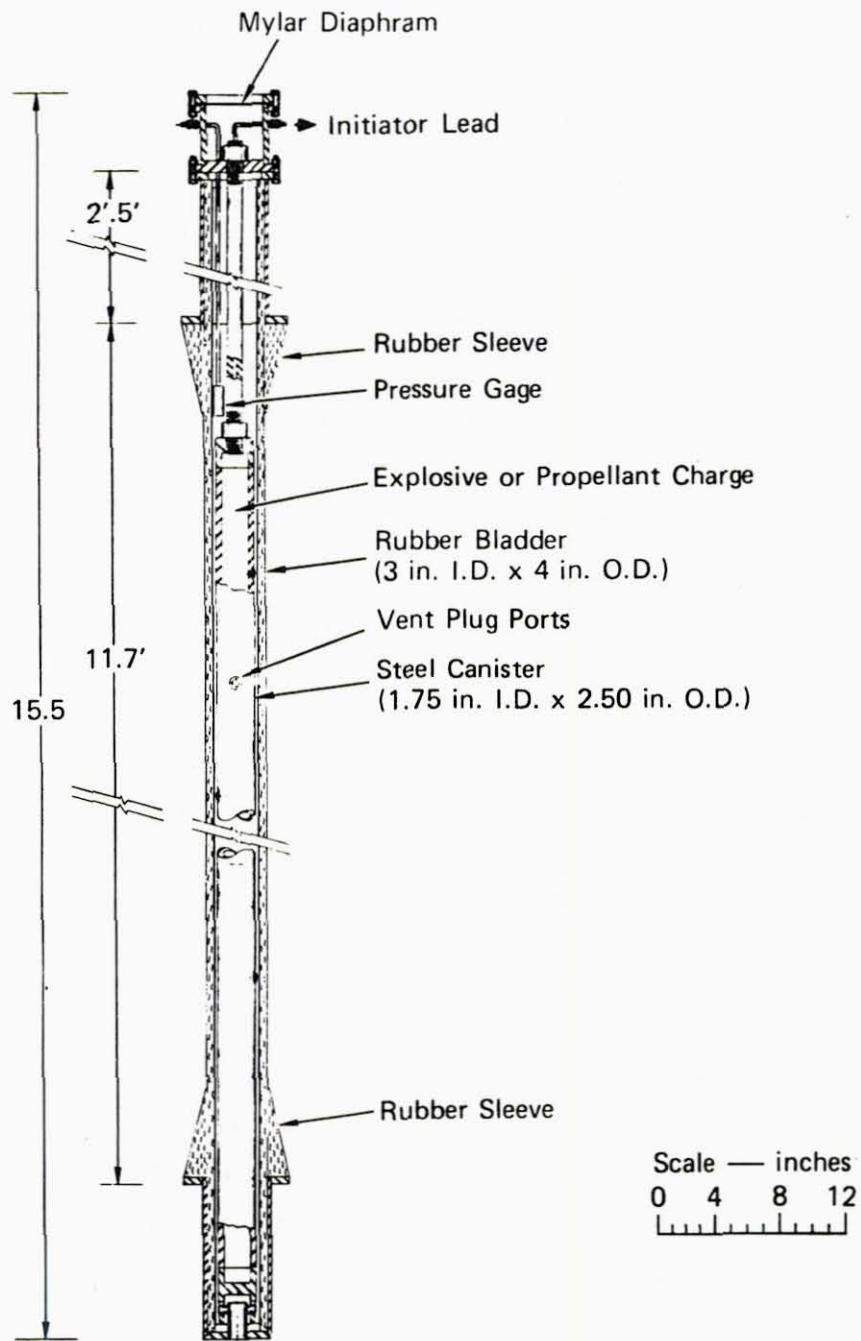
MA-7556-3A

FIGURE 2   ASSEMBLY DRAWING OF THE 4-IN.-DIAMETER LINE SOURCE

10

detonation cycle in the source produces two complete and independently timed oscillations of acceleration. The first results from the initial release of gas from the central canister into the bladder and has acceleration directed away from the source. The second results from the release of gas from the bladder and has acceleration directed toward the source.

The second change allows us to alter the central canister vent area easily without removing the source from the soil. This was accomplished by adding a "turn and lock" connection between the central canister and the bottom cap that allows the canister to be anchored to the top and bottom caps during a test (providing the necessary axial strength to the line source), while still allowing removal of the canister between tests. To keep the rubber bladder straight and to keep it from collapsing due to the surrounding soil overburden when the central canister is removed, we lined the inside of the rubber bladder with a thin-walled, perforated steel tube.

B.   Twelve-Inch-Diameter Line Source

Figure 3 displays the 12-in.-diameter line source. This source is the size we envision is required for an array that will shake a 30 x 30 ft test area at full-scale earthquake levels. The dimensions for this source are roughly scaled by a factor of 3 from the 4-in. diameter line source described above. Again, the key feature of the source is a high strength central steel canister in which the charge is placed. The reaction products are vented at a controlled rate from this canister into an expandable rubber bladder.

The bladder has a 11.75-in. O.D. and a 0.5-in.-thick wall and is made of 40 durometer pure gum rubber. The bladder is fabricated by wrapping the gum rubber onto a thin-wall, perforated steel mandrel and then vulcanizing the rubber to the desired durometer. The perforated mandrel is left inside the bladder, becoming part of the line source. This mandrel serves to keep the unpressurized bladder from collapsing under the soil overburden. As in the 4-in.-diameter source, a steel

11

TOP SECTION   BOTTOM SECTION

Mylar Diaphragm

Detonator Lead

2.0'

Vent Plug
Ports

Perforated
Steel Mandrel

Upper Steel
Cap

6.7'

Steel Canister
(2.75 in. I.D. x
4.25 in. O.D.)

39'

39'

Rubber
Sleeve

Pressure
Gage

Rubber Bladder
(10.75 in. I.D.
x 11.75 in. O.D.)

MA-7556-34
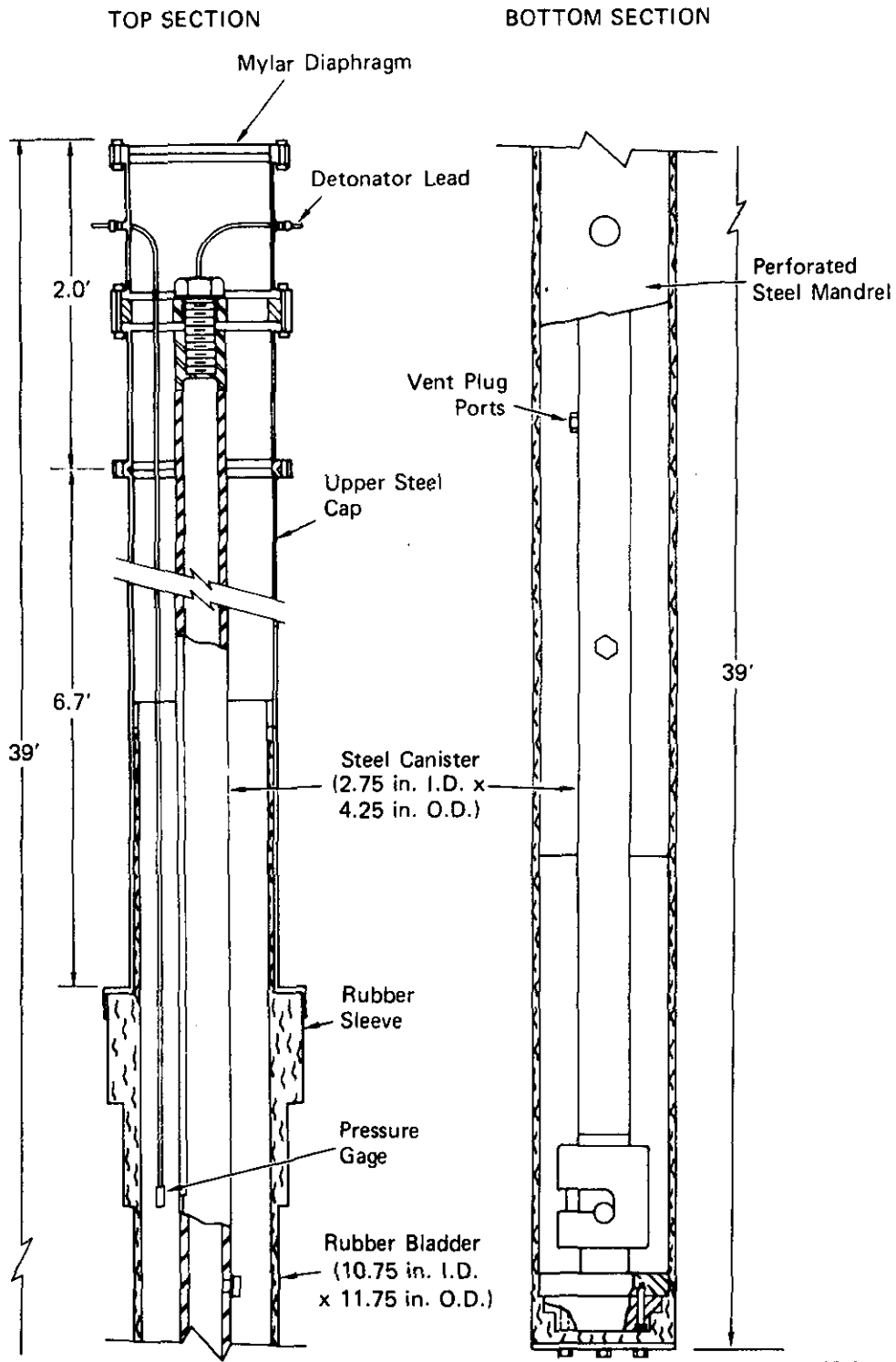
FIGURE 3 ASSEMBLY DRAWING OF THE 12-IN.-DIAMETER SOURCE

12

cap is fitted over the top of the bladder. A thickened section of rubber below this cap prevents the rubber from tearing at the cap. At the base of the bladder a more streamline design is used to allow removal of the line source from the ground. In this design the end of the rubber is built up on the inside, rather than on the outside as it is at the top end (Figure 3). The expandable bladder is 30 ft long.

The steel canister is 4.25-in. O.D. with a 0.75-in. wall. Like the smaller canister in the 1/3-scale source, it is fitted with vent plugs that redirect the flow of hot gases into the axial direction (to avoid burning the bladder) and that allow the canister vent area to be readily charged.

In the full-scale source only Blue Dot propellant was used. The use of propellant allows the relative size of the canister compared to the source to be reduced (see Appendix A). For this reason the 4.25-in. O.D. canister was not directly scaled from the 2.5-in.-dia. canister used in the 1/3-scale source; rather the outer diameter was sized so that as many as three canisters could fit within the source. (We plan to use three canisters in each source during the next year of program to achieve multiple detonations.) The canister wall thickness was chosen, as it had been in the 1/3-scale line source canister, to maximize the charge that could be contained within a given outer diameter.

Other features of the 12-in.-diameter line source are similar to those of the 4-in.-diameter source. The Mylar diaphragm at the top is explosively ruptured to allow the release of gas. The central steel canister can be removed by using a turn and lock connection at the base. A pressure gage on the end of a steel tube measures pressure 8 ft below the top of the source. (Pressure is measured below the top because after the top diaphragm ruptures, bladder pressure cannot be measured accurately by a gage located at the exit.)

C.   Test Site

At the start of the current program a survey was taken to evaluate
potential sites.[*]   A site at Camp Parks, a U.S. Army reserve base near
Dublin, California, was chosen for the program.

A level area within a few hundred feet of power and water was
selected for exploration.   Previous drilling in nearby areas had
indicated the upper 100 to 200 ft of soil to be a fairly uniform deposit
of clay.   Five 20-ft-deep sampling holes were drilled for our exploration.
We obtained soil samples at depths of 3, 10, and 18 ft by driving 3-in.-
diameter, 36-in.-long, thin-walled tubes (Shelby Tubes) into the
undisturbed soil.

These samples indicated that the upper 20 ft of soil is a fairly
uniform deposit of dark grey, stiff clay containing some caliche.   The
soil samples taken between the 10-ft and 12-ft depth also show a few
randomly oriented lenses of sand, 1 to 6 in. thick.   The water table
was at 11 ft.

To characterize the soil, we performed the following tests on soil
samples: six unconfined compression tests, a set of consolidated,
undrained triaxial tests, and three consolidation tests.   The unconfined
compressive strength averaged 50 psi at a depth of 3 ft, 25 psi at a
depth of 10 ft, and 35 psi at a depth of 18 ft.   The water content varied
from 60% near the surface to 90% near the water table.   The triaxial
data showed a friction angle of 30° and a cohesion of 5 to 10 psi.
These tests are described in more detail in Appendix B.

This area was deemed suitable as the test site.   The area was
fenced in, an instrumentation trailer was hauled to the site, and
power and water lines were installed.

---

[*] SRI maintains a 400-acre remote explosive test site with several
instrumentation bunkers near Tracy, California.   The first earthquake
simulation program was begun there; however, because the terrain is
hilly and the soil is rocky, we concluded it would not be a suitable
test site for the program.

D.   Instrumentation

We employed four types of instrumentation--pressure gages, a bladder expansion gage, accelerometers, and soil stress gages (see Figure 5 in the next section). The pressure gages measure pressure inside the bladder. The bladder expansion gage, developed during the first year, measures the bladder expansion as a function of time for the 4-in.-diameter source. The bladder expansion gage was not used in the 12-in.-diameter source tests. Accelerometers and soil stress gages were placed in the free field to measure ground motion and stress

The bladder expansion gage consists of a 2 x 6 x 0.016 in. steel sheet wrapped around the bladder and held in place with a thin rubber sleeve. A strain gage determines the curvature change of the steel sheet and thus the diameter of the rubber bladder. This bladder expansion gage was calibrated in the laboratory and field-checked by comparison with a passive bladder expansion gage consisting of a wire with two slip connections fitted around the bladder. Terminal observation of the wire length gave the maximum bladder expansion during the test for comparison with the active gage.

The soil stress gage is a design of the U.S. Army Waterways Experimental Station, Vicksburg, Mississippi, and is currently manufactured by Kulite Semiconductor. The design is based on the principle of a deflecting, rigidly clamped, circular diaphragm. The gage is wafer-shaped with a sensing diaphragm on both sides. Semiconductor strain gages, bonded to the diaphragms, are the sensing elements. The overall gage assembly is 2 in. in diameter and 0.22 in. thick.

Figure 4 shows the measurement designation system used for both the single-source and array tests. Designation (1) refers to the type of measurement; designation (2) refers to the sensing direction; designation (3) refers either to the distance from a single source or the distance measured perpendicular to the array; designation (4) refers either to an aximuth in degrees for a single source or the distance off the array centerline; and designation (5) refers to depth. All distances are in feet.

15

```
(1)   (2)   (3)      (4)     (5)
 A     H    6.0      0.0     7.5
 ▲     ▲     ▲        ▲       ▲
 │     │     │        │       └── DEPTH FROM SURFACE (Feet), Z
 │     │     │        │          DISTANCE OFF ARRAY CENTERLINE, X
 │     │     │        │             (Azimuth in Degrees for Single Source)
 │     │     │        └────────  DISTANCE FROM ARRAY, Y
 │     │     │                     (Source Number for Measurement in Source)
 │     │     └─────────────────  SENSING DIRECTION
 │     │                            H =  Horizontal
 │     │                            V =  Vertical
 │     └───────────────────────  TYPE OF MEASUREMENT
 └─────────────────────────────    P = Bladder Pressure
                                    EX = Bladder Expansion
                                    A = Acceleration
                                    SS = Soil Stress
```
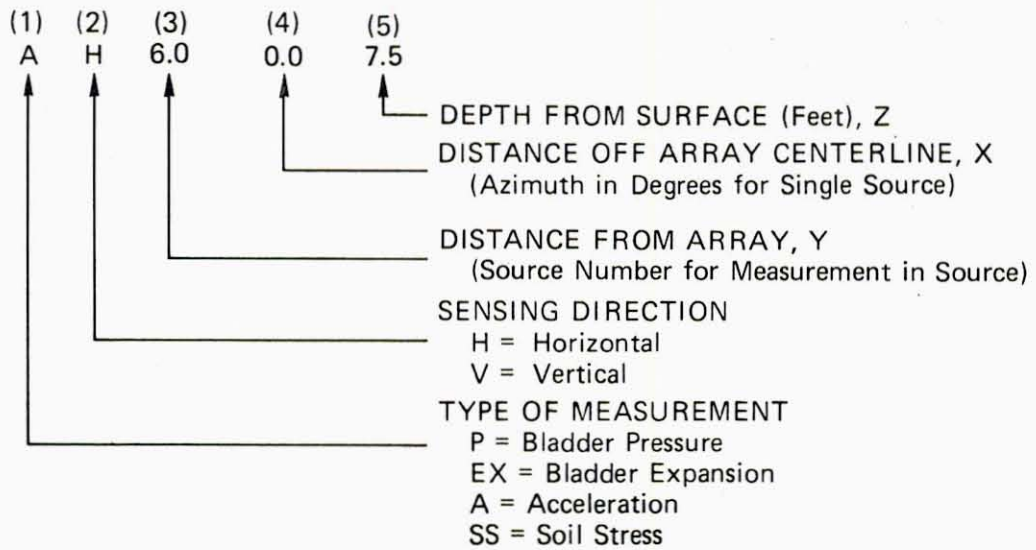
MA–7556–6A

FIGURE 4   MEASUREMENT DESIGNATION SYSTEM

16

III SINGLE-SOURCE TEST RESULTS

A. Four-Inch-Diameter Line Source

We undertook these tests to check the hardware and placement
techniques for the 4-in.-diameter line source and to obtain data on
single-source performance for later comparison to the array performance.

Figure 5 is a schematic of the line source in soil. The source
was first placed in a 9-in.-diameter, 15-ft-deep, drilled hole. Figure
6 shows the line source being lowered into the hole. Once the source
was in place, the hole was backfilled with a mix containing 73% (by
weight) No. 30 sand, 15% clay, 12% water, and 0.3% CFR2 (a fluidizing
agent). For backfilling, we placed a hose alongside the source and
pumped the mix into the bottom of hole. The backfill is both relatively
incompressible (thus providing good coupling between the source and the
surrounding soil) and pumpable (thus greatly simplifying the placement
technique by minimizing voids).

Once the sand/clay mix was pumped to the level of the upper rubber
sleeve, the hose was removed and the upper 2.5 ft of the hole was
back-filled with saturated sand and tamped. This upper 2.5 ft served
as a cap for the semifluid sand/clay backfill.

Between tests, the upper 2.5 ft of sand was removed, the sand/clay
mix was vibrated, and more mix was added if necessary to raise the level
even with the upper rubber sleeve. (The amount of mix added varied
from a quart to several gallons.) The upper 2.5 ft of sand was then
replaced and retamped.

In addition to the pressure gages and expansion gages on the source,
two accelerometers and a soil stress gage were placed in the surrounding
soil. One accelerometer was located at the center-depth of the source
(7.5-ft depth), and one was located 2 ft below the surface (see
Figure 5). Both accelerometers were oriented with the sensing axis

17
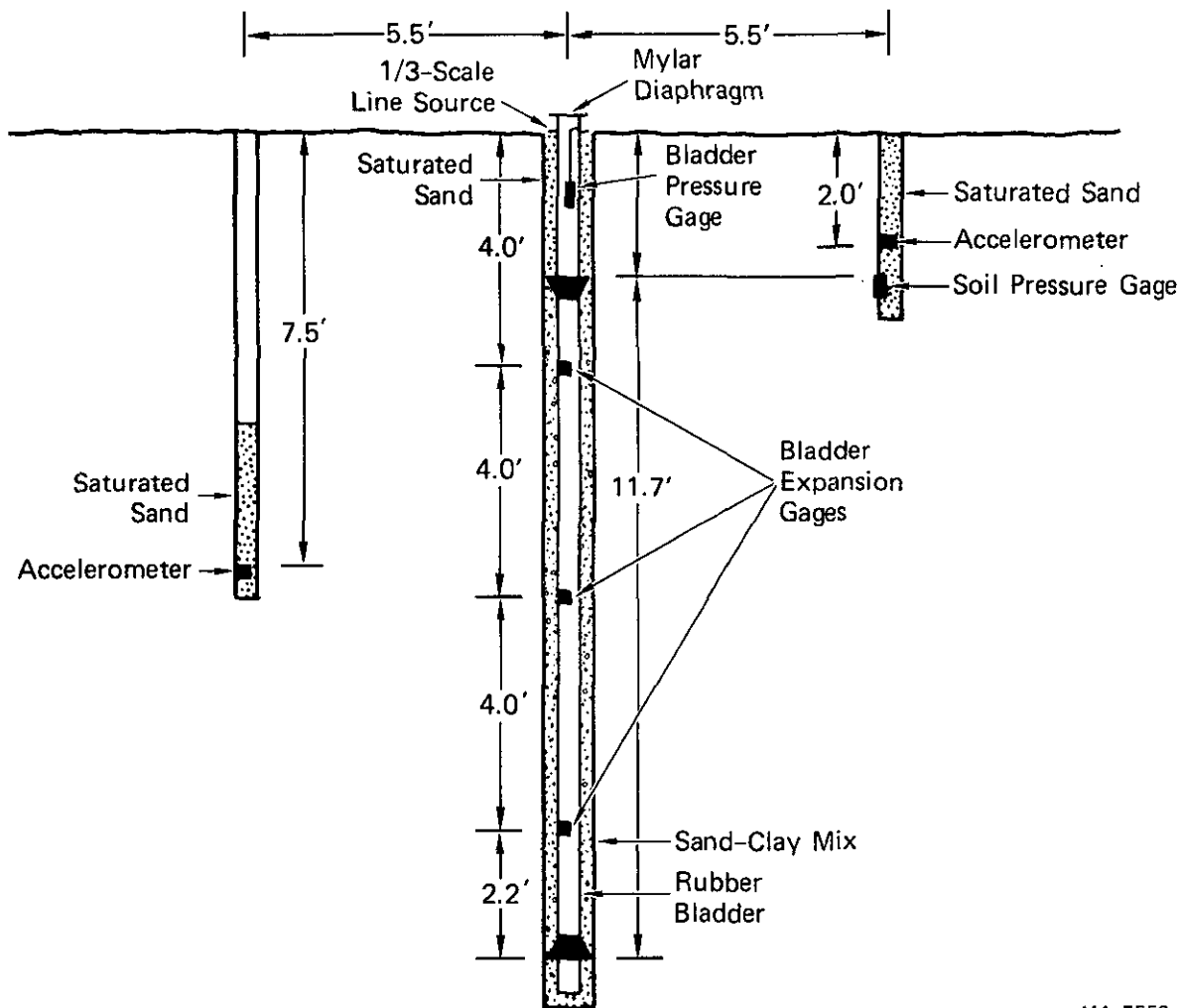
FIGURE 5   SCHEMATIC OF 4-IN.-DIAMETER LINE SOURCE IN SOIL

MA-7556-4

18

MP-7556-5

FIGURE 6   PLACEMENT OF 4-INCH-DIAMETER LINE SOURCE IN SOIL

19

horizontal and with the postive direction radially away from the source. The accelerometers were placed in 6-in.-diameter holes that were back-filled with 2 to 3 ft of saturated sand to ensure good coupling to the soil. The soil stress gage was placed 2.5 ft deep in the same borehole as the 2-ft-deep accelerometer. One face of the soil stress gage was pressed into the in-situ soil and then saturated sand was backfilled behind the gage.

For these tests, all free-field measurements were made at a radius of 5.5 ft. We chose this distance because it is near a lower bound on the standoff distance for a test structure from an array and because ground motion amplitude decays quickly with distance from a single source, making it desirable to make measurements close to the source.

Figure 7 shows the bladder pressure, soil stress, and bladder expansion from a typical test (Test 125) using 0.25 lb of PETN and a canister vent area of 0.60 in.^{2}. In this test the Mylar exhaust diaphragm was ruptured 40 ms after the primary detonation. The bladder pressure rises almost linearly to near its peak in the first 15 ms and falls suddenly on rupture of the Mylar diaphragm at t = 40 ms [Figure 6(a)]. This sudden fall in pressure does not represent the true bladder pressure because the gage was located in the neck of the bladder 12 in. from the exhaust, and some choking of the flow occurs in this neck. (In later tests this effect was minimized by locating the gage at the base of the neck, 30 in. from the exhaust.)

Comparing Figure 7(b) with 7(a) shows that soil stress follows the bladder pressure in shape but has a slower rise, with some ground oscillation superimposed. The rise time of the soil stress is delayed by about 10 ms from the rise time of the bladder pressure because of propagation time through the soil to the gage.

Figure 7(c) shows the bladder expansion record. Importance cannot be placed on the details or the amplitude of the bladder gage response because of the many sources for nonuniform expansion around the circumference and along the length of the source. However, the general shape of the bladder expansion record shows that the bladder displacement
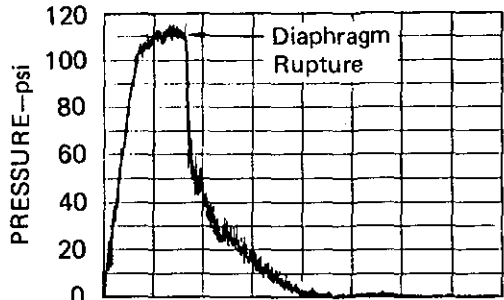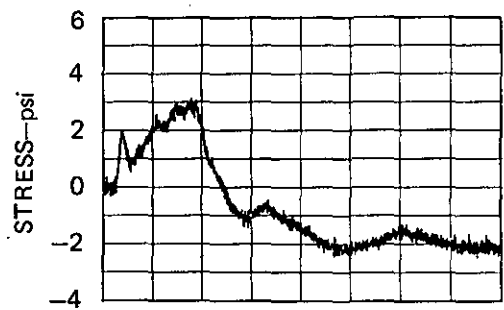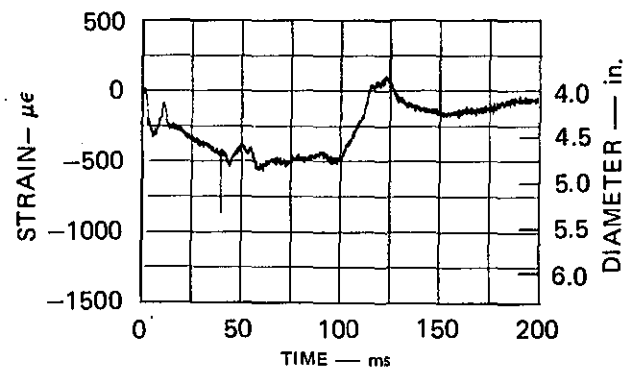
FIGURE 7   BLADDER PRESSURE, SOIL STRESS, AND BLADDER
EXPANSION FROM THE 4-IN.-DIAMETER SINGLE-
SOURCE TEST

Test 125, 0.25 lb PETN, Canister Vent Area, 0.60 in.^{2}

21

closely follows the shape of the soil stress during the pressure rise. The return of the bladder to its initial diameter is delayed in time from the pressure decay because the bladder tends to collapse only after its pressure has dropped below 15 psi.

Figure 8 shows the earth motion 5.5 ft from a single source for the test discussed above. Figures 8(a) and 8(b) show accelerations at the 7.5-ft and 2.0-ft depths. We attribute the initial high acceleration of 3g at the 7.5-ft depth [Figure 8(a)] to the source pressure having an initial sharp rise; it is therefore not well-matched to that required for sinusoidal acceleration at the fundamental earth motion frequency. This effect could be reduced if necessary by refining of the controlled venting process to lessen the initial sharp pressure rise. The accelerations near the surface [Figure 8(b)] are lower in amplitude and frequency. We attributed this to the stress relief near the surface and to the active length of the source not beginning until a depth of 3 ft. Water content variation with depth may also influence the difference between responses at depth and surface.

Figures 8(c) through 8(f) show the velocity and displacement time histories for the two accelerometer locations; these histories were calculated by integrating the acceleration records.* The velocity and displacement at the 7.5-ft depth are very small [Figures 8(c) and 8(e)]. This is consistent with the theory of single-source operation discussed in the next section. The velocity and displacement near the surface are larger than those at depth, which can be attributed to the relief from the free surface [Figures 8(d) and 8(f)]. The acceleration, velocity, and displacement near the surface are also consistent with the results of the first year's program, which was performed at a different test site and where acceleration was primarily measured at the 2-ft depth.

---

*A first-degree polynominal was used to correct the acceleration baseline before integration. The two coefficients were chosen by a standard method, consisting of minimizing the square of the velocity over the duration of the record. This technique is discussed in detail in Appendix C.

7.5 FT. DEPTH   2.0 FT. DEPTH

(a) ACCELERATION, a (AH5.5, 0°, 7.5)

(b) ACCELERATION, a (AH5.5, 180°, 2)

(c) VELOCITY, v = ∫ adt

(d) VELOCITY, v = ∫ adt

(e) DISPLACEMENT, d = ∫ vdt

(f) DISPLACEMENT, d = ∫ vdt
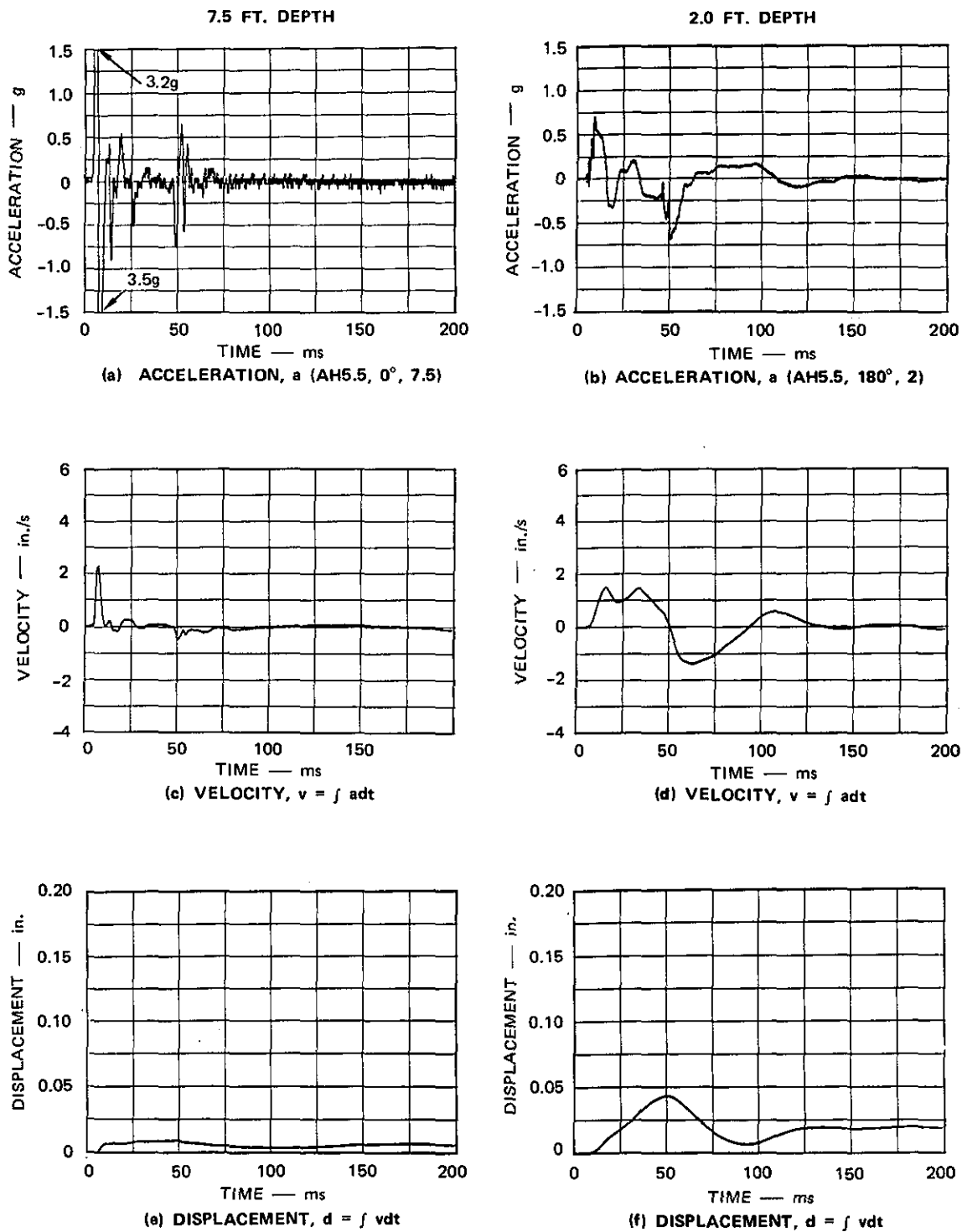
MA-7556-8

FIGURE 8   EARTH MOTION 5.5 FT FROM THE 4-IN.-DIAMETER SINGLE SOURCE

Test 125, 0.25 lb PETN, Canister Vent Area 0.60 in.^{2}

23

B.   Twelve-Inch-Diameter Line Source

The objectives of these tests were to check the hardware and place-
ment techniques for the 12-in.-diameter source, to obtain data on
scaling between the soil motion for a 4-in.-diameter source and that
for a 12-in.-diameter source and to obtain data for later comparison to
the 80 x 40 ft array tests. (Tests of an 80 x 40 ft array comprised
of eight to ten 12-in.-diameter line sources are planned for next years'
program.) In this test series, only the objective of checking the hard-
ware and placement techniques were met due to a failure of the central
charge canister on the initial test. This failure is discussed in more
detail below.

Figure 9 is a schematic of the line source in the soil. The first
step in placement was the drilling of a hole 24-in. in diameter by 37 ft-
deep. As expected, the high water table at Camp Parks caused the hole
to fill with water to the 12-ft depth within about a half hour. We had
been prepared to line the hole with steel pipe to prevent the soil from
slumping off the sides but found that only minimal slumping occurred.
We therefore proceeded without a liner. In other locations at the site
the steel liner may still be necessary. If a liner is used, it must
be pulled after the line source is placed.

The line source was placed in the hole in three sections, because
we had no convenient method for assembling the line source in the
horizontal position. The first section placed was the 32-ft-long
rubber bladder and mandrel (Figure 3). Figure 10 shows it being lowered
into place by the boom on the drill rig. Because this section is slightly
buoyant and sealed at the bottom, it floated in the drill hole about
4 ft off the bottom. The next section was the 6.7-ft-long upper steel
cap. Once this cap was in place, the source was no longer bouyant and
sank to the bottom of the hole. This cap fits over the upper 2 ft of
rubber, and thus serves as a seal; the cap extends from the ground
surface down to the rubber bladder and provides 6.7 ft of soil confine-
ment above the bladder. The last section to be placed was the 37-ft-
long central charge canister. When it was in place, we locked it to

24
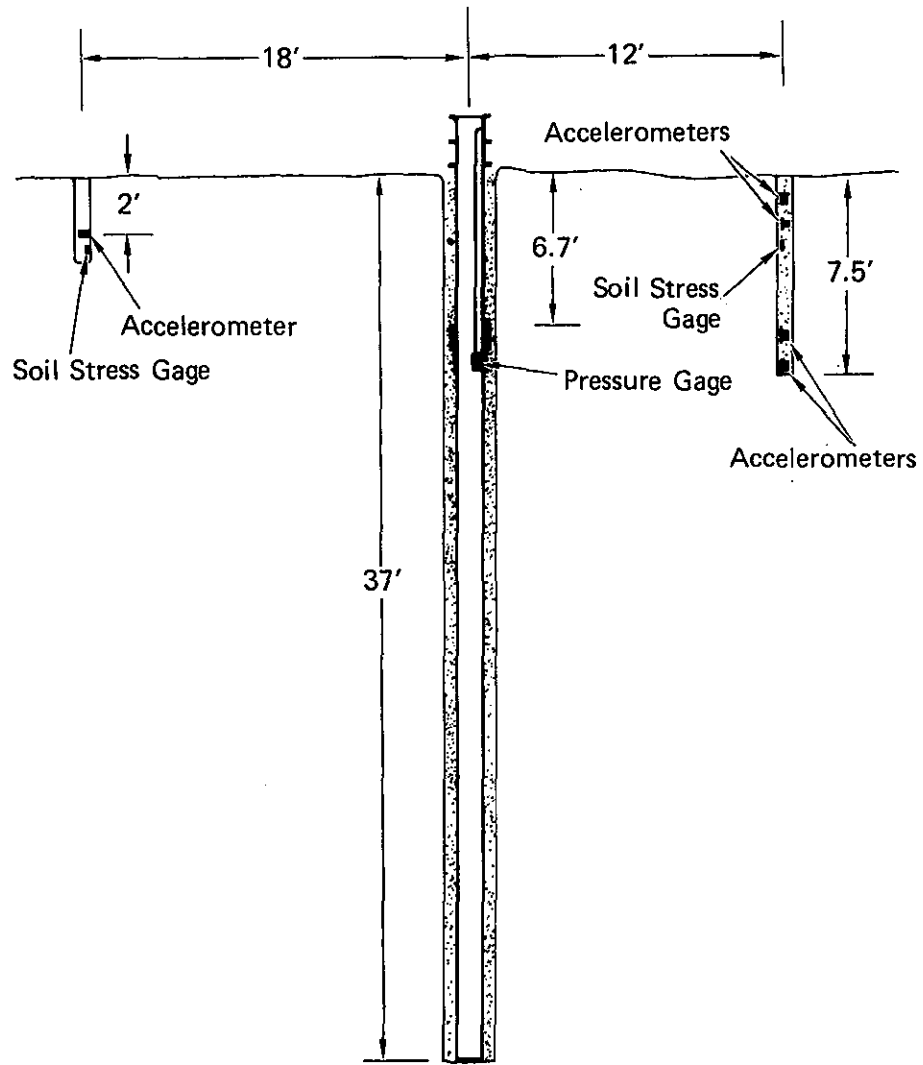
MA-7556-35

FIGURE 9   SCHEMATIC OF THE 12-IN.-DIAMETER LINE SOURCE IN SOIL
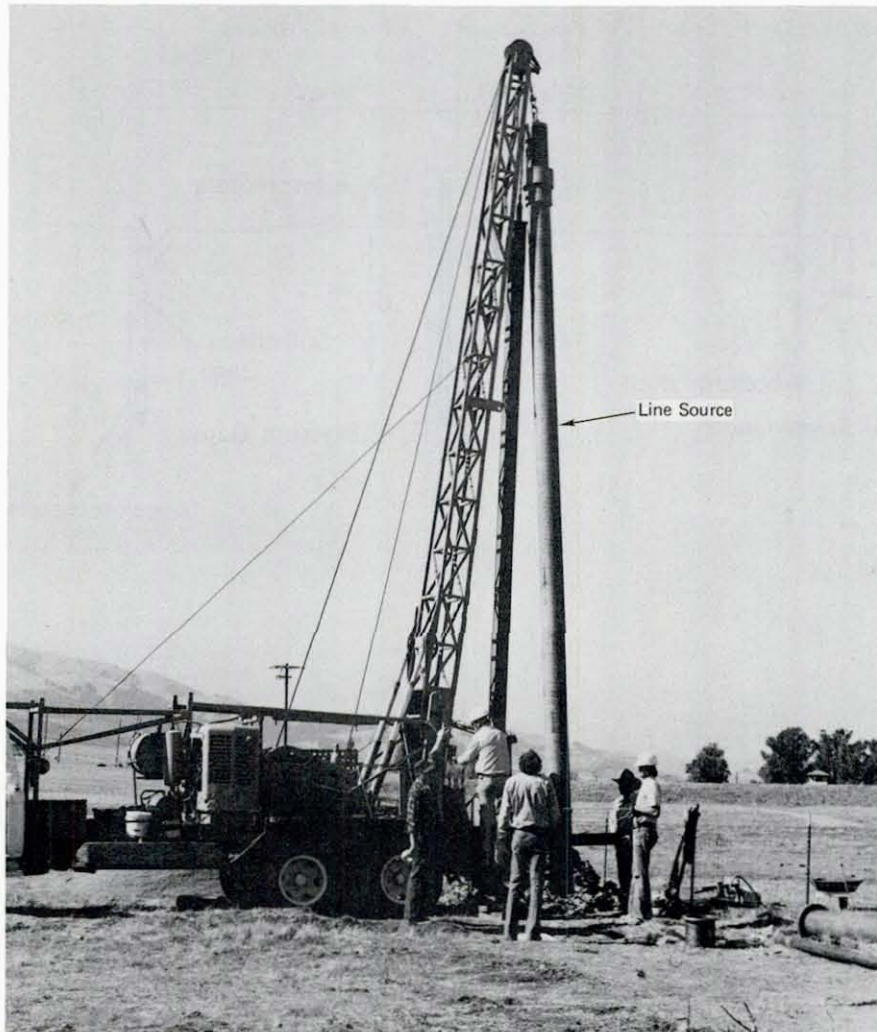
Line Source

MP-7556-36

FIGURE 10   PLACEMENT OF THE 12-IN.-DIAMETER LINE SOURCE IN SOIL

the bottom of the line source by a turn-and-lock connection and then bolted it to the top of the source, thus, holding the line source together axially.

Once the source was assembled in place, sand was backfilled into the hole. As the sand was being added, excess water was pumped from the hole to keep the water level at the 12-ft depth. Above the 12-ft depth the sand was simply added and tamped into place.

As shown in Figure 9, pressure gages were placed in the source to measure the bladder pressure at a depth 8 ft below the top of the source. Three horizontal accelerometers were placed at a standoff of 12 ft and at depths of 2, 6 and 7 ft, and one was placed at an 18-ft standoff and a 2-ft depth. A single vertical accelerometer was placed at a 12-ft standoff and a 1-ft depth. Two soil stress gages were placed side by side at a 12-ft standoff and 2.5-ft depth.

The initial test (Test 160) was performed using 4 lb of Blue Dot propellant. The propellant charge configuration was based on the previous 1/3-scale array tests with propellant described in Section V, and on the closed chamber tests of a 1/3-scale charge canister described in Appendix A. The configuration consisted of four 2-in.-diameter by 14-in.-long paper tubes, each filled with 1 lb of Blue Dot. These tubes were spaced uniformly on a 35-ft-long strand of 50 gr/ft* Primacord that ran through the center of each tube. This Primacord, which contained a total of 0.25 lb of PETN, was used to initiate the charge tubes. This configuration was then placed within the 4.25-in.-O.D. charge canister. The canister had been fitted with 16 vent plugs whose total area was 1.8 in.^{2}. This value was scaled from the 4-in.-diameter line source vent area.

Posttest observation of the source indicated that the charge canister had fragmented near the uppermost charge tube, 6 ft from the top of the source. The section of the canister above this tube appeared to be undamaged. The canister below this tube was not recovered because sand

---

*
1 grain (gr) equals 1/7000 lb.

and water quickly filled the source to the 12-ft depth, indicating that a large opening in the bladder and mandrel had occurred below the water table. When we probed the sand with a stiff rod, we found the top of the next section of charge canister at a depth of 19 ft.

We conclude that the charge canister fragmented at the four charge tubes locations, cutting the canister into five pieces. The lower four fell, to a position of three stacked on top of each other with one along side, leaving the 19-ft-depth to the top of the first section. At the location of each charge tube the fragmenting canister tore open the rubber badder and mandrel allowing the sand water to enter.

The instrumentation records support this conclusion. The pressure gages in the bladder were at the depth of the first charge tube and were damaged by fragments. Their records show a high amplitude ringing occurred at the time of detonation, indicating the fragmentation of the charge canister took place within the first millisecond. The accelerometer records show a very high amplitude and high frequency earth response, indicating the controlled venting process was not working. Because of the much higher than expected acceleration amplitude, the accelerometer outputs overshot the tape recorder settings and thus no quantative maximum accelerations were measured.

The charge for this initial test was chosen with the assumption that it was a fairly safe charge amount for the canister. In the closed chamber tests described in Appendix A, we tested a canister of approximately 1/3-scale from the canister used here. No damage was seen at a charge density of 11 lb/ft^3. With 4 lb in the 4.25-in.-O.D. canister, which has a interior volume of 1.5 ft^3, the charge density was only 2.7 lb/ft^3, a seemingly safe value. (Both canisters have similar radius to thickness ratio, thus, have similar strength.) Additionally, for the closed chamber tests the charge canister had an I.D. of 0.81 in. and the charge tube had a diameter of 0.75 in.; thus, the charge occupied 86% of the interior cross-sectional area. In this test the charge canister had an I.D. of 2.75 in. and the charge tube had a diameter of 2.00 in.; thus, the charge occupied only 53% of the interior cross-sectional area, again a seemingly safe value.

Further study indicated a possible cause for the canister failure. The burn rate of a propellant increases rapidly as a function of pressure (see Appendix A). The larger the charge, the slower the pressure dissipates; thus, the burn rate and the pressure at the burn front increases. This local increase in pressure probably led to a detonation of the propellant, that fragmented the canister at the charge tube locations.

Several ways exist for correcting this problem in furture tests. For one, slower burning propellants can be used. These propellants have a slower burn rate, primarily because of their larger grain size. In effect, this is one reason why scaling did not predict the pressure accurately in the full-scale test: The grain size of the propellant was not scaled in going from 1/3-scale to full scale.

Another approach is to space the charge more evenly along the charge tube. Originally, the charge was concentrated to give it more confinement and therefore a short burn time relative to the time of venting for the canister. However, from the results of the full-scale line source test we have learned that the burn time is much faster than this lower time limit; therefore a spread out charge is desirable.

We believe that the best approach is to try the methods discussed above with a well-instrumented section of the full-scale charge canister outside of the line source. In this way we will understand the burn rate of the propellant more thoroughly and will determine the true limits of the canister. Once a desirable charge type and configuration have been determined, they can then be used in the line source.

In summary, the full-scale line source test showed that a 12-in.-diameter by 37-ft-long line source can be built, handle.1, and placed in the ground. The tests gave us experience in these activities. We believe that no significant changes necessary are in the line source design itself. The major changes necessary are in charge grain size and configuration. A number of methods are available to correct the problem of excessive charge pressure and they can be conveniently investigated in simple laboratory tests.

30

IV QUASI-STATIC THEORY FOR SINGLE-SOURCE
AND ARRAY RESPONSE

We employed a quasi-static theory to understand the operation of
the single source and to extrapolate the single-source results to the
array geometry. We present this theory before describing the experimental
results for the array because it indicates the response mechanisms
taking place in the array tests and clearly shows the reason for testing
with an array.

The basis of the quasi-static theory is shown in Figure 11. The
wave front moves about 15 ft (75 source radii) during the pressure rise,
indicating that a static theory can be used for displacement near the
source. During the complete pulse, the wave front has moved above 100
ft; therefore, a static theory can be used for overall estimates of
displacement from a single source at ranges of interest for structural
testing (5 to 15 ft for this source). For the array, these wave front
propagation distances are comparable to the 30 x 15 ft array dimensions
(a 1/3-scale array), but a static theory is still useful for interpreting
some features of response and to show the relationship between array
and single-source response. A static theory can also be justified by
the experimental observation (see Section V) that displacement follows
the source pressure, the basic characteristic of quasi-static response.

A. Single Source

To estimate the elastic response around a single source, we consider
the static plane strain problem of a pressurized circular hole with
radius a_s. The displacement u at a distance r for this idealization
would be

$$u = \frac{P_s (1 + \nu)}{E} \frac{a_s^2}{r} \tag{1}$$

31
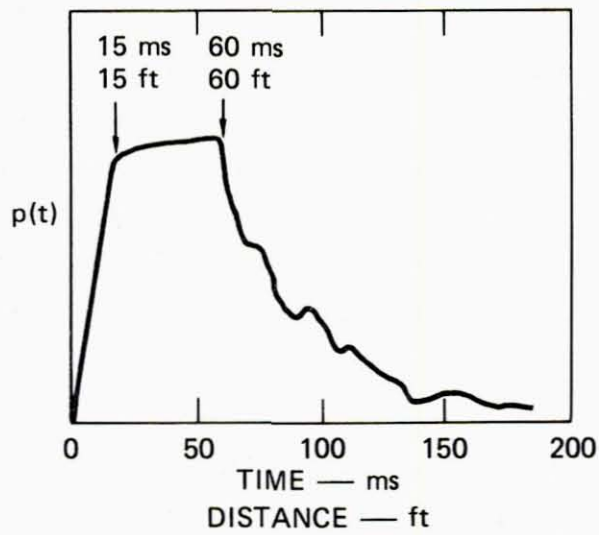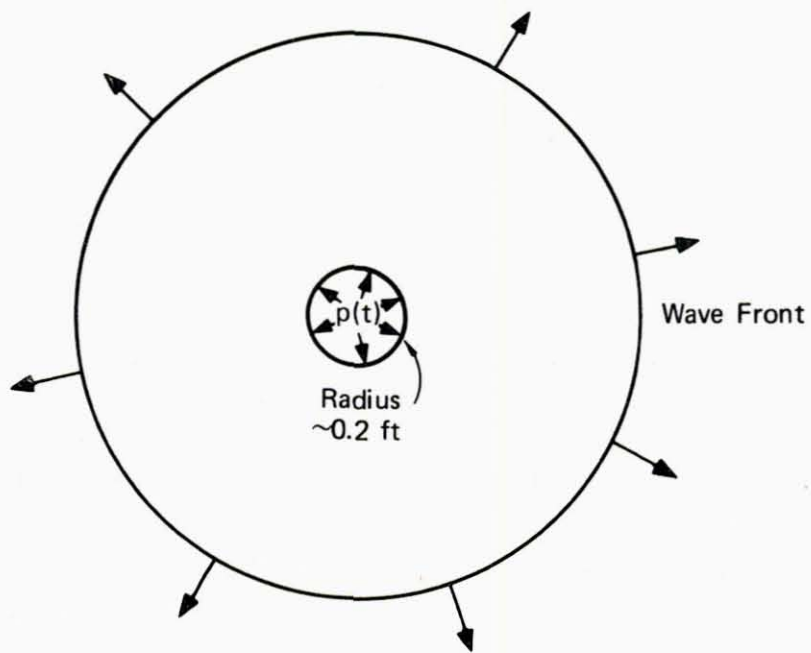
FIGURE 11   COMPARISON OF SOURCE DIMENSIONS
WITH WAVE FRONT LOCATION

in which E is Young's modulus, ν is Poisson's ratio, and P_s is the source pressure. The source pressure is defined as the pressure of the bladder on the surrounding soil and is approximately 20 psi less than the bladder pressure at expansions greater than 25%. (The 20-psi pressure is carried by the hoop stress in the rubber.)

For values of E, ν, and P_s consistent with the single-source test described in Section III (E = 5000 psi, ν = 0.25, P_s = 75 psi),

$$u = \frac{75(1 + 0.25)}{5000} \frac{a_s^2}{r} = 0.019 \frac{a_s^2}{r} \tag{2}$$

At a radius of 5.5 ft with a_s = 0.2 ft, we have u = 0.0016 in. Thus displacements for an entirely elastic response would be extremely small because the source dimension a_s is quite small as compared with the standoff r.

However, near the source the soil yields[*] when the source pressure increases above an initial yield pressure P_y. As P_s is increased further, a plastic zone of increasing radius R is formed as indicated in Figure 12. Appendix D gives a complete description of elastic-plastic analysis of a pressurized cylindrical cavity. The soil is treated as a Mohr-Coulomb material with unconfined strength σ_u and friction angle ϕ. The initial yield pressure is given by

$$P_y = \frac{\sigma_u}{N_\phi + 1} \quad , \quad \text{where } N_\phi = \frac{1 + \sin\phi}{1 - \sin\phi} \tag{3}$$

As the source pressure increases, the radial stress σ_r at the boundary r = R remains at this yield value P_y, but R increases. Because the elastic solution for $r \geq R$ has the same form as already given, the displacements are now given by

---

[*] The soil also compacts immediately around the source, but this mainly affects the deformation at the source hole and hence the gas energy required to maintain the pressure P. In the present analysis, P is taken as a known quantity from the experiments. A theory that accounts more completely for soil constitutive relations is planned for future work.

Plastic

Elastic

a_s

R

P_s

$$\sigma_r = \frac{\sigma_u}{N_\phi + 1}$$
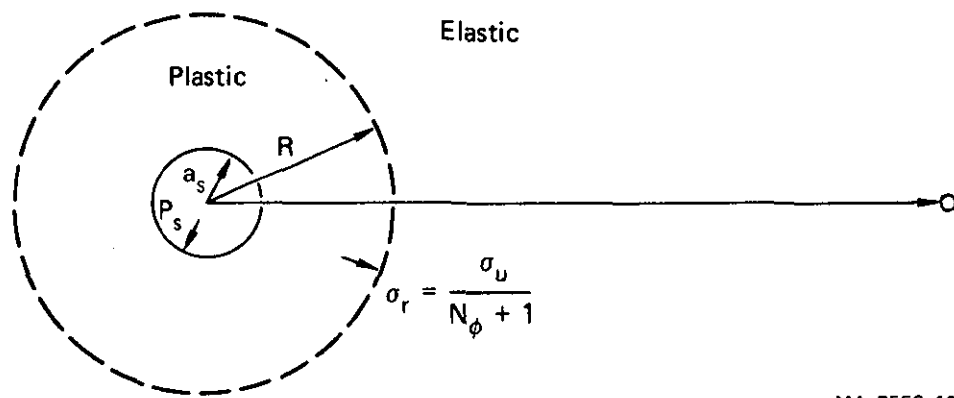
MA-7556-10

FIGURE 12   SINGLE-SOURCE ELASTIC-PLASTIC MODEL

$$u = \frac{P_y(1 + \nu)}{E} \cdot \frac{R^2}{r} \qquad P_s \geq P_y \qquad (4)$$

in which

$$\frac{R}{a_s} = \left\{ \frac{N_\phi + 1}{2N_\phi} \left[1 + (N_\phi - 1) \frac{P_s}{\sigma_u} \right] \right\}^{\frac{N_\phi}{N_\phi - 1}} \qquad (5)$$

For typical soils and, in particular, from measurements made on the soil at the Camp Parks test site, $\phi = 30°$ and the plastic radius and yield pressure are given by

$$\frac{R}{a_s} = \left(\frac{1 + 2P_s/\sigma_u}{1.5} \right)^{1.5} \qquad P_y = \frac{\sigma_u}{4} \qquad (6)$$

It is also useful to express the postyield displacement in Eq. (4) as a multiple of the displacement u_y at initial yield $P_s = P_y$, which is given by Eq. (4) with $R = a_s$. Then Eq. (4) becomes simply

$$\frac{u}{u_y} = \left(\frac{R}{a_s} \right)^2 \qquad (7)$$

in which

$$u_y = \frac{\sigma_u(1 + \nu)}{(N_\phi + 1)E} \frac{a_s^2}{r} \qquad (8)$$

These results are displayed graphically in Figure 13 for $\phi = 30°$. As P_s/σ_u increases from 0.25 at initial yield to $P_s/\sigma_u = 2.5$, the yield radius grows from $R/a_s = 1$ to $R/a_s = 8.0$. The displacement increases from $u/u_y = 1$ to $u/u_y = 64$. If the soil were to remain elastic over this pressure increase, the displacement would increase linearly to $u/u_y = 10$, as shown by the straight line drawn through the initial yield point. The plastic deformation therefore increases the displacement 6.4 times that in an entirely elastic deformation. This factor increases sharply as P_s increases still further. At $P_s/\sigma_u = 4$, the
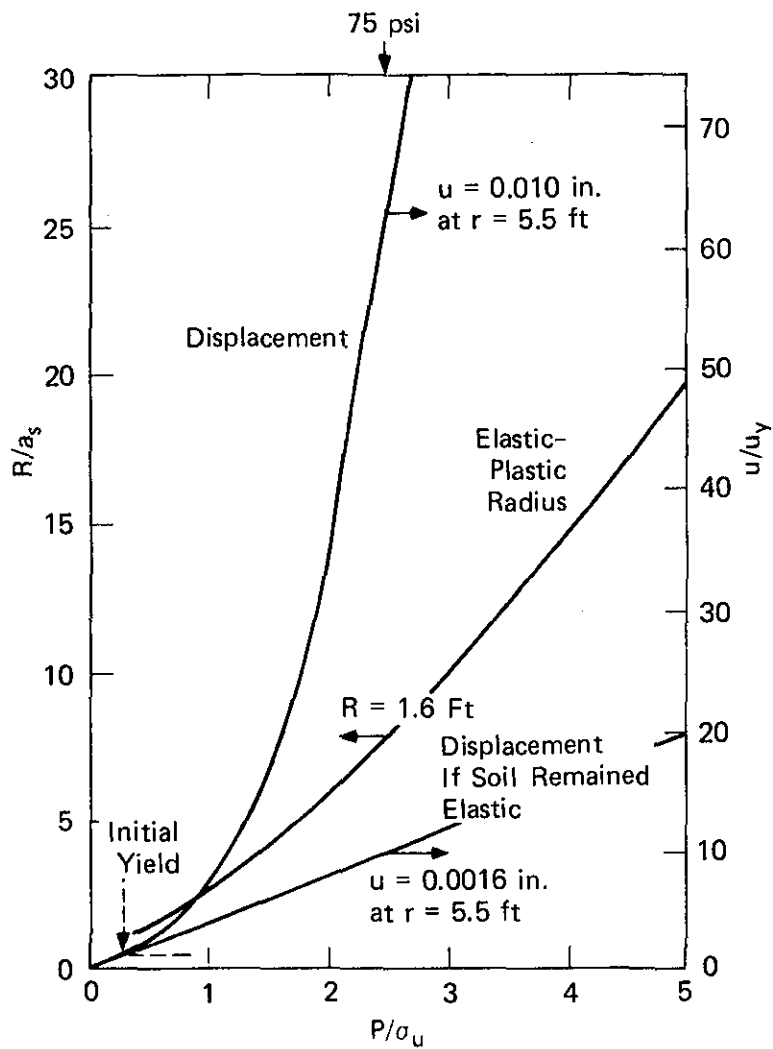
FIGURE 13 SINGLE-SOURCE DISPLACEMENT AND ELASTIC-PLASTIC
RADIUS VERSUS PRESSURE

Numerical values for soil and source configuration at Camp Parks.

36

displacement for plastic deformation is 35.4 times that for a hypothetical elastic deformation.

Tests on soil samples from Camp Parks gave an unconfined compressive strength near 30 psi. Thus, the soil would have yielded at P_s = 30/4 = 7.5 psi. The displacement 5.5 ft from the single source (the accelerometer location in the single-source tests) for P_s = 7.5 psi is u_y = 0.00016 in., found from Eq. (8). This displacement at the example pressure of P_s = 75 psi, from Eq. (7), is $u = u_y(8)^2$ = 0.010 in. This is still a very small displacement.

From a practical standpoint, the displacement from a single source will always be small. With properties measured for the Camp Parks soil, which are typical of many soils, the displacement given by Eq. (4) at radius r is $u = 0.002\ R^2/r$, where R is the radius of the elastic-plastic boundary. If we are to have elastic-free-field response at the test structure location, we must have R < r. Thus, u < 0.002 r.

B. __Array__

From the displacement expression given by Eq. (4), we conclude that to increase the displacement in the structural test area, the characteristic dimension of the elastic boundary at which loading is applied must be increased. An array of sources accomplishes this objective while also keeping the source pressure and plastic region reasonably small. This is shown schematically in Figure 14. Pressure is applied in each source until the plastic radius R around each source interacts with adjacent sources. The result is an overall elastic-plastic interface for the array that is approximately elliptical, with minor diameter s and major diameter ns, where n is the number of sources at spacing s. For simplicity, the individual plastic boundaries around the sources are shown as circles, and the interaction between sources is neglected for the present. To estimate quantitative results, we further assume that the elliptical approximation is valid when these circles make first contact, at R = s/2 as shown in the figure.

37
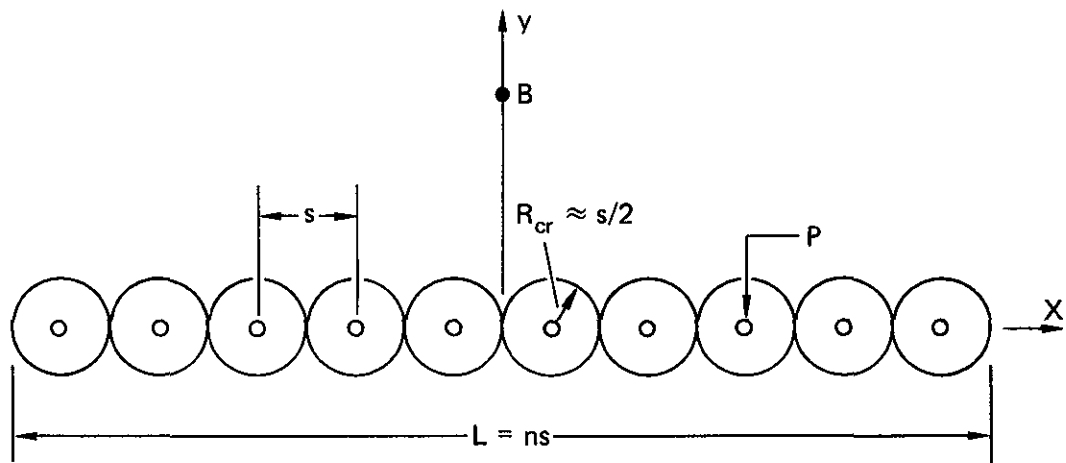
FIGURE 14 ARRAY GEOMETRY

MA-7556-12

38

Appendix E describes elastic stresses and displacements in the field around an elliptical hole under pressure P_e. The central displacement perpendicular to the array at a distance $y = 0.34$ ns (shown by point B in Figure 14, and corresponding to a 10-ft standoff for the 30-ft array in the tests) is

$$u = \frac{P_e(1 + \nu)}{E} \ (a + b) \tag{9}$$

where a and b are the major and minor radii of the ellipse. In our idealization, $a + b = (ns + s)/2$. Comparison of Eq. (9) with Eq. (4) shows that in going from a single source to an array the characteristic length multiplying either $P_y(1 + \nu)/E$ or $P_e(1 + \nu)/E$ has been increased from R^2/r to $a + b$. With $R = s/2$ and standoff $r = y = 0.34$ ns (10 ft for the array tested) the length ratio is

$$\frac{(a + b) \ r}{R^2} = \frac{1/2(ns + s)(0.34 \ ns)}{(s/2)^2} = 0.68 \ (n^2 + n) \tag{10}$$

For the 10-source array in the tests (n = 10), this ratio is 75. Thus, if the pressure P_e, on the ellipical elastic boundary of the array, was the same as the pressure P_y on the circular elastic boundary of a single source, the displacement at $r = y = 0.34$ ns would be 75 times higher for a 10 source array than for the single source--a clear reason for testing with an array.

Of course, equating P_y and P_e is only valid for a source pressure, P_s, corresponding to $R = s/2$, where each elastic-plastic single source boundary (at $r = R$) moves out to reach the hypothetical boundary of the ellipse (at $y = s/2$). Even then, it is a rough approximation because it neglects the complex plastic interaction between the sources. Results of a finite element calculation are given in Section IV-C that show the relationship between the source pressure, P_s, and the pressure on the elliptical boundary, P_e, with the complex plastic interaction of the sources taken into account. Once the relationship between P_s and P_e is known, the solution of the elastic stress and displacement fields around an elliptical hole (given in Appendix E) can be used to estimate the stresses and displacements around the array.

39

C. Finite Element Calculation of Source Interaction

Figure 15 shows the finite element grid used to model an individual source in an array. A Mohr-Coulomb, elastic-perfectly plastic material model was used to represent the soil. Symmetry boundaries were placed along the lines of symmetry of the source and along the line of symmetry between the sources. The elliptical boundary at the minor axis was represented by a series of elastic springs that account for the finite length of the array.

The stiffness of these elastic springs was determined from the pressure/displacement relation for the pressurized elliptical hole given in Appendix E, as follows: On the boundary of the ellipse the displacement, u_B, along the minor axis is given by

$$u_B = 2.6 \frac{P_e(1 + \nu)}{2E} (a + b) \tag{11}$$

Substitution of $ns/2$ for $a + b$ gives

$$u_B = \frac{P_e(1 + \nu)(ns)}{1.54 \, E} \tag{12}$$

The spring stiffness, k, is given by

$$k = \frac{P_e}{u_B} = \frac{1.54 \, E}{(1 + \nu)(ns)} \tag{13}$$

With $\nu = 0.25$,

$$k = \frac{1.23 \, E}{ns}$$

The width of the grid was chosen to be one-half the source spacing s. The length chosen is large enough that boundary stresses at the springs are nearly uniform. After one iteration this length was set at as $0.85s$.

Appendix E describes elastic stresses and displacements in the field around an elliptical hole under pressure P_e. The central displacement perpendicular to the array at a distance $y = 0.34$ ns (shown by point B in Figure 14, and corresponding to a 10-ft standoff for the 30-ft array in the tests) is

$$u = \frac{P_e(1 + \nu)}{E} \ (a + b) \tag{9}$$

where a and b are the major and minor radii of the ellipse. In our idealization, $a + b = (ns + s)/2$. Comparison of Eq. (9) with Eq. (4) shows that in going from a single source to an array the characteristic length multiplying either $P_y(1 + \nu)/E$ or $P_e(1 + \nu)/E$ has been increased from R^2/r to $a + b$. With $R = s/2$ and standoff $r = y = 0.34$ ns (10 ft for the array tested) the length ratio is

$$\frac{(a + b) \ r}{R^2} = \frac{1/2(ns + s)(0.34 \ ns)}{(s/2)^2} = 0.68 \ (n^2 + n) \tag{10}$$

For the 10-source array in the tests $(n = 10)$, this ratio is 75. Thus, if the pressure P_e, on the ellipical elastic boundary of the array, was the same as the pressure P_y on the circular elastic boundary of a single source, the displacement at $r = y = 0.34$ ns would be 75 times higher for a 10 source array than for the single source--a clear reason for testing with an array.

Of course, equating P_y and P_e is only valid for a source pressure, P_s, corresponding to $R = s/2$, where each elastic-plastic single source boundary (at $r = R$) moves out to reach the hypothetical boundary of the ellipse (at $y = s/2$). Even then, it is a rough approximation because it neglects the complex plastic interaction between the sources. Results of a finite element calculation are given in Section IV-C that show the relationship between the source pressure, P_s, and the pressure on the elliptical boundary, P_e, with the complex plastic interaction of the sources taken into account. Once the relationship between P_s and P_e is known, the solution of the elastic stress and displacement fields around an elliptical hole (given in Appendix E) can be used to estimate the stresses and displacements around the array.

C. Finite Element Calculation of Source Interaction

Figure 15 shows the finite element grid used to model an individual source in an array. A Mohr-Coulomb, elastic-perfectly plastic material model was used to represent the soil. Symmetry boundaries were placed along the lines of symmetry of the source and along the line of symmetry between the sources. The elliptical boundary at the minor axis was represented by a series of elastic springs that account for the finite length of the array.

The stiffness of these elastic springs was deterimined from the pressure/displacement relation for the pressurized elliptical hole given in Appendix E, as follows: On the boundary of the ellipse the displacement, u_B, along the minor axis is given by

$$u_B = 2.6 \; \frac{P_e(1 + \nu)}{2E} \; (a + b) \tag{11}$$

Substitution of ns/2 for a + b gives

$$u_B = \frac{P_e(1 + \nu)(ns)}{1.54 \; E} \tag{12}$$

The spring stiffness, k, is given by

$$k = \frac{P_e}{u_B} = \frac{1.54 \; E}{(1 + \nu)(ns)} \tag{13}$$

With $\nu = 0.25$,

$$k = \frac{1.23 \; E}{ns}$$

The width of the grid was chosen to be one-half the source spacing s. The length chosen is large enough that boundary stresses at the springs are nearly uniform. After one iteration this length was set at as 0.85s.

FIGURE 15   FINITE ELEMENT GRID FOR CODE CALCULATION SHOWING
THE RELATION BETWEEN SOURCE PRESSURE AND PRESSURE
ON THE ELLIPTICAL BOUNDERY

MA-7556-37

41

Code calculations were performed with the finite element code NONSAP, using the model described above. Several parameters were varied from a set of baseline values. These parameters included the source radius a_s, the unconfined compressive strength of the soil σ_u, and the friction angle ϕ. (The friction angle was varied at a constant cohesion.)

Figure 16 shows the results of five of these code calculations. Boundary pressure P_e is shown as a function of source pressure P_s. Run 1 was performed for the baseline values of a_s = 3 in., n = 10, s = 36 in., E = 5000 psi, σ_u = 30 psi, and ϕ = 30°. (In the 1/3-scale array tests the source radius a_s started at 2 in. and increased to about 4 in., primarily because of local soil compressibility, a factor not accounted for in the Mohr-Comloub soil model). In Run 2 a value of a_s = 2 in. was used, and in Run 3 a value of a_s = 6 in. was used. For both Runs 2 and 3 all the other parameters remained at the baseline values. In Run 4 the only parameter changed from the baseline values was σ_u, which was decreased from 30 to 15 psi. In Run 5 the friction angle was changed from a baseline value of 30° to 15°; this change was made at a constant soil cohension, requiring that the unconfined compressive strength also changed from a baseline value of 30 to 22 psi.

In all cases the ellipse boundary pressure increases very slowly until a critical source pressure is reached; it then increases rapidly. Examination shows that at the critical source pressure the elastic-plastic radius is at about 12 to 14 in. This fits with an intuitive observation that a critical source pressure is reached when the plastic interaction between the sources becomes strong or, stated differently, when the plastic radius approaches half the source spacing (s/2 = 18 in. in all cases). Until the source pressure reaches this critical value, the array is not being used to full advantage.

The effect of varying the various parameters on the critical source pressure is shown in Figure 16. Increasing the source diameter decreases the critical source pressure, whereas decreasing it increases the critical source pressure (compare Runs 1, 2 and 3). The unconfined compressive strength of the soil and the critical source pressure appear to be
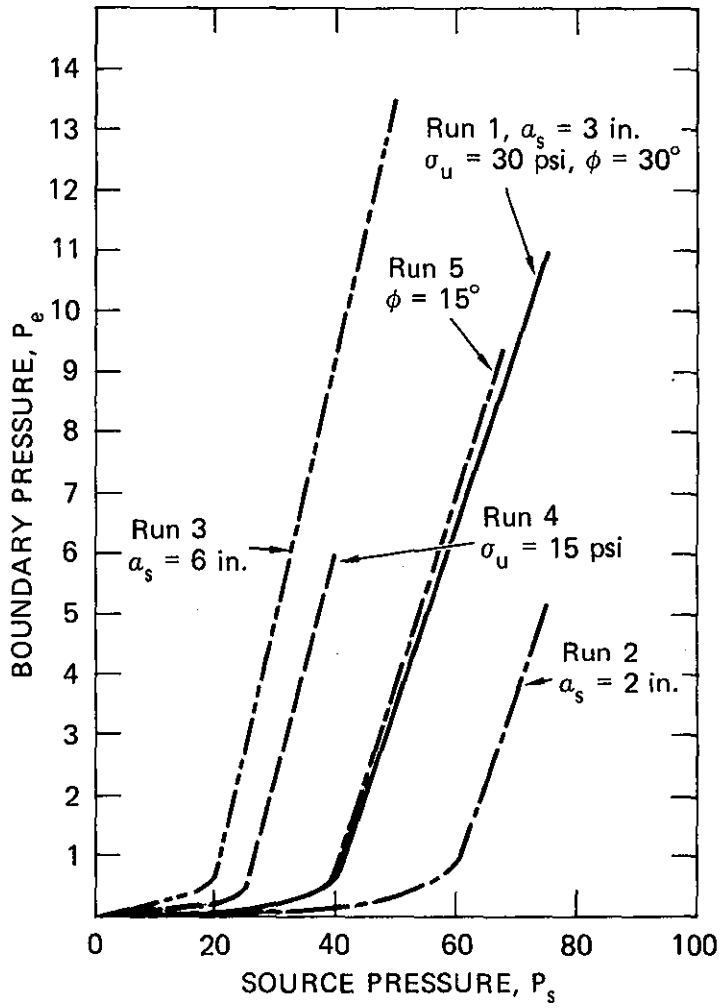
MA-7556-38

FIGURE 16   CODE CALCULATIONS SHOWING THE RELATION BETWEEN
SOURCE PRESSURE AND PRESSURE ON THE ELLIPTICAL
BOUNDARY

43

related to each other in a one-to-one manner (compare Runs 1 and 4), but, the friction angle of the soil appears to have little effect (compare Runs 1 and 5).

If we use the baseline calculation to relate P_e to P_s, we find for P_s = 75 psi that P_e = 11 psi. We can use this value of P_e (and values of E = 5000 psi, ν = 0.25) in Eq. (9) to calculate the displacement at a 10-ft standoff from a 10-source array to be 0.5 in., a useful level for testing. (Note that the displacement at a 5.5-ft standoff from a single source was calculated to be only 0.01 in.).

In summary, the finite element calculation described above allows us to relate the source pressure to the pressure on the elliptical boundary, with both the interaction of the sources and the finite length of the array taken into account. This relation can be combined with the elastic solution of stress and displacement around an elliptical hole (given in Appendix E) to predict stress and displacement around the array. The calculation also shows that a critical source pressure exists and that the array should be operated above that pressure to achieve the full benefit of the array geometry. This critical pressure is a function of both the array geometry and the soil properties.

D.   Limitation of the Theory and Future Code Calculations

In Section VI we compare the results of the theory given above with the 1/3-scale array experiments. We find that the theory and experiments agree well qualitatively but that quantitatively they differ by a factor of about 2. We note three primary reasons for this difference:

  (1) The quasi-static theory neglects the dynamic response
       and thus introduces some error at the scale of the
       complete array.

  (2) The plane strain theory neglects the presence of the
       soil free surface and the finite depth of the array.

  (3) The elastic, perfectly-plastic soil model only
       approximates true soil behavior.

Nevertheless, the theory gives a reasonable picture of the response mechanisms taking place, and of the relationships between a single source and an array. It also shows how the source and soil parameters affect response, and hence it gives a guide to use for improving the technique.

More complete theoretical analyses that treat these shortcomings, both individually and in appropriate groups as theoretical complexity is increased, can be performed with a finite element code. The solution for an infinite surface crack in an elastic half-space can be used to examine the effect of the soil free surface and the finite depth of the source. Some results from analytical solution of this problem exist in the literature for the static case, but the results we need can probably be more easily determined by using a finite element code. Figure 17(a) shows the idealized theoretical model for an infinite surface crack.

The solution for a finite surface crack in an elastic half-space (Figure 17b) will also be useful. This solution exists in the literature as well, but, again, the computations are quite lengthy. For this reason it is more expeditions to use a finite element code to determine the solution. The code can be run both statically and dynamically to determine the effect of dynamic response of the soil on the displacement.

Inclusion of more complex material models is also possible with finite element codes. The most important addition to the material model is probably the allowance for a variable elastic modulus. Soil compaction might also be an important effect to be included. The solution of the two elastic problems and the inclusion of a variable modulus soil model will be addressed in next year's program.
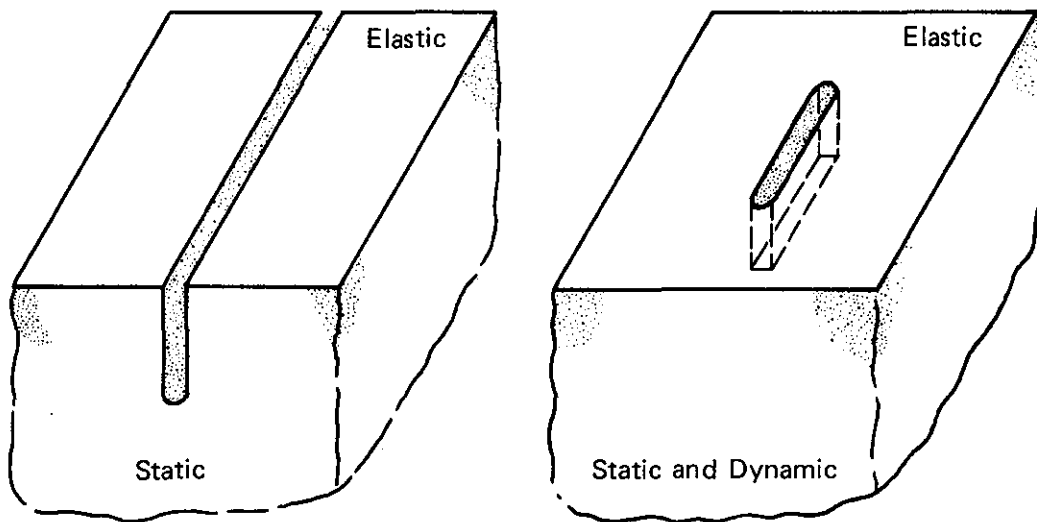
(a) **INFINITE SURFACE CRACK IN ELASTIC HALF-SPACE**

(b) **FINITE SURFACE CRACK IN ELASTIC HALF-SPACE**

MA-7556-22A

FIGURE 17 THEORETICAL MODELS FOR MORE ACCURATE SOIL RESPONSE CALCULATIONS

V ARRAY TEST RESULTS

A. Test Description

Figure 18 shows the layout used for seven array tests; ten sources were spaced on 3-ft centers. The sources and the source placement technique were the same as that for the single-source test described in Section III. The measurement designation system is given in Figure 4. Bladder pressure and bladder expansion were measured for two of the 10 sources, one near the center and one at the outer edge of the array. At the 7.5-ft depth, three accelerometers were located along the array centerline at standoff distances of 6, 10, and 15 ft, and two accelerometers were placed 6 ft to the left and 6 ft to the right of the array centerline at a 6-ft standoff. At the 2-ft depth, three accelerometers were located 1.5 ft off the array centerline at the same standoff distances as the deeper accelerometers (6, 10, and 15 ft).[*] All of these accelerometers were oriented with their sensing axis horizontal and perpendicular to the array, with the positive direction away from the array. A single vertically oriented accelerometer was located at a standoff of 10 ft and a depth of 1 ft. The sensing direction was oriented with the positive direction upward.

Soil stress was measured both at a 3-ft standoff (near the equivalent ellipitcal boundary) and at a 10-ft standoff (where a test structure would be located). The sensing direction was horizontal and perpendicular to the array and the depth was 2.5 ft for both gages.

Figure 19 shows three of the ten sources in the array, taken before hookup of the detonation system. The mylar diaphragm used to seal the exhaust vent can be seen.

---

[*] In the first four tests the accelerometer at a 2-ft depth and 15-ft standoff was not included, and in the last three tests the accelerometers 6-ft to the left and 6-ft to the right of the array centerline were not included.
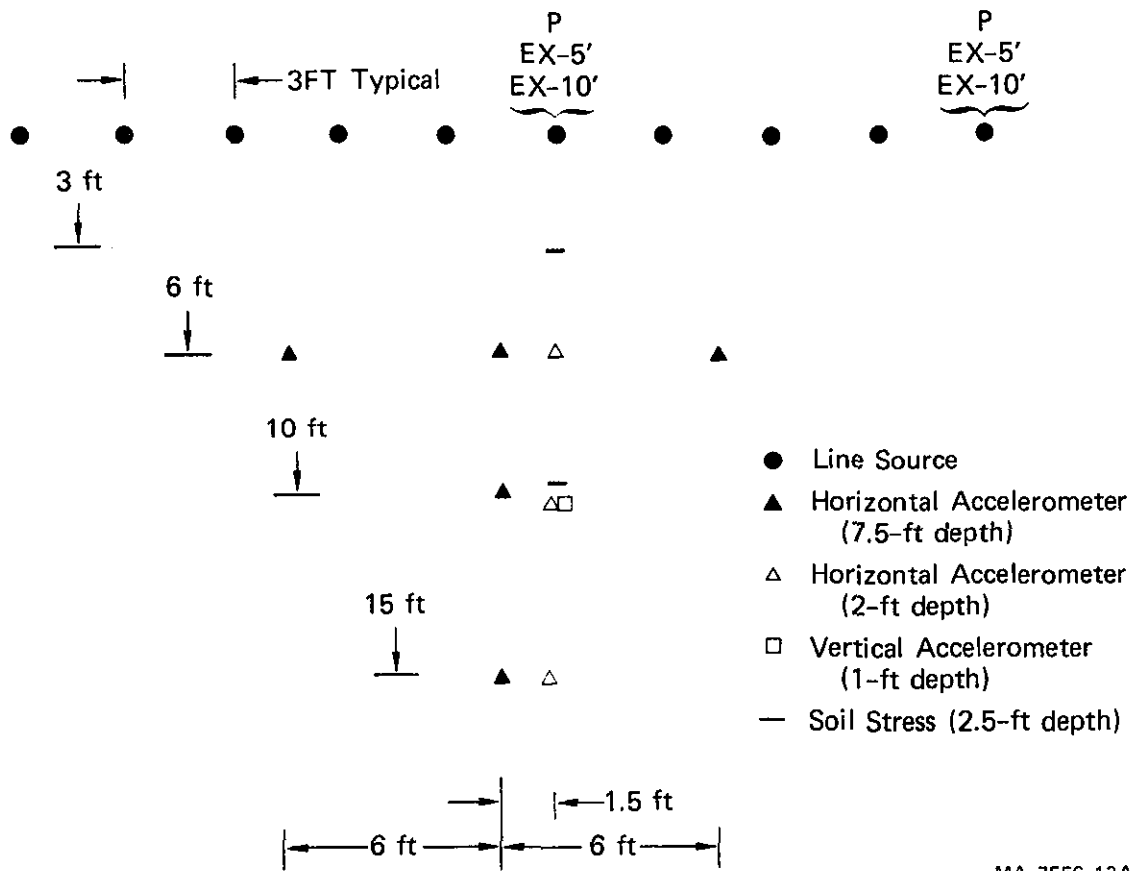
FIGURE 18   ARRAY LAYOUT (PLAN VIEW)

MP-7556-29

FIGURE 19   CLOSE-UP OF THREE SOURCES IN ARRAY
(Before hook-up of detonation system)

Figure 20 shows a view of the complete array after hookup of the detonation system. A steel I-bean was placed behind the row of charges to shield the sources from a small strand of explosive cord that was used to initiate the primary charge in each source. This cord was in turn initiated with a detonator at the center of the array. Because the detonation rate in the cord is 22 ft/ms, the central sources were detonated 0.6 ms ahead of those at the ends of the array. However, because this differential is quite small when compared to the 150-ms complete pulse, the detonation was in effect simultaneous.

A second small, continuous, explosive cord was tied to each Mylar diaphragm. This cord was also detonated at its center, rupturing each Mylar diaphragm either at 60 or 100 ms after the primary detonation, depending on the test.

Table 1 gives the parameters that were varied in the seven tests and states the primary objective of each test. In the comments column a guide showing the orginization of the remainder of this section is given.

B. Results of a Typical Test

Figure 21 shows the bladder pressure, soil stress, and bladder expansion from the array test (Test 132) with 2.5 lb/ft of PETN (0.25 lb/source) and a canister vent area of 0.60 in.^{2} (the largest vent area tested). In this test the Mylar exhaust diaphragms were ruptured 60 ms after the primary detonation. (The diaphragm was ruptured at t = 40 ms for the single source.) Comparison of the records in Figure 21 for an array with those in Figure 7 for a single source indicates that source pressures and soil stresses differ little between a single source and an array. As discussed below, the ground motion for an array does differ significantly from that produced by a single source.
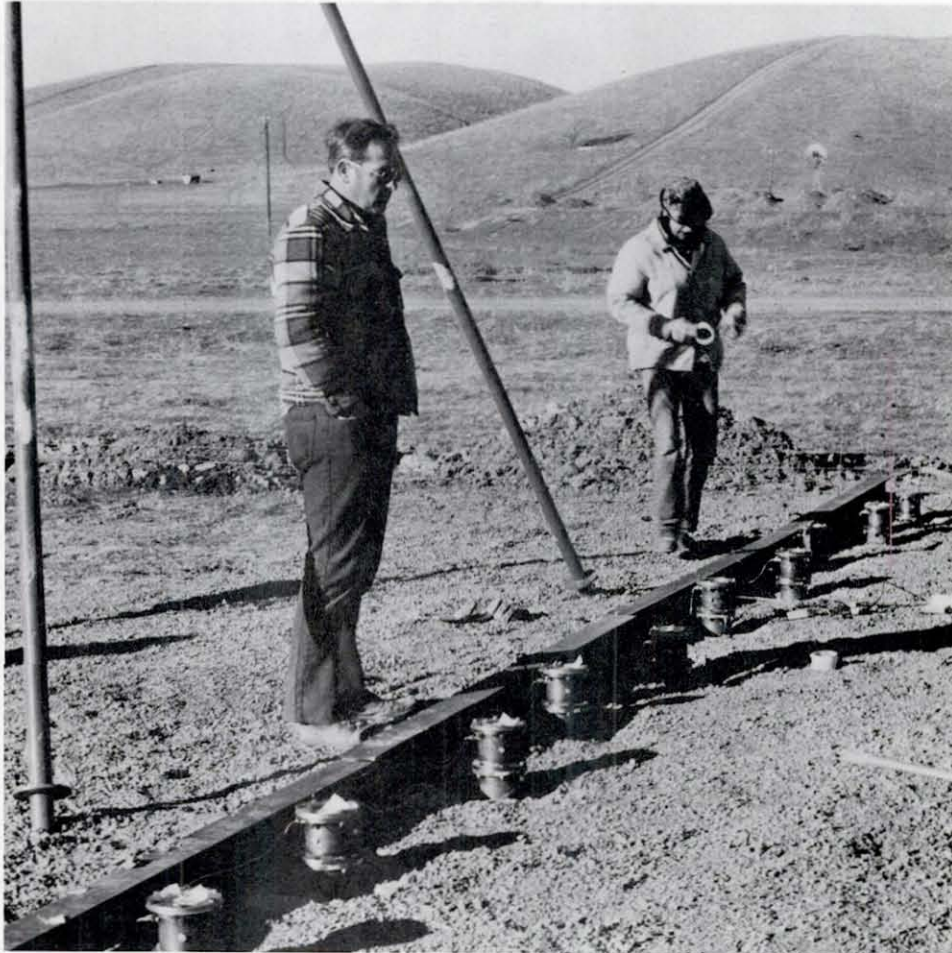
MP-7556-14

FIGURE 20   VIEW OF LINE SOURCE ARRAY

Table 1

OUTLINE OF ARRAY TESTS

Test No.	Charge Weight (1b/source)	Charge Type	Canister Vent Area (in.^{2}/source)	Primary Objective	Comparison
127	0.17	PETN	0.30	Initial array test	
130	0.25	PETN	0.30	Effect of increased weight	
131	0.25	PETN	0.15	Effect of reduced canister vent area	Vent Area Comparison, Section V-C
132	0.25	PETN	0.60	Effect of increased canister vent area	PETN/Blue Dot Comparison, Section V-D
156	0.25	Blue Dot	0.60	Comparison of propellant and explosive charge	
157	0.37	Blue Dot	0.60	Increase charge weight toward limit	Charge Weight Comparison, Section V-E
158	0.62	Blue Dot	0.60	Increase charge weight toward limit	

52
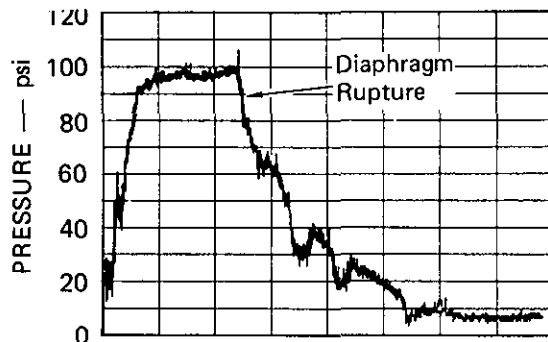
(a) BLADDER PRESSURE (Source 6)
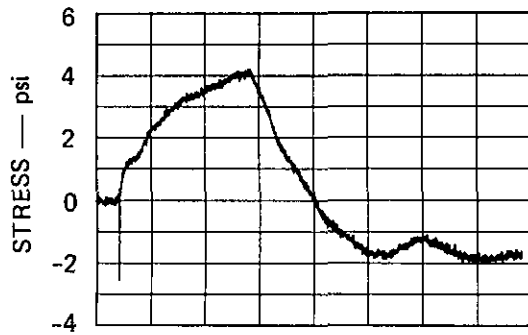
(b) SOIL STRESS 10 FT FROM
ARRAY (SP10, 1.5, 2.5)
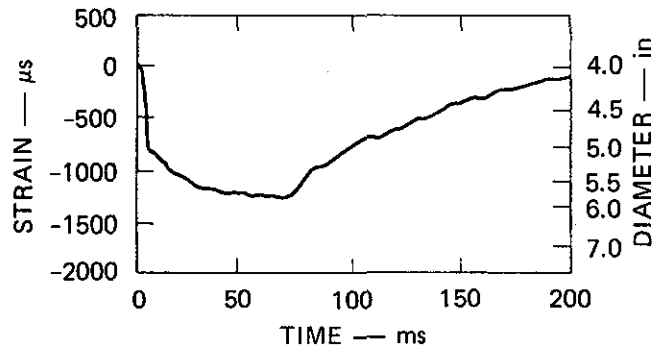
(c) BLADDER EXPANSION
(Source 6, 10 ft depth)

MA-7556-15

FIGURE 21   BLADDER PRESSURE, SOIL STRESS,
AND BLADDER EXPANSION IN ARRAY
TEST

Test 132, 0.25 lb/source PETN and
Canister Vent Area 0.60 in.^{2}/source

53

Comparison of Figure 21(b) with 21(a) shows that the soil stress follows the bladder pressure in shape but has a somewhat slower rise. This result is similar to that for the single-source test (Figure 7). Comparison of 21(c) with 21(a) shows that the bladder expansion also follows the bladder pressure.

Figure 22(a) and (b) show two symmetric acceleration measurements for Test 132, one made 6 ft to the left and the other 6 ft to the right of the array centerline at the 7.5-ft depth. The motion is essentially the same at the left and right location, demonstrating the uniformity of the soil and of the source response. Comparison with records in Figures 23, 24, and 25 from the central accelerometer shows that soil response is the same at the center as at the left and right locations and therefore uniform along the 12-ft span of the instrumented area. Just as in the single-source tests, the initial accelerations are very high (6g). This is again attributed to the initial sharp rise in source pressure. This rise will be reduced in future tests to match the shape required for sinusoidal acceleration more closely.

Figure 22(c) through 22(f) show the velocity- and displacement-time histories for the two symmetric accelerometer locations. In contrast to the single-source results (see Figure 8), the velocity and displacements are now appreciable.

Figure 23 shows the six accelerometer records from the array center-line for the same test (Test 132). Figures 23(a), 23(c), and 23(e), from the 7.5-ft depth, again show very high initial acceleration and frequency. These high accelerations attenuate quickly with distance [compare Figure 23(a) with 23(e)].

Figure 23(b) and 23(d) show the records from near the surface (2-ft depth). As in the single-source tests, these accelerations are lower in amplitude and frequency than those at the mid-depth of the array, a result we attribute to stress relief near the surface and to the active source length beginning at a depth of 3 ft.

54
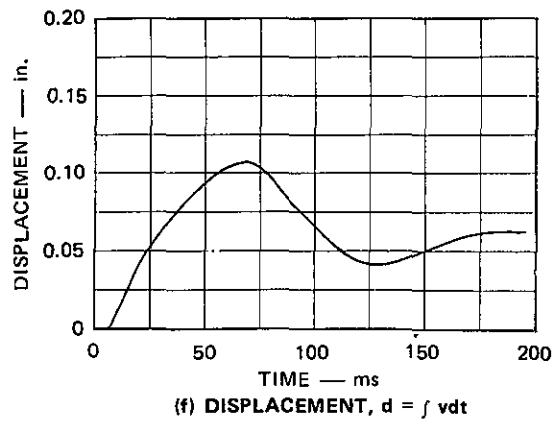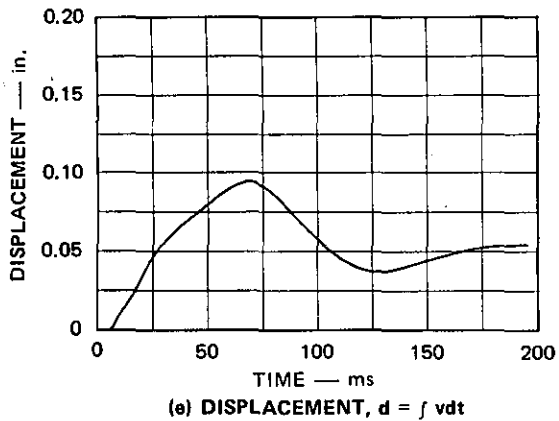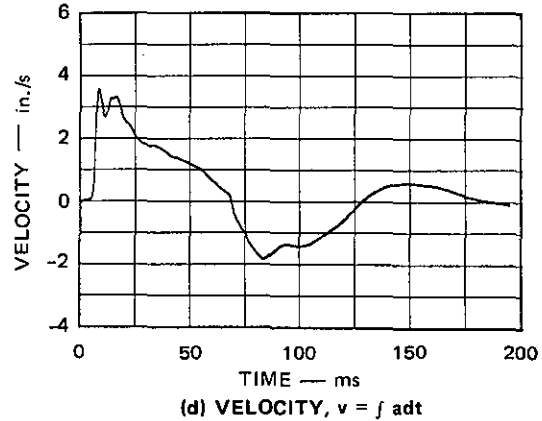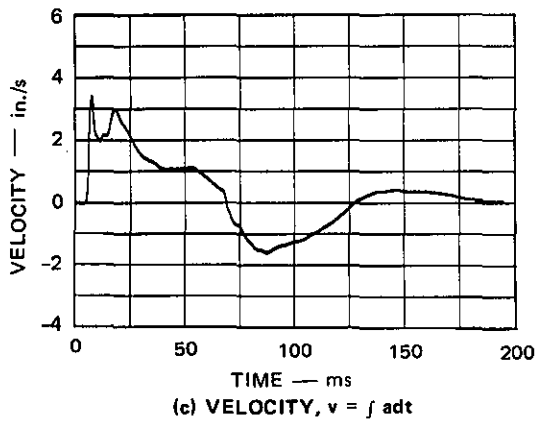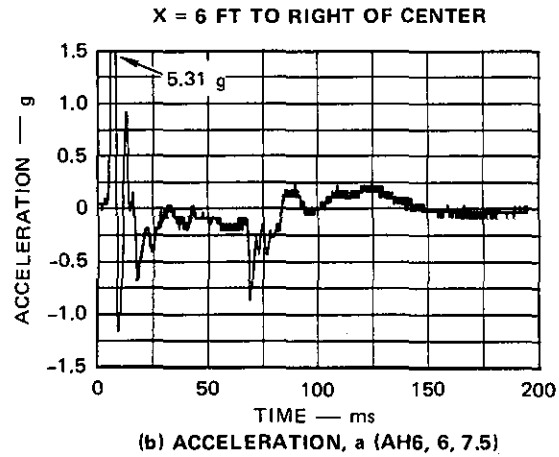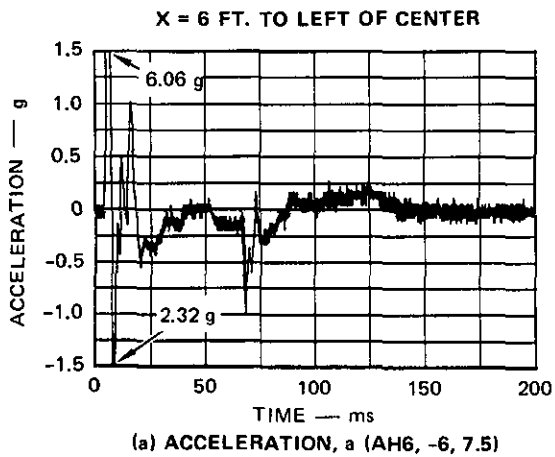
FIGURE 22   EARTH MOTION FROM ARRAY TEST, AT Y = 6 FT FROM ARRAY
AND Z = 7.5 FT DEEP

Test 132, 0.25 lb/source PETN and Canister Vent Area 0.60 in.^{2}/source

55
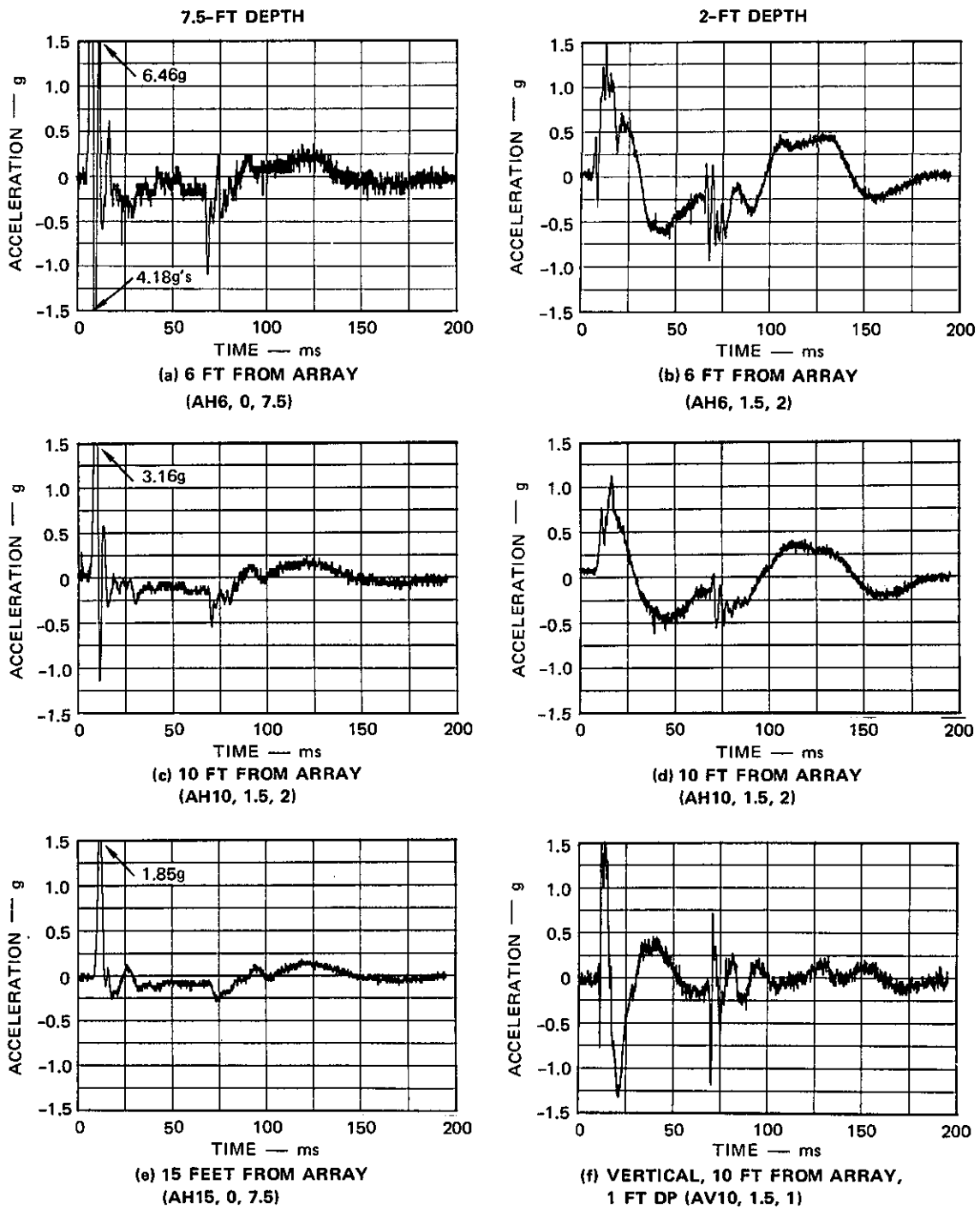
FIGURE 23   VARIATION OF ACCELERATION WITH DISTANCE AND DEPTH FOR ARRAY TEST

Test 132, 0.25 lb/source PETN and Canister Vent Area 0.60 in.^{2} source

56

Figure 23(f) shows significant vertical acceleration at a 10-ft standoff and a 1-ft depth. However, as we see below in Figure 25(f), little vertical displacement is associated with this acceleration.

Figure 24 shows the velocity-time histories calculated by integrating the six accelerometer records given in Figure 23. In contrast to the single-source results (see Figure 8), the velocities are significant both at depth and near the surface.

Figure 25 shows the displacement-time histories calculated by twice integrating the six accelerometer records given in Figure 23. Again, in contrast to the single-source results (Figure 8), the displacements are significant both at depth and near the surface. Comparison of Figures 25(a), 25(c), and 25(e) shows that with increasing distance from the array the displacement-time histories change in amplitude but not in shape. This decay in amplitude with distance follows that predicted by the quasi-static elliptical hole theory presented in Appendix A.

A close look at these displacement-time histories shows that they are quite similar in shape to the soil stress records. This can be seen from Figure 26, which shows the displacement-time and soil stress-time histories at a 10-ft standoff. Because the soil stress in turn follows the source pressure (Figure 21), we conclude that the displacement-time history in the soil can be controlled by controlling the shape and amplitude of the source pressure pulse.

Figure 27 shows a comparison of earth motion from a single source and from an array for both a 7.5-ft and 2-ft depth. Use of an array greatly enhances velocity and displacement.

C.   Comparison of Tests with Three Vent Areas

We performed array tests using three central canister vent areas. (To this point, we have discussed only the test with the largest of these vent areas—Test 132). The three different vent areas were tested in an effort to control the frequency of the earth motion by controlling the pressure rise in the bladder. Figures 28 and 29 show

7-FT DEPTH

(a) 6 FT FROM ARRAY
(AH6, 0, 7.5)

2-FT DEPTH

(b) 6 FT FROM ARRAY
(AH6, 1.5, 2)

(c) 10 FT FROM ARRAY
(AH10, 0, 7.5)

(d) 10 FT FROM ARRAY
(AH10, 1.5, 2)

(e) 15 FT FROM ARRAY
(AH5, 0, 7.5)

(f) VERTICAL, 10 FT FROM ARRAY
1 FT DP (AV10, 1.5, 1)
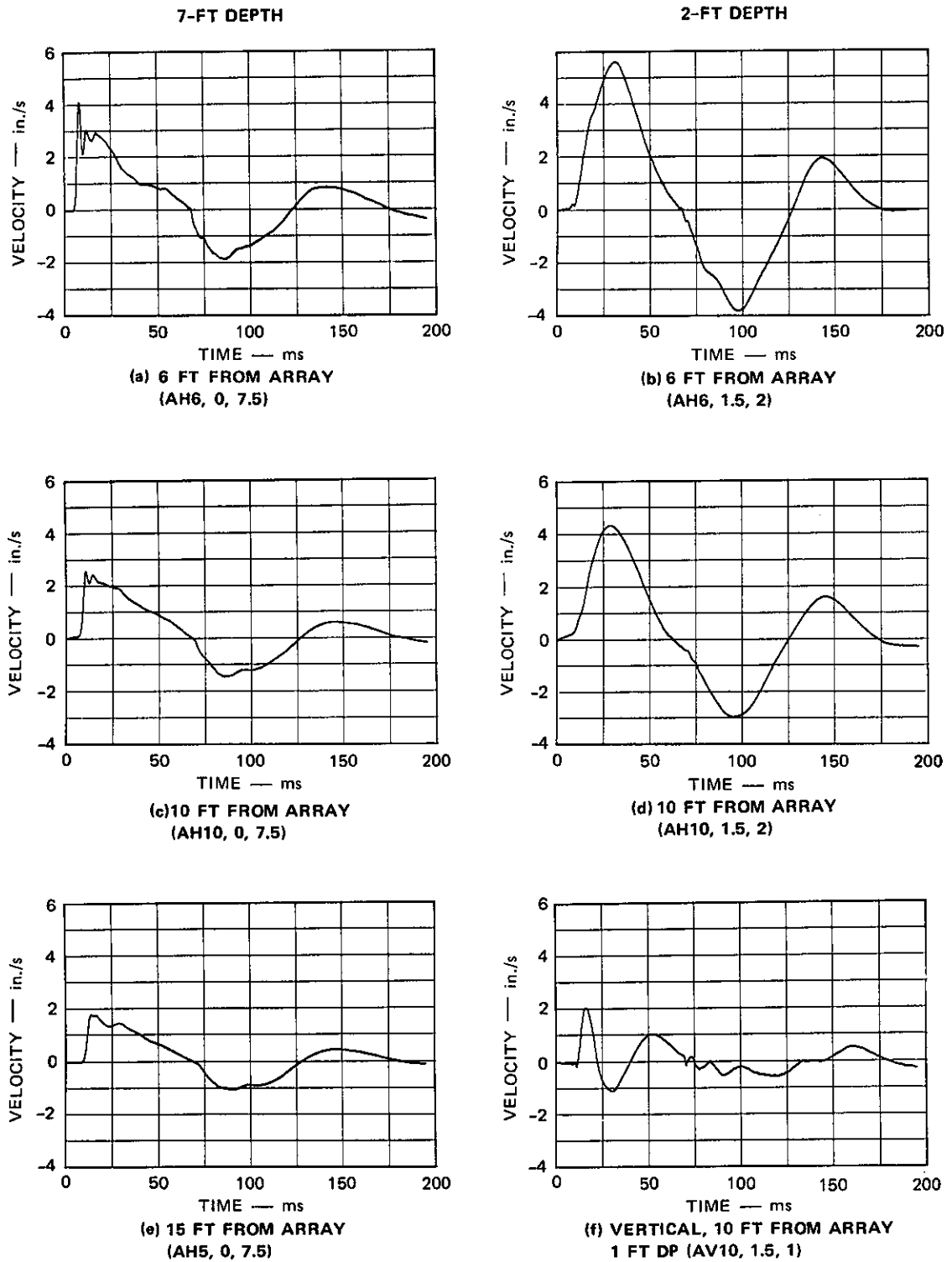
MA-7556-18

FIGURE 24   VARIATION OF VELOCITY WITH DISTANCE AND DEPTH FOR ARRAY TEST,
$v = \int adt$

Test 132, 0.25 lb/source PETN and Canister Vent Area 0.60 in.^{2}/source

7.5-FT DEPTH

2-FT DEPTH

(a) 6 FT FROM ARRAY
(AH6, 0, 7.5)

(b) 6 FT FROM ARRAY
(AH6, 1.5, 2)

(c) 10 FT FROM ARRAY
(AH10, 0, 7.5)

(d) 10 FT FROM ARRAY
(AH10, 1.5, 2)

(e) 15 FT FROM ARRAY
(AH15, 0, 7.5)

(f) VERTICAL, 10 FT FROM ARRAY,
1 FT DP (AV10, 1.5, 1.0)
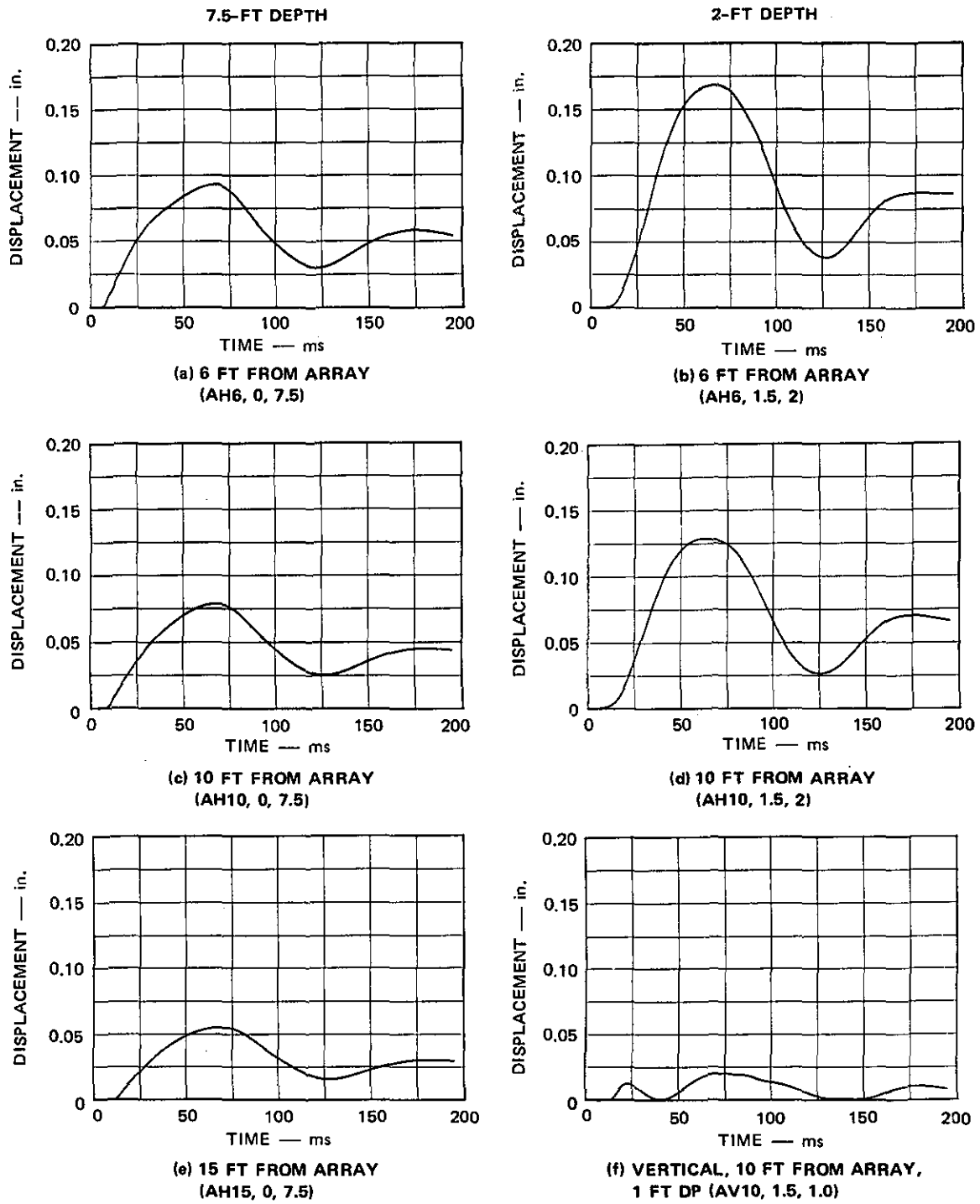
MA-7556-19

FIGURE 25   VARIATION OF DISPLACEMENT WITH DISTANCE AND DEPTH FOR ARRAY
TESTS, $d = \int v dt$

Test 132, 0.25 lb/source PETN and Canister Vent Area 0.60 in.^{2}/source

59
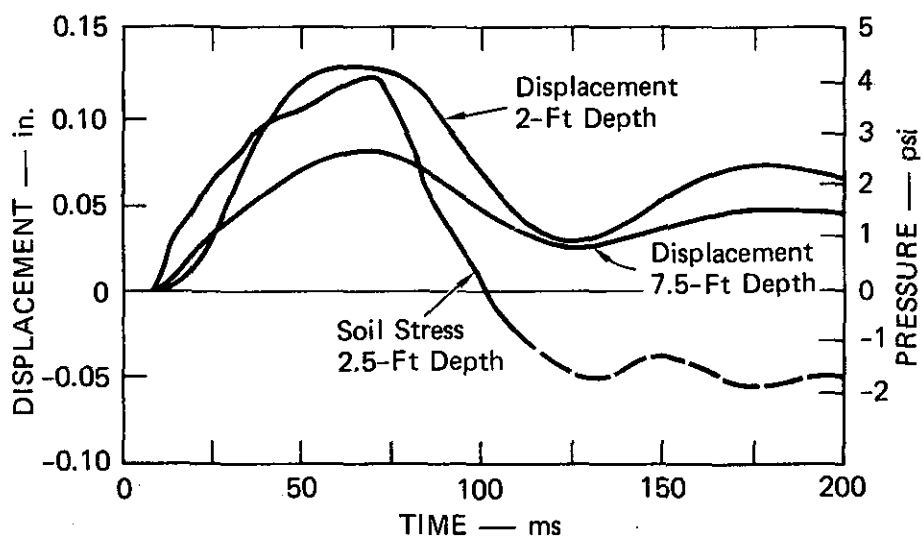
MA-7556-20A

FIGURE 26   COMPARISON OF DISPLACEMENT AND SOIL STRESS,
10 FT FROM ARRAY
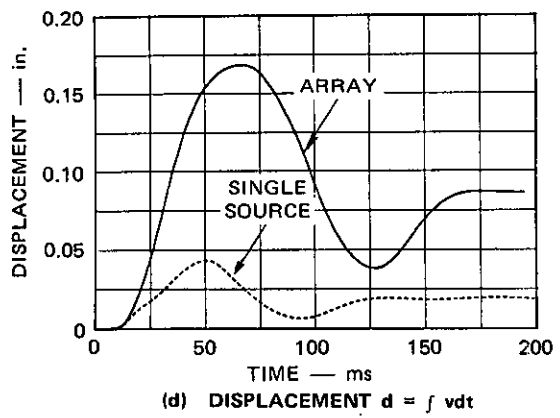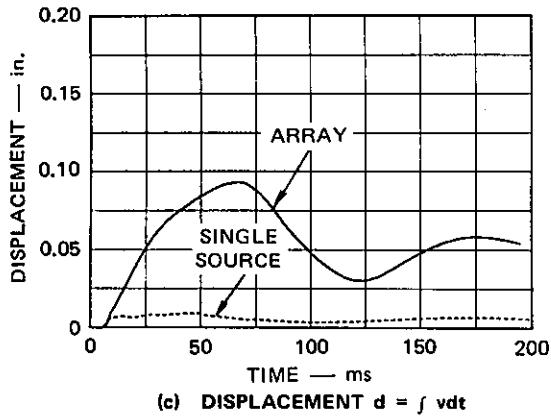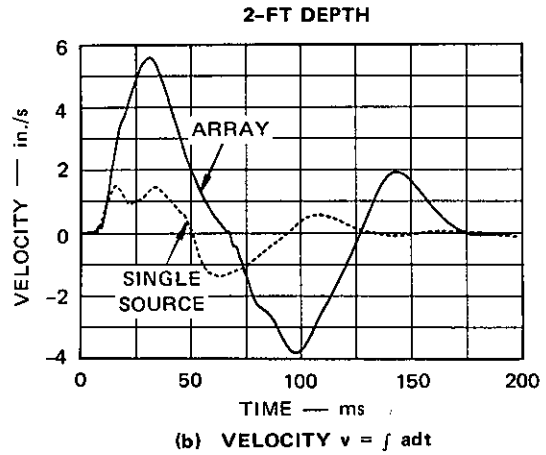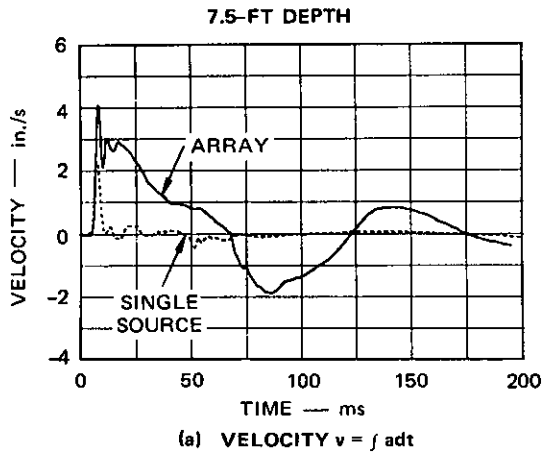
FIGURE 27   COMPARISON OF EARTH MOTION FROM SINGLE-SOURCE AND ARRAY TESTS
(5.5-FT STANDOFF FOR SINGLE SOURCE AND 6-FT STANDOFF FOR ARRAY)

Tests 125 and 132, 0.25 lb/source PETN and Canister Vent Area 0.60 in.^{2}/source

61

the key results from these three tests: Test 132; Test 131, with
one-fourth the vent area of Test 132; and Test 130, with one-half the
vent area of Test 132.

Figure 28 shows the bladder pressure and soil stress for these
three array tests. Comparison of Figures 28(a) and 28(c) with 28(e)
shows that the initial slope of the bladder pressure decreased at about
the same rate as the vent area was decreased. The peak bladder pressure
was also decreased by decreasing the vent area; this is attributed to
heat transfer to the central steel canister. (A rough estimate of
energy loss to heat transfer shows that a 50% loss can occur in 60 ms.)
This drop in bladder pressure along with the nonlinearity of soil
response accounts for the fourfold decrease in soil stress between
Figure 28(f) and 28(b).

Figure 29 shows the acceleration- and velocity-time histories for
the three array tests. Comparison of the three tests shows that
decreasing the canister vent area resulted in a decrease in the
amplitude of the ground motion, although it had little effect on the
frequency during the loading pulse (during the expansion of bladder).
This decrease in amplitude is as expected after examining the decrease
in soil stress (Figure 28).

A different phenomenon is observed during the exhaust of the
explosive products from the bladder (the unloading pulse); the pulse
period decreases as the canister vent area is decreased (although the
exhaust vent area remains the same). A reason for this can be seen
by comparing the bladder pressure records for the three array tests
(Figure 28); reducing the canister vent area results in a decrease in
bladder pressure and thus a decrease in the unloading period directly
affecting the pulse period.

Figure 30 shows compares of soil stress- and the displacement-time
histories 10 ft from the array for the three vent areas. Note that
soil stress and ground displacement have a similar period and shape,
indicating that by proper tailoring of the input pressure at high
enough levels both the period and shape can be controlled.

62

FIGURE 28 VARIATION OF BLADDER PRESSURE AND SOIL STRESS WITH CANISTER VENT AREA FOR ARRAY TESTS

0.25 lb/source PETN

63

ACCELERATION (AH6, 1.5, 2)

VELOCITY v = ∫ a dt
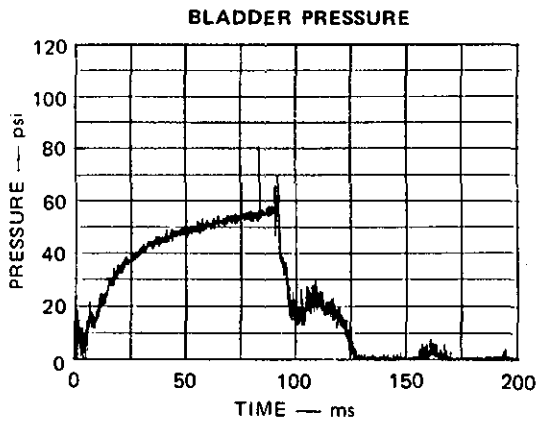
(a)   TEST 131, VENT AREA 0.15 in.^{2}/SOURCE   (b)
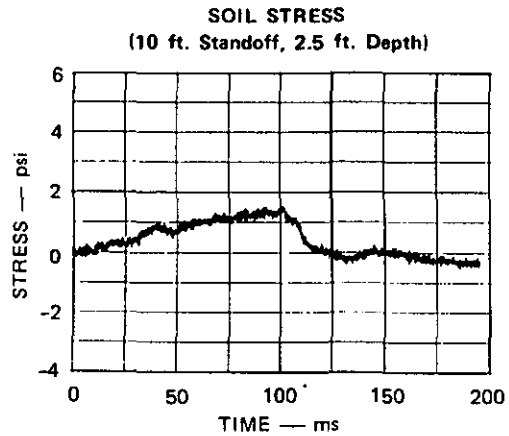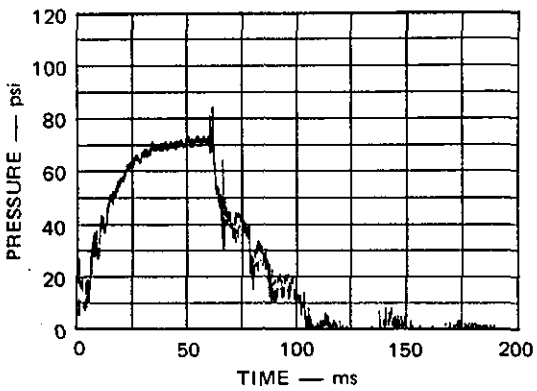
(c)   TEST 130, VENT AREA 0.30 in.^{2}/SOURCE   (d)
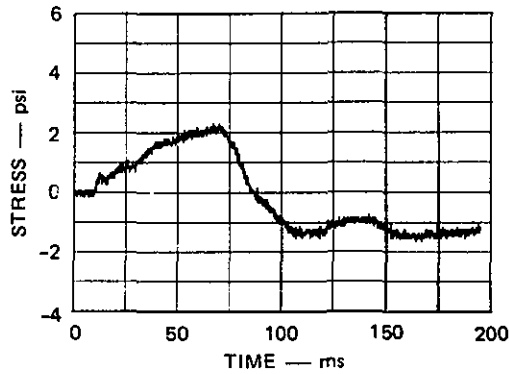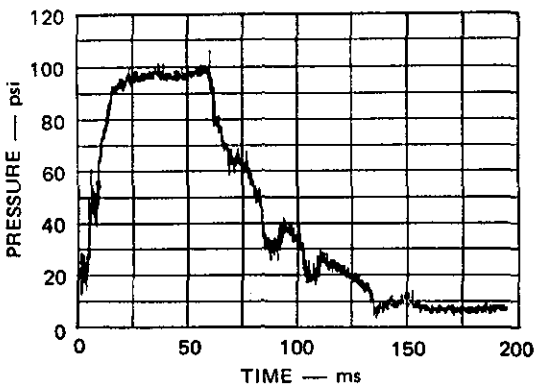
(e)   TEST 132, VENT AREA 0.60 in.^{2}/SOURCE   (f)
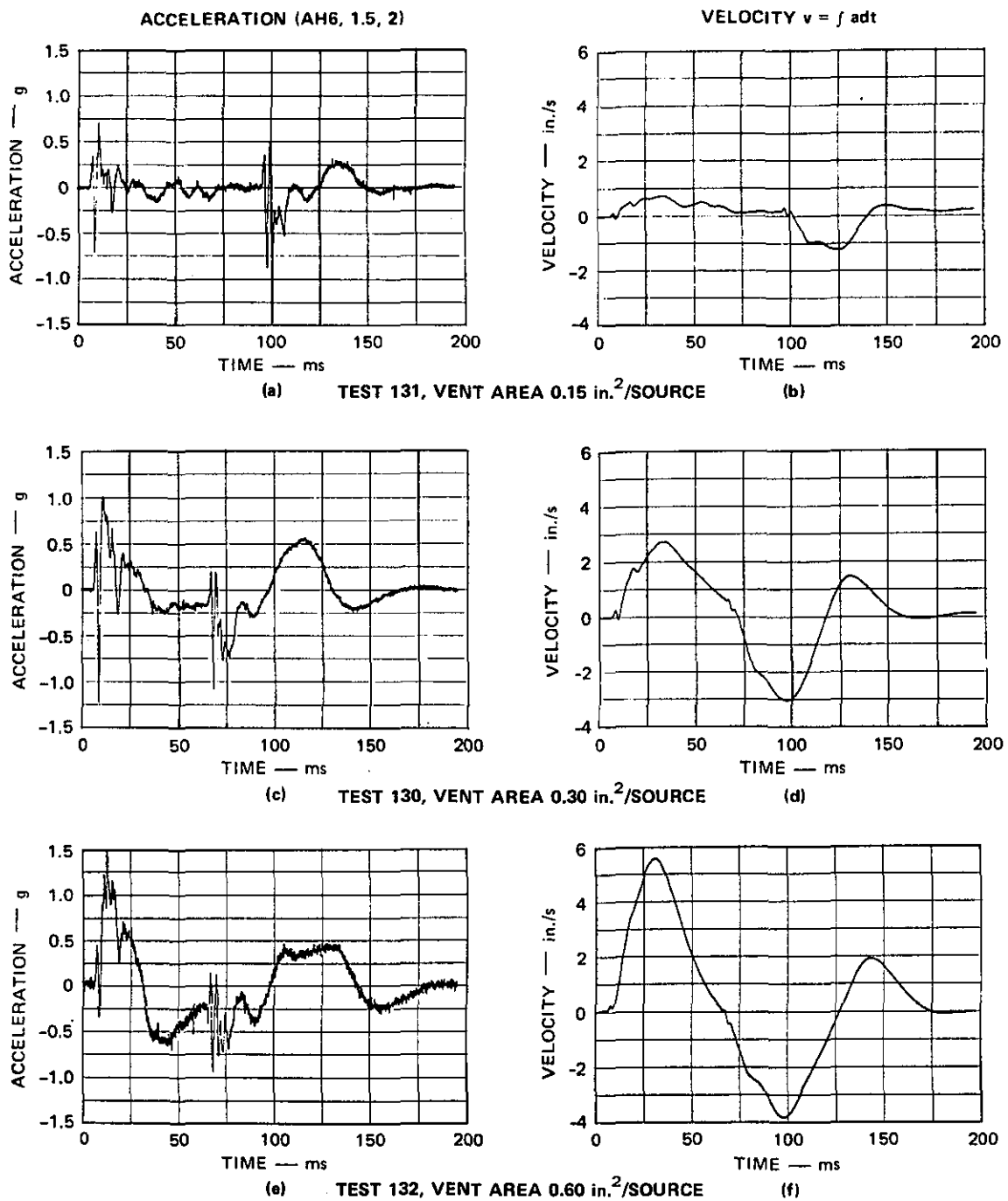
MA-7556-24A

FIGURE 29   VARIATION OF EARTH MOTION WITH CANISTER VENT AREA FOR ARRAY
TESTS

0.25 lb/source PETN, 6 ft from source, 2 ft deep

64
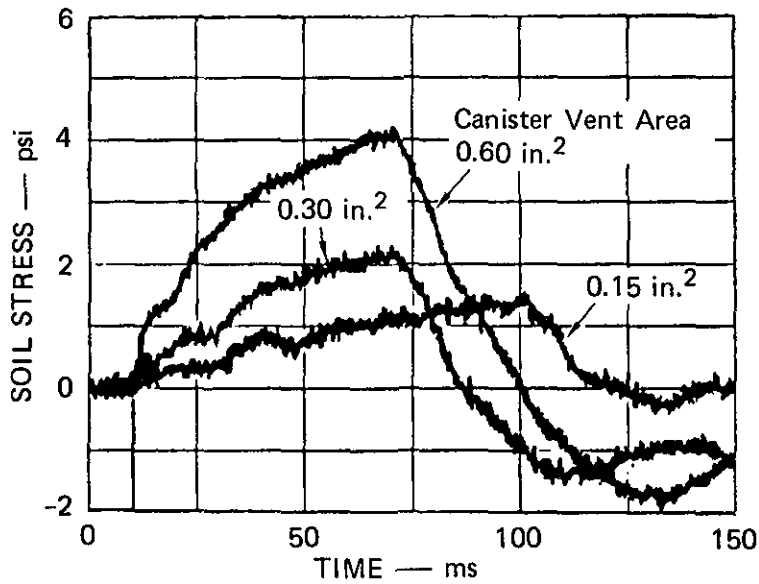
(a) SOIL STRESS — 2.5-FT DEPTH
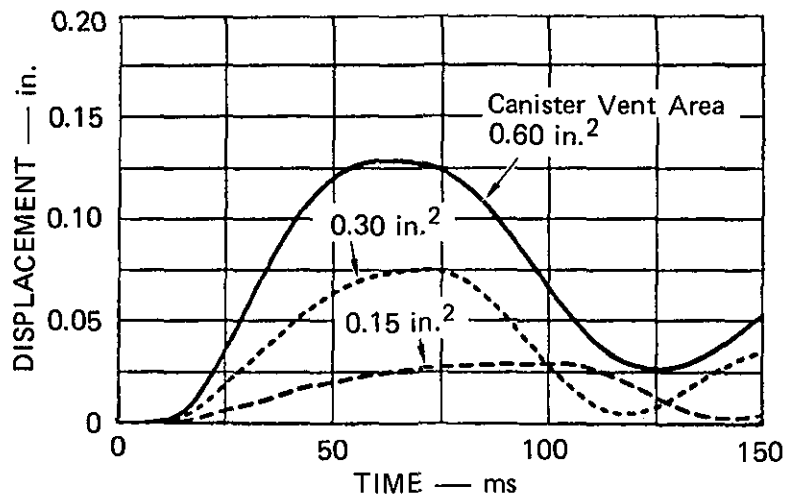
(b) DISPLACEMENT — 2-FT DEPTH

MA-7556-25A

FIGURE 30   SOIL STRESS- AND DISPLACEMENT-TIME HISTORIES
10 FT FROM ARRAY FOR THREE VENT AREA

0.25 lb/source PETN

D. Comparison of Tests Using Propellant Versus Explosive Charges in Line Source

Because propellants can release their energy through a rapid burning rather than by detonation, much lower stresses in the charge canister result. At the same time the same equilibrium canister pressure and hence same bladder pressure are produced as would be with an equal amount of explosive. Thus, a larger amount of propellant can be contained within a given charge canister than would be possible if explosives were used. In the closed chamber tests described in Appendix A, we found that propellants could provide a practicable and controllable method of pressurizing the bladder. The next step was to test propellants in the line source itself.

We performed a test (Test 156) with an amount of Blue Dot propellant equal to the amount of PETN explosive used in Test 132. For this test the array hardware was modified by adding two small ports in the aboveground portion of each source to purge air from the source and replace it with nitrogen. This is necessary because, unlike PETN, double-based propellants such as Blue Dot are not oxygen balanced. Therefore, their combustion products contain carbon monoxide (37%) and hydrogen (8%) that can burn further in the presence of air. A secondary and noncontrollable burning of these products can occur outside the charge canister if oxygen is present within the source. (This phenomenon was observed in the closed chamber tests described in Appendix A). The purging process consisted of pressurizing the source from a nitrogen bottle to 15 psig and then venting the pressurized source atmosphere. The process was repeated 3 times for each of the 10 sources.

The charge was constructed as it was in the closed chamber test. The propellant was placed in 0.875-in.-diameter paper tubes constructed with a 0.25-in.-diameter straw through the center. The tubes were filled with a measured weight of Blue Dot and sealed at each end. They were then threaded onto a 12-ft length of 25 gr/ft Primacord. For each source in Test 156, four charge tubes were equally spaced on the 12-ft length of Primacord. Each tube contained 0.062 lb of Blue Dot and was about 4 in. long.

66

Figure 31 compares bladder pressure and earth motion for the two
tests. Test 132 was performed using 0.25 lb/source of PETN explosives
and its results are described in full in Section V-B. Test 156 was
performed in the same array 7 months later using 0.25 lb/source of
Blue Dot propellant. Figure 31 shows that both the bladder pressure
and the earth motion are remarkably similar for the two tests, leading
us to conclude that propellants are a practicable pressure source.
That the array of line sources could be left in the ground for 7 months
and then be reused with such similar results indicates the repeatability
associated with the contained line source array technique.

E.   Comparisons of Tests with Three Charge Sizes

To this point, we have discussed tests that used a maximum of
0.25 lb of charge per source. Previous tests had shown that 0.25 lb
of PETN explosive was the most that could be repeatably contained within
the canister without causing its failure. Extrapolation of the closed
chamber tests described in Appendix A showed that as much as 2 lb of
propellant could be contained within the canister.

In this section we compare the results of three array tests
performed using propellant, Test 156 with 0.25 lb per source, Test 157
with 0.37 lb per source, and Test 158 with 0.62 lb per source. The
three tests were performed with the same canister vent area--0.60 in.^{2}
per source.

Figure 32 shows the bladder pressure and the soil stress at a
10-ft standoff for the three tests. Comparison of peak pressures
shows that the bladder pressure increases at a rate less than that
with which the charge is increased. For example, comparison of results
from Tests 156 and 158 shows only a 1.3-fold increase in bladder pressure
occurs with a 2.5-fold increase in charge. This result is attributed
to a substantial amount of the increased energy going to increase in
the volume of the bladder rather than simply into an increase in
bladder pressure. This volume increase is desirable since increases
in bladder volume produce ground motion.

TEST 132, 0.25 LB/SOURCE PETN

TEST 156, 0.25 LB/SOURCE BLUE DOT

(a) BLADDER PRESSURE (Source 6)

(b) BLADDER PRESSURE (Source 6)

(c) VELOCITY 7.5-FT DEPTH
(AH10, 0, 7.5)

(d) VELOCITY, 7.5-FT DEPTH
(AH10, 0, 7.5)

(e) VELOCITY, 2-FT DEPTH
(AH10, 1.5, 2.0)

(f) VELOCITY, 2-FT DEPTH
(AH10, 1.5, 2.0)
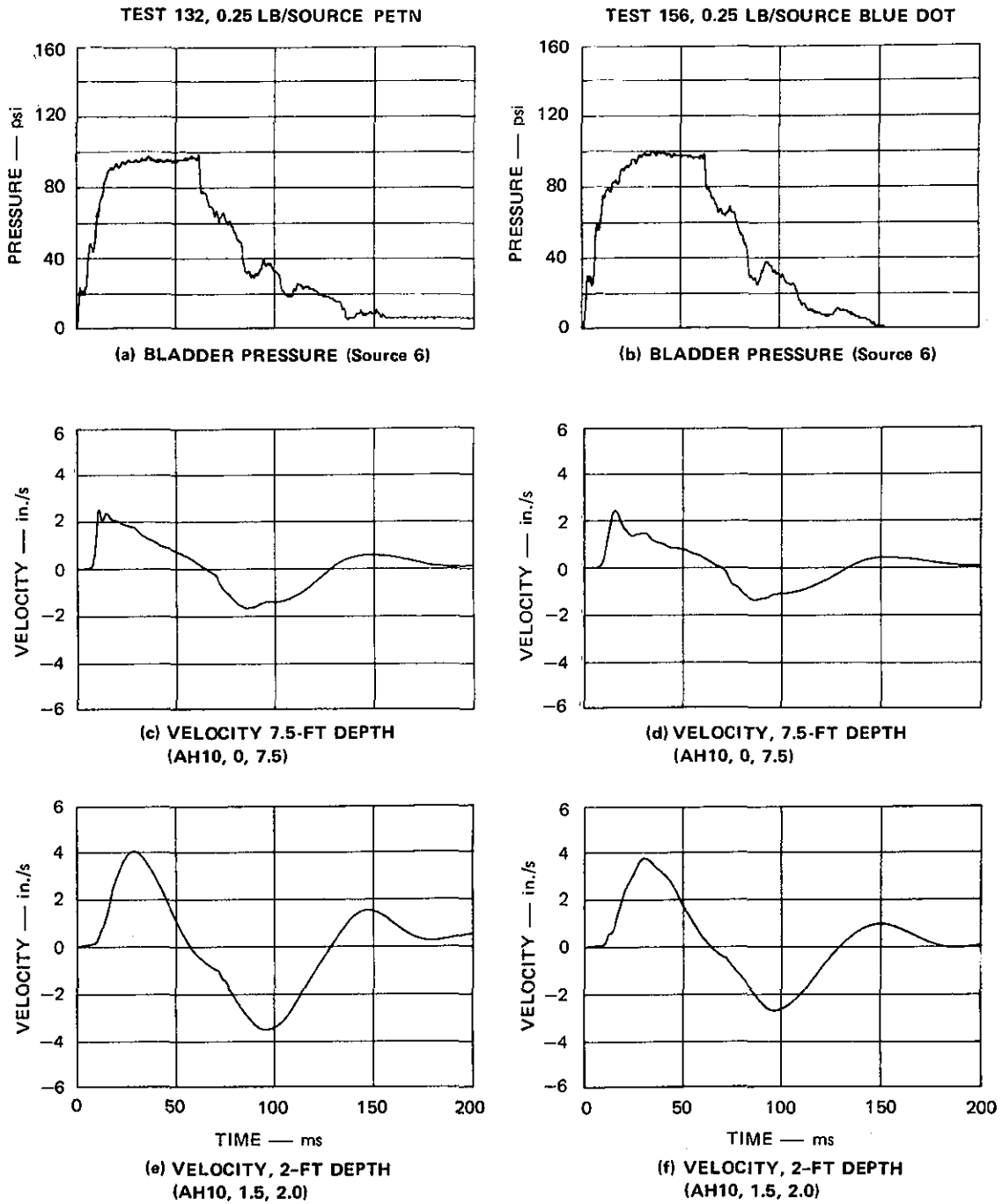
MA-7556-39

FIGURE 31   COMPARISON OF BLADDER PRESSURE AND EARTH MOTION FOR TESTS
WITH EQUAL AMOUNTS OF PETN OR BLUE DOT

Canister Vent Area 0.60 in.^{2}/source

68

BLADDER PRESSURE (SOURCE 6)   SOIL STRESS (10-FT STANDOFF, 2.5-FT DEPTH)

(a)   TEST 156, 0.25 LB/SOURCE BLUE DOT   (b)

(c)   TEST 157, 0.37 LB/SOURCE BLUE DOT   (d)

(e)   TEST 158, 0.62 LB/SOURCE BLUE DOT   (f)
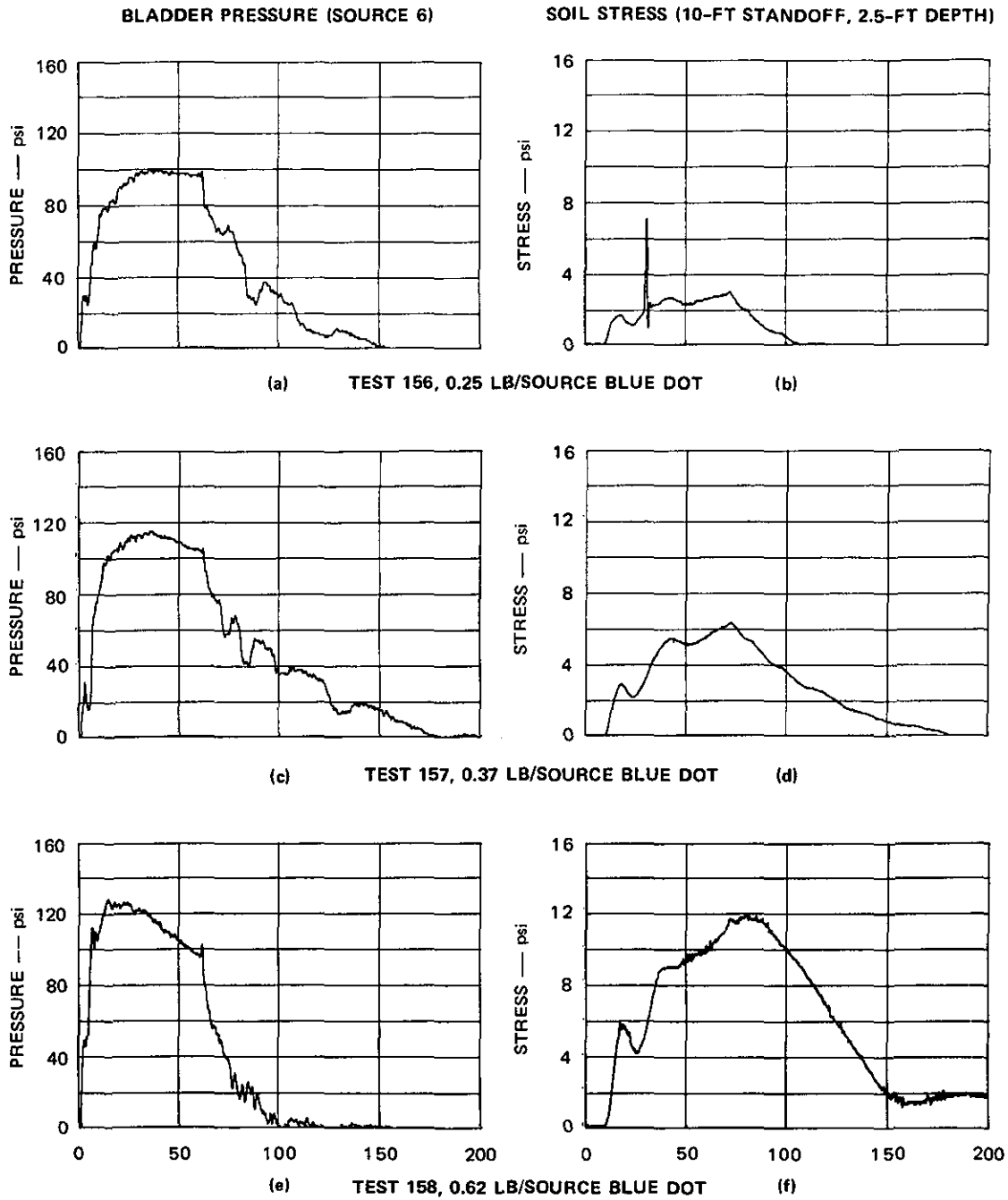
MA-7556-40

FIGURE 32   VARIATION OF BLADDER PRESSURE AND SOIL STRESS WITH CHARGE
SIZE FOR ARRAY TESTS

Canister Vent Area 0.60 in.^{2}/source

Figure 32 shows that the soil stress increases at a rate greater than that with which the charge is increased. For example, comparing the results of Tests 156 and 158 shows that a 3.8-fold increase in soil stress occurs with a 2.5-fold increase in charge. This is caused by the nonlinearity of the soil response close to the sources, as discussed in detail in Section IV.

Figure 33 shows the variation of recorded acceleration with charge size for the three tests. The six records are all from a 10-ft standoff. The three records on the left are for a 7.5-ft depth and the three on the right are for a 2-ft depth. Figures 34 and 35 show the velocity and displacement time histories calculated from the six acceleration records shown in Figure 33.

Figures 33 through 35 also show that earth motion increases at a rate higher than that with which the charge increased. For example, comparison of the displacement at a 10-ft standoff and a 2-ft depth for Tests 156 and 158 shows a 3.5-fold increase in displacement occurs with a 2.5-fold increase in charge. This relationship between earth motion and charge weight is similar to the relationship, discussed above, between soil stress and charge. This result is as expected because both the soil stress and earth motion measurements are for a 10-ft standoff, in an area where the soil should behave elastically (see Section IV.) Therefore, a one-to-one relation should exist between soil stress and earth motion.

Another result learned from these array tests was that the charge of 0.62 lb per source used in Test 158 is an upper limit of charge size before bladder and soil failure occurs with the present source design. During this test, two sources on one end of the array failed because of the soil failure between the top of the bladder and the surface. This failed section of soil moved upward and then the unconfined bladder ruptured. This charge limit could be increased in future line source designs by a deeper placement of the bladder, thereby giving more soil confinement.

70
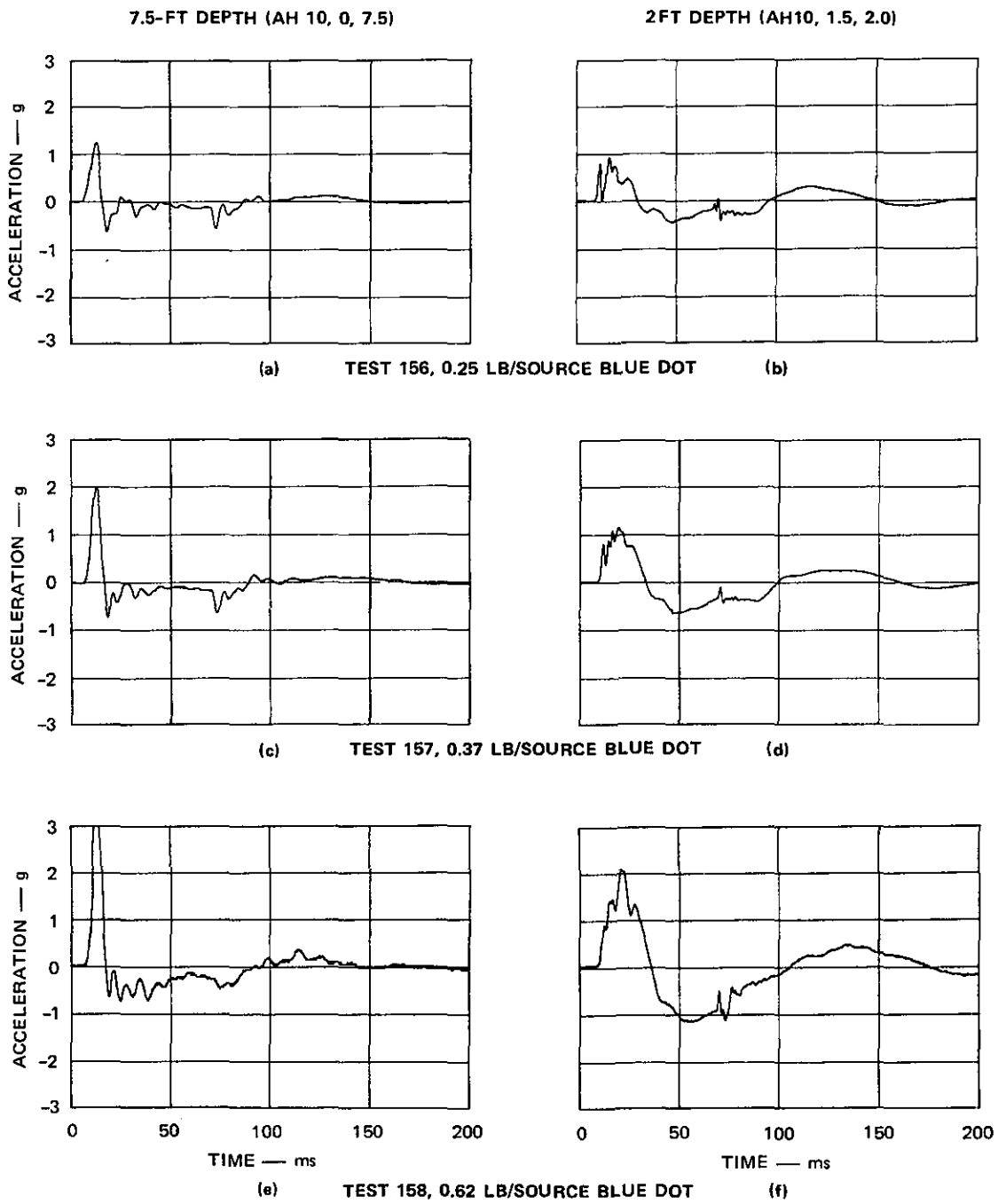
FIGURE 33   VARIATION OF ACCELERATION WITH CHARGE SIZE FOR ARRAY TESTS

10-ft standoff, Canister Vent Area 0.60 in.^{2}/source

71
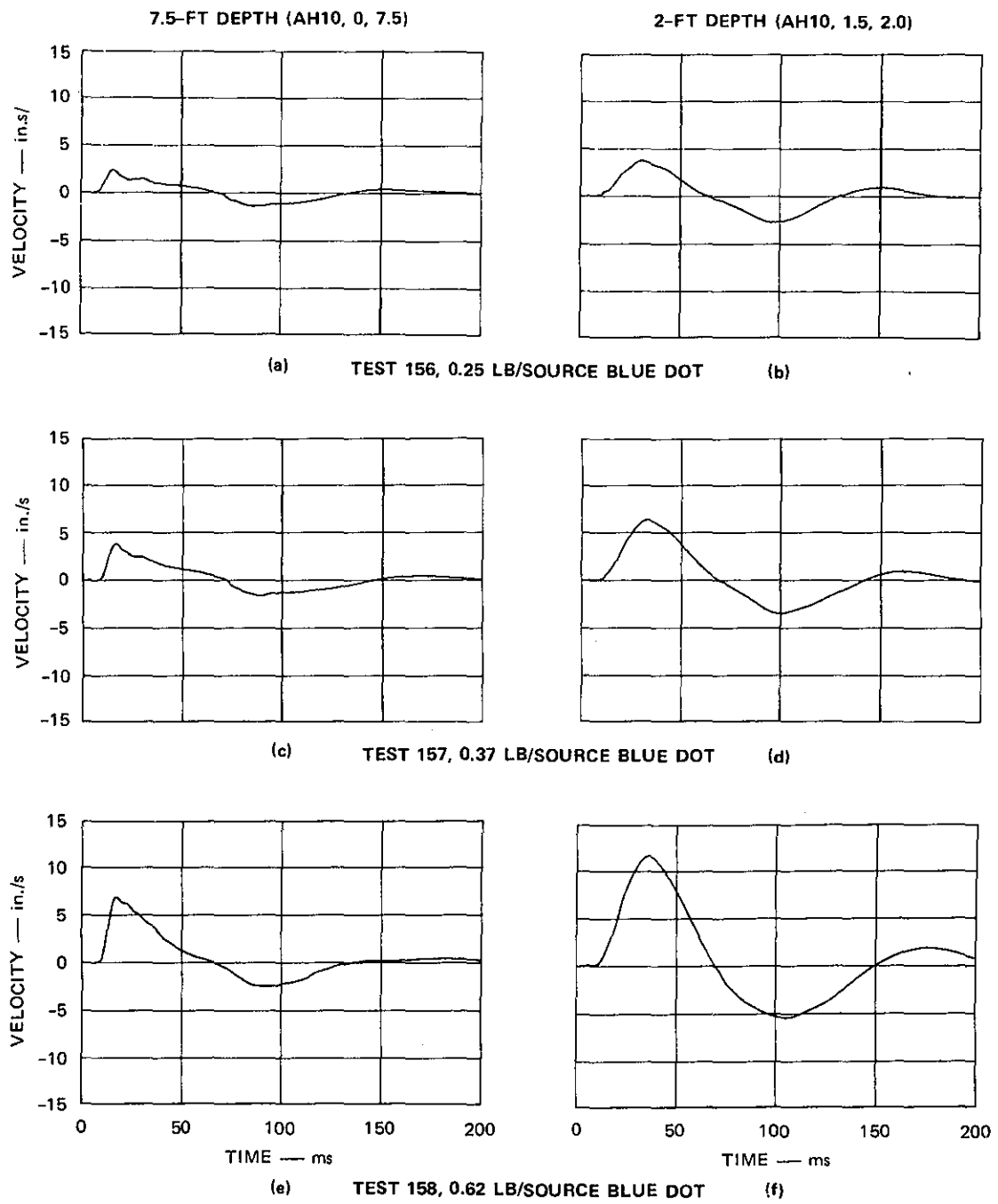
FIGURE 34   VARIATION OF VELOCITY WITH CHARGE SIZE FOR ARRAY TESTS

10-ft Standoff, Canister Vent Area 0.60 in.^{2}/source

7.5-FT DEPTH (AH10, 0, 7.5)   2-FT DEPTH (AH10, 1.5, 2.0)

DISPLACEMENT — in.

0.6
0.4
0.2
0

(a)   TEST 156, 0.25 LB/SOURCE BLUE DOT   (b)

DISPLACEMENT — in.

0.6
0.4
0.2
0

(c)   TEST 157, 0.37 LB/SOURCE BLUE DOT   (d)

DISPLACEMENT — in.

0.6
0.4
0.2
0

0   50   100   150   200
TIME — ms

0   50   100   150   200
TIME — ms

(e)   TEST 152, 0.62 LB/SOURCE BLUE DOT   (f)
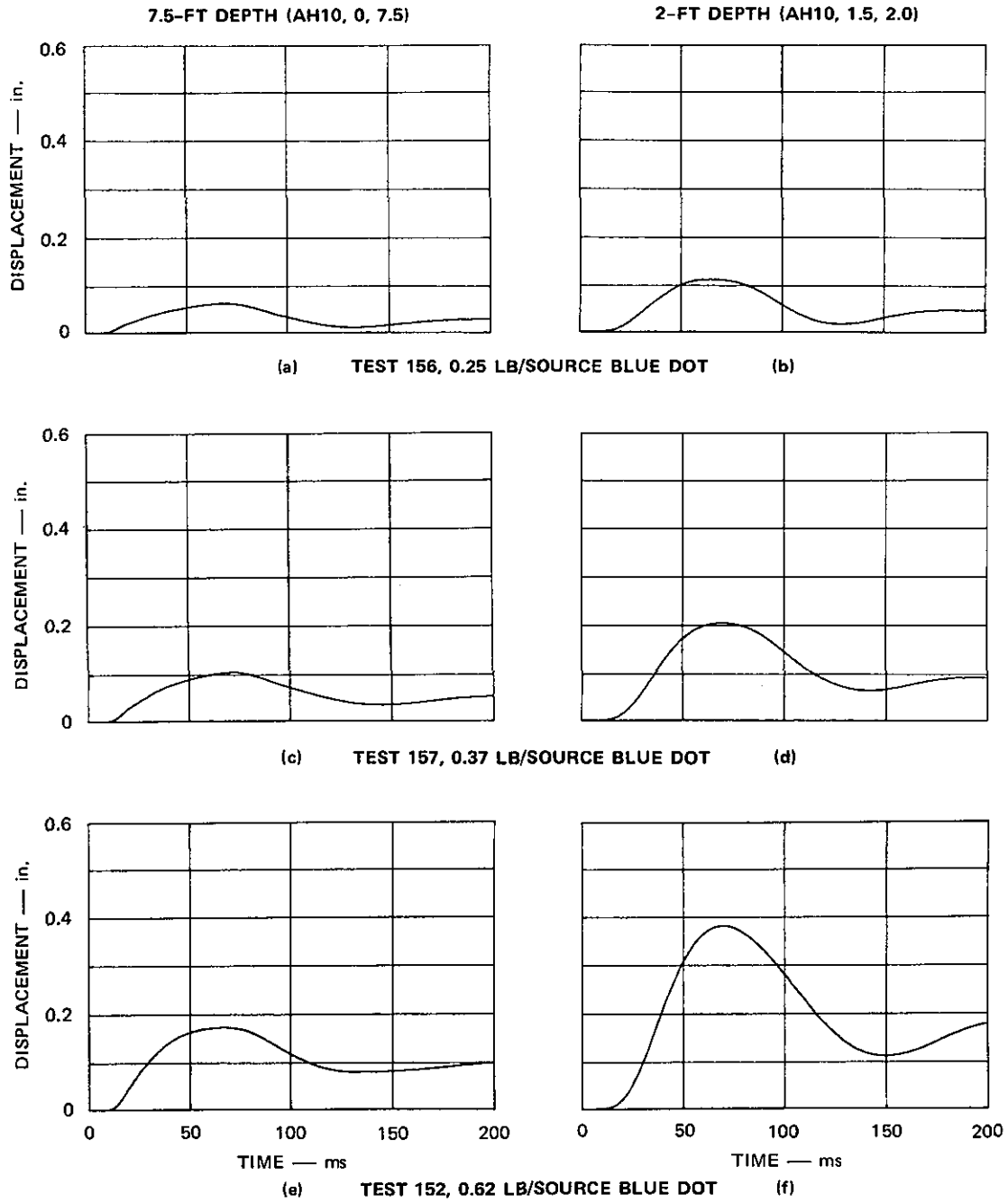
MA-7556-43

FIGURE 35   VARIATION OF DISPLACEMENT WITH CHARGE SIZE FOR ARRAY TEST
10-ft Standoff, Canister Vent Area 0.60 in.²/source

73

F.   Summary of Array Tests

Seven array tests were performed with the 30 x 15 ft array. The following results typify the seven tests:

- The ground motion is uniform along the 12-ft length of the instrumented area (along a line parallel to the array).

- The ground motion attenuates about 30% across the 10-ft width of the instrumented area (along a line perpendicular to the array).

- The ground motion at the mid-depth of the array has a slightly faster rise-time and is slightly lower in amplitude than that near the surface.

- The soil displacement and the soil stress follow the source pressure in shape, a basic characteristic of quasi-static response.

- The primary frequency of the ground motion is in a range from 8 to 15 Hz. (This scales to 3 to 5 Hz for the 80 x 40 ft array.)

A series of array tests with three canister vent areas showed that reducing the vent area decreases amplitude of the soil motion, while having little effect on the frequency. We attribute this decrease in amplitude to heat transfer to the charge canister (a smaller canister vent area causes the detonation products to remain longer in the canister). Frequency was not affected because, although the decrease in vent area did decrease the soil stress rise rate, it did not increase the soil stress rise time (Figure 28), because of the reduced stress. However, the similarity in soil stress and displacement time-histories in period and shape for these three tests (Figure 30) indicates that by proper tailoring of the bladder pressure at high enough levels both period and shape of soil motion can be controlled.

A series of array tests employing three different charge sizes showed that increasing the charge size by a factor of 2.5 results in a 3.5 fold increase in soil displacement (Figure 35). The tests also showed that an upper limit on charge size for a 4-in.-diameter source with a 3-ft-deep soil cover is 0.62 lb/source. However, higher charge limits are possible by locating the source under a deeper soil cover.

74

Table 3 summarizes the test conditions and key peak response values from the seven array tests. Peak bladder pressure ranged from 70 to 125 psi. At a 10-ft standoff and 2-ft depth, peak soil stress ranged from 1 to 12 psi, peak soil acceleration ranged from 0.4 to 2g, peak soil velocity ranged from 0.6 to 12 in./s and peak soil displacement ranged from 0.03 to 0.4 in.

Using the measured soil response from the 30 x 15 ft array and the geometric scaling factors shown in Table 3 (Section VII), soil response can be estimated for an 80 x 40 ft array (the size scaling constant is equal to 80/30 or 2.7 in this case). These estimates are: Peak soil stress ranges from 1 to 12 psi, peak soil acceleration ranges from 0.1 to 0.7g, peak soil velocity ranges from 0.6 to 12 in./s and peak soil displacement ranges from 0.1 to 1.1 in. The charge weight needed to produce these responses ranges is from 3 to 12 lb per source, or 30 to 120 lb total.

Table 2

SUMMARY OF ARRAY TEST RESULTS

Test No.	Charge Weight (lb/source)	Charge Type	Canister Vent Area (in.^{2}/source)	Peak Bladder Pressure (psi)	Peak* Soil Stress (psi)	Peak* Soil Acceleration (g)	Peak* Soil Velocity (in./s)	Peak* Soil Displacement (in.)
127	0.17	PETN	0.30	70	1.1	0.4	1.1	0.04
130	0.25	PETN	0.30	72	3.1	0.7	2.0	0.07
131	0.25	PETN	0.15	55	1.4	0.4	0.6	0.03
132	0.25	PETN	0.60	98	4.0	1.0	4.2	0.13
156	0.25	Blue Dot	0.60	98	3.0	0.9	3.8	0.11
157	0.37	Blue Dot	0.60	114	6.4	1.3	6.3	0.21
158	0.62	Blue Dot	0.60	125	11.8	2.1	11.6	0.38

*
 Measured at 10-ft standoff, 2-ft depth.

VI COMPARISON OF THEORY WITH EXPERIMENTAL RESULTS FOR ARRAY TESTS

In the theory (see Section IV and Appendix E) the array is treated as an elliptical hole in an infinite elastic medium under internal pressure P_e. The internal pressure acting on the ellipse, P_e, is related to the source pressure P_s through a finite element computer calculation, in which the finite length of the array, the interaction of the sources, and the elastic-plastic behavior of the soil are taken into account.

In the array tests (see Section V) the bladder pressure was measured at two of the sources, and the soil stress and soil displacement were measured at a 10-ft standoff from the array. The source pressure P_s acting on the soil is equal to the bladder pressure, minus the component from the rubber bladder's hoop stress, which was measured in a static test to be 20 psi for bladder expansions of 25% to 100%. The soil stress at a 10-ft standoff approximately equals the pressure acting on the ellipse P_e. (In the solution of the elliptical hole given in Appendix E, the stress at a 10-ft-standoff [σ_u at $\rho = 0.6$] is 85% of the stress at the edge of the ellipse [σ_y at $\rho = 1$].) For comparison to theory we use the measured bladder pressure, minus 20 psi, as the measured value of pressure source P_s, and we use the measured soil stress at a 10-ft standoff as the measured pressure acting the elliptical boundary, P_e.

Figure 36 shows the calculated and measured soil displacement at a 10-ft standoff from the array as a function of the source pressure. The calculation was performed for a nominal set of soil property values, $E = 5000$ psi, $\nu = 0.2$, $\sigma_u = 30$ psi and $\phi = 30°$, with an elastic-perfectly plastic Mohr-coulomb yield criterion for the soil. The curve showing the measured relationship was determined by plotting the value of the peak displacement versus the value of the peak source pressure for each of the seven array tests (shown by the solid circles) and fitting a curve through the seven points. Qualitatively, the two curves show the

77
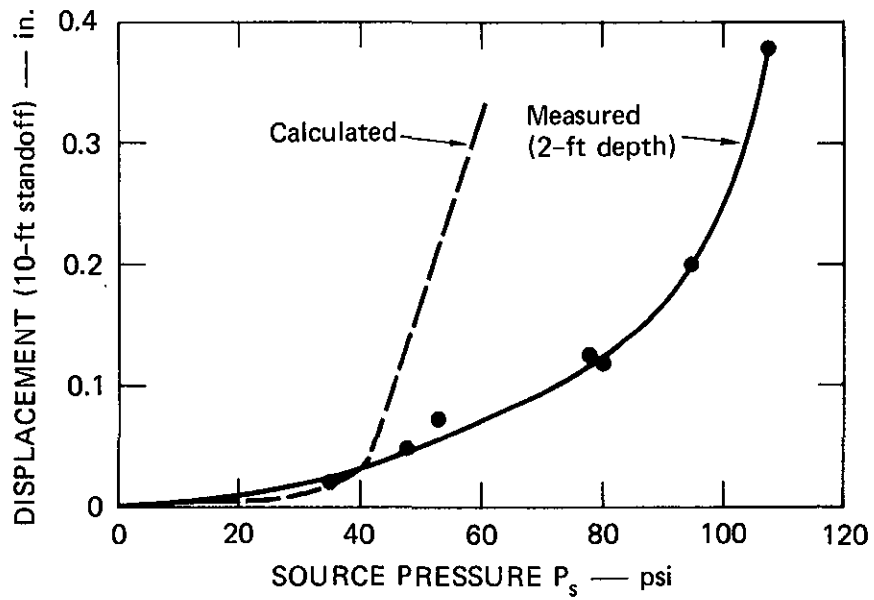
MA-7556-44

FIGURE 36   CALCULATED AND MEASURED RELATION BETWEEN SOURCE PRESSURE
AND SOIL DISPLACEMENT

same characteristic: The soil displacement increases slowly as source pressure is increased until a critical source pressure is reached; then the soil displacement increases at a much faster rate. The calculations indicated that this critical source pressure is reached when the plastic radii around each source in the array approach each other. At this point the array acts like a slit in the earth rather than as a series of individual single sources, and therefore an increase in source pressure contributes more directly to increasing the soil displacement rather than primarily increasing the elastic-plastic boundary radius around each source.

Quantitatively the two curves are different, primarily because of the difference in the value of the critical source pressure. We believe this is due to the simplified soil model and soil properties used in the calculation. Refinement of the soil model is planned for future calculations.

Figure 37 shows the calculated and measured soil displacement at a 10-ft standoff from the array as a function of the boundary pressure. The calculation was performed with the same nominal set of soil property values given above, by using the elastic solution for a pressurized elliptical hole given in Appendix E. The curve showing the measured relationship was determined by plotting the peak values from the seven array tests and fitting a line through the seven points.

The calculated relationship is a straight line because the calculation is linear elastic. The measured data also fall along a straight line, indicating that outside the elliptical boundary surrounding the array the soil is indeed behaving linearly. The difference in the slope of the two lines probably results because of inaccurate knowledge of the true in-situ elastic soil properties and because the simplified plane strain calculation neglects the effect of the free surface and the finite depth of the array.
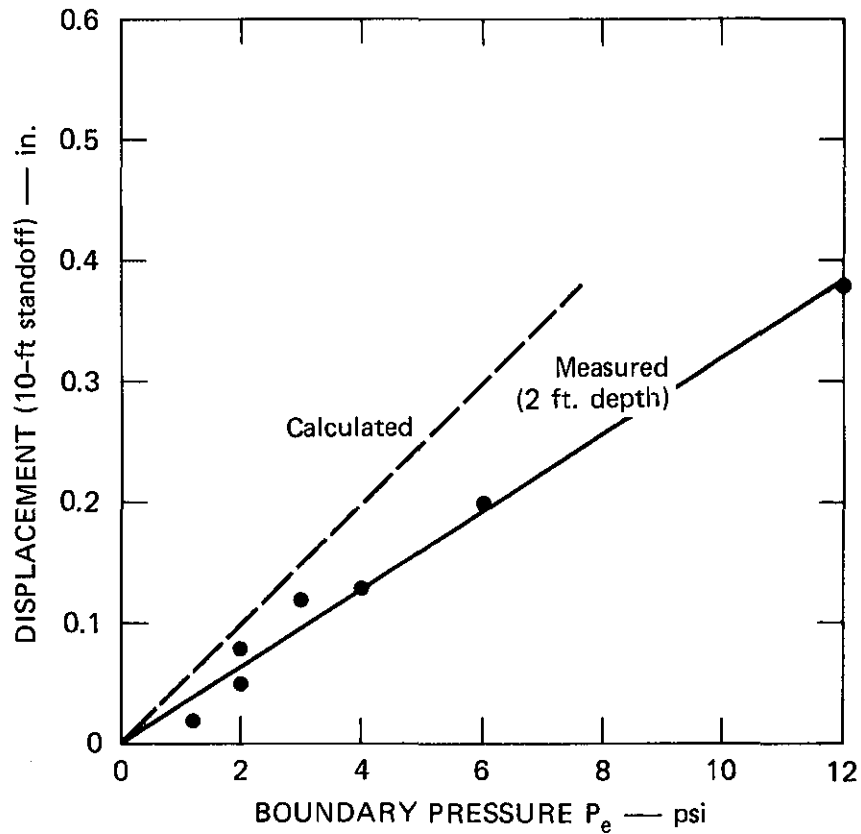
FIGURE 37   CALCULATED AND MEASURED RELATION BETWEEN PRESSURE ON
THE ELLIPTICAL BOUNDARY AND PEAK SOIL DISPLACEMENT

In summary, the quasi-static theory reproduces the important
features governing the response of the soil around the array. Qualitatively
the theory and the measured response are in good agreement. The theory
and the measurements both show that a critical source pressure exists above
which the sources should be operated to achieve the full benefit of the
array geometry.

Page Intentionally Left Blank

VII RESPONSE SPECTRA ANALYSIS

A convenient method for comparing ground motion from the line source array and from an actual earthquake is by using response spectra. The response spectrum is a plot of the maximum system response versus system frequency of a single-degree-of-freedom, dynamic system founded on the ground. The response spectra shown in this section are normalized to a peak ground acceleration of 1g and give data for "maximum pseudo-relative velocity," "maximum relative displacement," and "maximum pseudo-absolute acceleration."

Figure 38 compares three response spectra: the response spectrum for the estimated ground motion from a single detonation of an 80 x 40 ft array, the response spectrum for the estimated ground motion from three detonations spaced 1 s apart of an 80 x 40 ft array, and an envelope response spectrum statistically obtained by Newmark, Blume, and Kapur for several earthquakes.[2]

The ground motion for the 80 x 40 ft array is estimated by using the acceleration recorded at the center of the structural test area in a 30 x 15 ft array test (specifically, from accelerometer AH10, 1.5, 2.0 in Test 158) and applying geometric scaling laws with a scale factor of 3. Table 3 shows the general relationship using geometric scaling for the input and response variables in the similar structures. With geometric scaling all materials remain the same, and all dimensions in the system are scaled by a factor S approximately equal to 3 in this case. The two input variables that cannot be readily scaled are the acceleration of gravity and the strain rate constants of the various materials. However, if response is primarily governed by inertia and elastic forces and not by gravity forces, and if strain rate effects are not large, geometric scaling gives reasonable estimates for response.
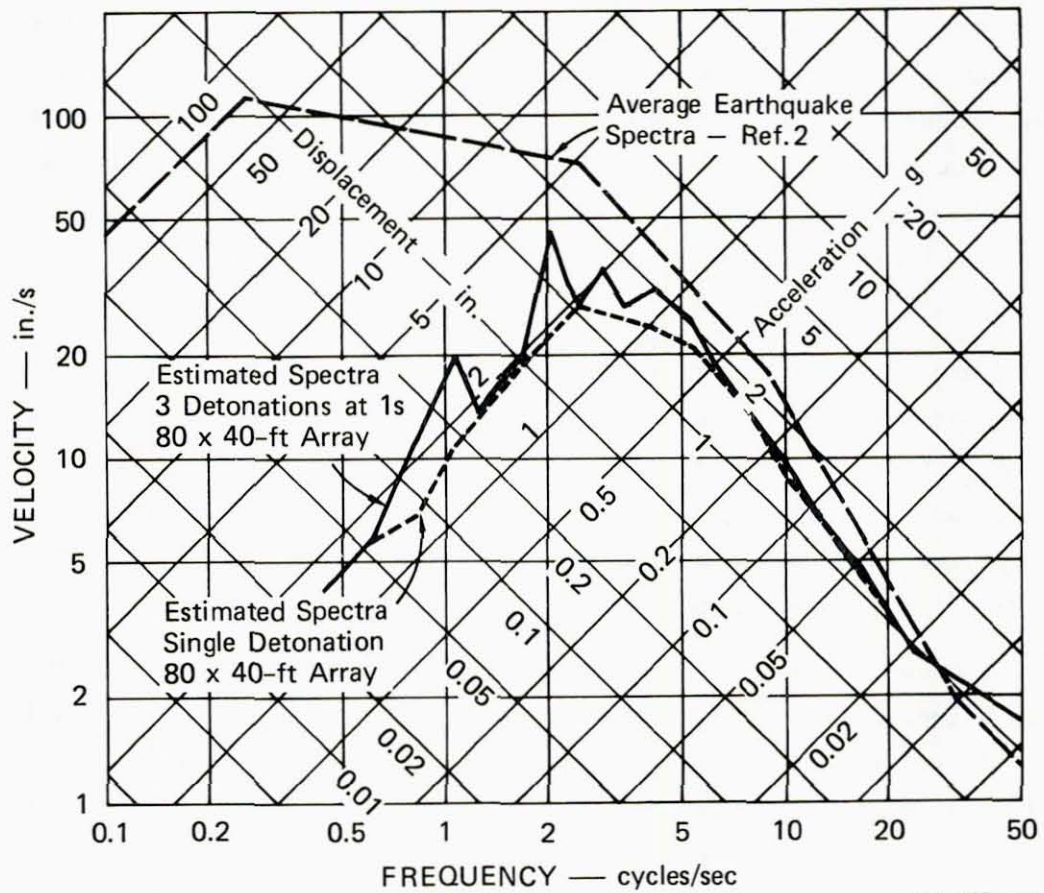
FIGURE 38   COMPARISON OF RESPONSE SPECTRA FOR ESTIMATED GROUND MOTION
FROM 80 x 40-FT ARRAY TO AVERAGE EARTHQUAKE SPECTRA

84

Table 3

GEOMETRIC SCALING OF VARIABLES

Input Variables	Small	Large
Length	L	LS
Elastic modulus	E	E
Density	ρ	ρ
Mass	m	mS^3
Energy	Q	QS^3
Gravity	g	g/S
Strain rate constant	α	αS

Response Variables		
Displacement	d	dS
Velocity	v	v
Acceleration	a	a/S
Pressure	P	P
Stress	σ	σ
Strain	ε	ε
Strain rate	$\dot{\varepsilon}$	$\dot{\varepsilon}/S$
Time	t	tS

S = 2.7

Comparison of both of these response spectra for the 80 x 40 ft array with the Newmark, Blume, and Kapur spectrum shows there is a good agreement in shape at frequencies higher than 2 Hz. At freqencies lower than 2 Hz the array spectra falls off in amplitude from the Newmark, Blume, and Kapur spectrum (Figure 38). (A comparison of amplitude should not be made, however, because both spectra are normalized to a peak ground acceleration of 1g. Experience with the 30 x 15 ft array and scaling laws discussed in Section III indicate that the 80 x 40 ft array can produce ground acceleration that exceeds 0.5g. This amplitude covers the range of expected accelerations from strong motion earthquakes.)

A reason for this fall off below 2 Hz can be found by examining the displacement response axis. An 80 x 40 ft array operating at a 1g level can produce a peak ground displacement of about 2 in. Thus, it is understandable that the normalized spectra are limited to displacements on the order of 2 to 4 in.

In short, the 80 x 40 ft array spectra are a good match to Newmark, Blume, and Kapur's spectrum for frequencies higher than 2 Hz. We believe that by adjustment the timing between detonations an even better agreement can be obtained. For structures for which frequencies lower than 2 Hz are important, one or both of two things can be done: The structure can be tested at some smaller scale, for which the structural frequency of interest is raised by the scale factor; or a larger size array can be built. As stated in the introduction, arrays three to four times the size of the 80 x 40 ft. array are within conventional construction capabilities. Their cost would be higher and would have to be weighed against the need for full-scale testing. (A discussion of cost is given in Section I.) An estimate for an array twice the size of the 80 x 40 ft array predicts it can produce peak ground displacements of about 3 in. at an acceleration level of 0.3g. When this ground motion is normalized to 1g, the displacement response spectrum rises to 10 in. Thus, the normalized spectrum from a 160 x 80 ft array would have a limit at the 10 to 20 in. displacement level.

VIII CONCLUSIONS AND FUTURE WORK

The results of the past 2 years' work demonstrate that the contained explosion line source array is a feasible technique for testing in-situ structures at strong earthquake levels. Tests at 1/3 scale demonstrate that reasonable amplitudes and frequencies can be coupled into the earth with a minimum of explosive and with no surface eruptions. Theoretical extrapolation to a 80 ft wide by 40 ft deep array shows that 120 lb of explosive will give a peak velocity of about 12 in./s, a peak displacement of about 1 in., and a fundamental frequency of 3 Hz. The tests also show that repeatable results can be obtained with reuse of the same line sources.

The test of the full-scale line source showed that a 12-in.-diameter by 37-ft-long line source can be built, handled, and placed in the ground. Although the charge canister failed, we do not believe that any significant changes are necessary in the line source design itself. The major changes necessary are in the charge grain size and configuration. Several methods are available to correct the problem of charge pressure control, and they can be persued by simple laboratory testing.

In the new 2-year program proposed to begin in early 1980, we plan to build and test the larger 80 x 40 ft array; it will consist of 8 to 10 sources, with each source having a 3-pulse-per-test capability. During the first year, the array will be built and tested in the single-pulse mode. In the second year, the 3-pules-per-test capability will be added. A 30 x 30 ft test area will be available for structural testing by SRI, and by other researchers as time and space allow.

These tests will provide the technological basis for the long-range objective of designing groups of arrays, of this size and larger as needed, that can simulate motions lasting 5 to 10 s. For example, a group of three arrays of the size described above, with each array

adjusted to produce a different pulse duration, could provide a sequence of 18 acceleration pulses (9 firings) and hence a simulated motion lasting 5 s and having a frequency content ranging from 2 to 10 Hz. We envision that such arrays would be built after completion of the above program as a cooperative effort among several universities, or by industrial concerns for use in applied research and immediate application to earthquake resistance research and certification.

REFERENCES

1. G. R. Abrahamson, H. E. Lindberg, and J. R. Bruce, "Simulation of
    Strong Earthquake Motion with Explosive Line Source Arrays,"
    SRI Final Report for NSF (October 1977).

2. N. Newmark, J. Blume, and K. Kapur, "Seismic Design Spectra for
    Nuclear Power Plants," ASCE J. Power Division (November 1973).

Appendix A

CLOSED CHAMBER TESTS OF EXPLOSIVE AND PROPELLANT CHARGES

A series of closed chamber, constant volume tests were performed for both explosive and propellant charges. The objectives of these tests were to (1) examine the relation between charge canister vent area and energy loss to the canister wall through heat transfer, and (2) examine the feasibility of using propellant as the charge in the line source. While the volume of the line source varies as a function of time, these tests were performed in a closed chamber of constant volume to facilitate data interpretation.

The closed chamber consisted of an aluminum tube 8 in. I.D. and 30 in. long. (The 8-in.-diameter represents a diameter of the 1/3-scale line source when expanded to twice its original size.) The tube was sealed with a plate at the bottom and with a removable lid at the top. Pressure was measured inside the closed volume using two redundant PCB 102M50 pressure gages mounted in the lid of the chamber.

A 24-in.-long section of the 1/3-scale line source charge canister was used in the tests. This canister was a 1015 carbon steel tube with a 2.375-in.-O.D. and a 0.438-in.-thick wall.[*] The tube was threaded at both ends and was sealed using two pipe caps. Two 0.375-in.-diameter holes were drilled and tapped in the side of the charge tube to allow placement of one or two vent plugs, each containing a 0.188-in.-diameter vent. (When only one vent plug was used, the other 0.375-in.-diameter hole was sealed with a solid plug.)

_____

[*] This size charge canister was used in the early single-source tests described in Reference 1. In the single-source and array tests described in this report, a slightly larger, 2.5-in.-O.D. canister was used.

In the tests, charges of either explosive or propellant were initiated within the canister. The high pressure explosion products then flow out of the canister through the vent plugs pressurizing the closed chamber.

Tests to Determine the Relation Between Canister Vent Area and Energy Loss

In the array tests it was observed that peak bladder pressure, and thus the ground response, decrease when the canister vent area is reduced. We believe this lower pressure can be attributed to energy loss through heat transfer to the inner walls of the canister. Within the canister, the temperature of the explosion products is above 3000 K. At this temperature a rough estimate shows that a 50% loss of energy to the inner canister wall can occur in less than 100 ms. On the other hand, outside the canister the expanded explosion products are considerably cooler and the rate of heat transfer is considerably less than that inside the canister. Hence, as the canister vent area is reduced and the explosion products remain within the canister a relatively longer time, the energy loss is increased, directly reducing the bladder pressure.

Two tests (Tests 133 and 134) were conducted to examine the relation between the charge canister vent area and the peak chamber pressure. (The peak pressure in the sealed, constant volume chamber is linearly related to the temperature and thus is directly related to the energy loss.) In both tests a 2-ft-length of 150 gr/ft[*] Primacord, containing 0.042 lb of PETN, was initiated within the charge canister. In Test 133 there were two 0.188-in.-diameter vents in the canister, while in Test 132 there was only one 0.188-in.-diameter vent. This charge size and these vent areas are consistent on a per unit length basis with the range of charge sizes and vent areas used in the seven 1/3-scale array tests.

---

[*] 1 gr equals 1/7000 of a pound.

Figure A-1 shows the chamber pressure for the two tests. The peak pressure using two vents was 55 psi [Test 133, Figure A-1(a)], whereas the peak pressure using one vent was 42 psi [Test 134, Figure A-1(b)].

These results show that a 50% decrease in canister vent area leads to a 25% decrease in chamber pressure. This is the same result that was seen in the field array tests. For example, in Test 132, with the largest vent area used in the array tests, the peak bladder pressure was 98 psi; in Test 130, with one-half the vent area but the same charge amount as Test 132, the peak bladder pressure was 72 psi, a 27% decrease; and in Test 131, with one-quarter the vent area and again the same charge amount as Test 132, the peak bladder pressure was 55 psi, and additional 25% decrease.

By considering the results from the closed chamber tests, it can be stated that the decrease in pressure associated with reduction of vent area seen both in the closed chamber and in the array tests can be accounted for in energy loss to the canister through heat transfer. This statement was not possible by considering only the array tests since the volume of the bladder at the time the peak pressure was reached directly effects the pressure. (The bladder volume is a function of the past pressure-time history and the soil compressibility and it is therefore not precisely known.)

In summary, the results of these two closed chamber tests help in understanding the reduced ground motion associated with reducing the canister vent area; they suggest that if the vent area is reduced, the charge amount should be increased to account for the expected increased energy loss.

Tests Using Propellant Charges

In an explosive the energy releasing reaction propagates at a rate faster than the acoustic wave velocity of the explosive material, thereby producing a detonation-supported shock front. The pressure at this shock front (detonation pressure) is very high (50 to 250 kbar). In a propellant the energy releasing reaction propagates at a rate
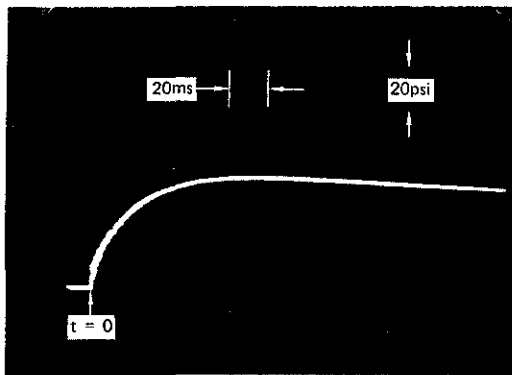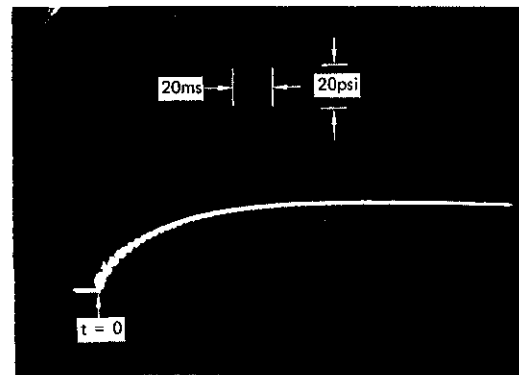
(a) Test 133, 19 gm PETN, 2 Vents   (b) Test 134, 19 gm PETN, 1 Vent

MP–7556–47

FIGURE A-1   CHAMBER PRESSURE FOR EXPLOSIVE TESTS

slower than the acoustic wave velocity of the propellant material. For this reason, the burn rate is sensitive to the pressure created behind the front and to the amount of confinement. The pressure at the reaction front is not constant as a function of time, but is considerably less than the detonation pressure of the explosive.

For this application, propellants have the advantage over explosives because their lower reaction pressure allows the propellant to be contained within a smaller canister than that needed to contain an equal amount of explosive. These smaller canisters are particularly desirable not only because of cost savings in steel, but also because their smaller size will allow placement of three canisters within each source--a necessary feature if multiple pulses are to be achieved within an individual source.

One disadvantage of propellants compared with explosives is that their burn rate is sensitive to pressure. Therefore, to achieve repeatability, it is desirable to burn all the propellant at a rate that is fast relative to the rate in which gas is vented from the charge canister. In this way the controlled venting process controls the bladder pressure. Also, as we learned in the full-scale source test (Section III), if the propellant burns too fast, the pressure at the reaction front will become very large, which can lead to failure of the canister.

In the closed chamber tests we directed our attention to creating a burn rate that was fast relative to the rate in which gas is vented from the canister. This was achieved by placing the propellant in a 0.75-in.-diameter paper tube and running a 2-ft-long strand of 18 g/ft Primacord through the center of the tube. The paper tube was 3.5-in. long for an 0.040-lb charge of propellant. (The 2-ft-long strand of Primacord contains about 0.004 lb of PETN, about 10% of the mass of the propellant tested.) The Primacord was detonated first and it in turn ignited the propellant. Because the propellant is ignited along a line though its center, so that it need only burn from inside to outside, and because the Primacord, which detonates at 22 ft/ms,

A-5

produces 10% of the total pressure in the first 0.1 ms, the burn rate is fast compared to the vent time, which is 10's of milliseconds.

Figure A-2 shows the chamber pressure from two tests (Tests 145 and 146) in the initial series of propellant tests. These two tests are direct repeats of Tests 133 and 134, respectively (Figure A-1), except that instead of 0.042 lb of PETN the charge consisted of 0.040 lb of Blue Dot propellant plus the 0.004 lb of PETN used to initiate the propellant. Blue Dot and PETN both release an equal amount of energy, about 1200 cal/gm; therefore, equal amounts of each should create approximately equal chamber pressures. Comparison of Test 145 [Figure A-2(a)] with Test 133 [Figure A-1(a)], both having two canister vents, showed that the propellant gave more than twice the peak pressure and a much faster rise time. Comparison of Test 146 [Figure A-2(b)] with Test 134 [Figure A-1(b)], both having one canister vent, showed very similar records for the first 140 ms. At 140 ms Test 145 with propellant shows a sharp rise to move than twice the chamber pressure.

Further study indicated that the explosive and the propellant tests differed because, unlike PETN, the Blue Dot is not oxygen balanced. The combustion products from Blue Dot contain, in part, 37% carbon monoxide and 8% hydrogen. In the closed chamber, additional oxygen exists due to the air present in the chamber. Therefore, once the products vent from the charge canister into the closed chamber, they are subject to a secondary combustion of the carbon monoxide and hydrogen if the temperature and pressure are high enough for ignition.

This explanation helps in understanding the difference between the two sets of tests shown in Figures A-1 and A-2. In the propellant test with two vents (Test 145) the combustion products are ignited in the first few milliseconds, producing the initial differences in the records. In the propellant test with one vent (Test 146) the combustion products do not ignite until 140 ms after the primary ignition, producing the late time differences in the records.
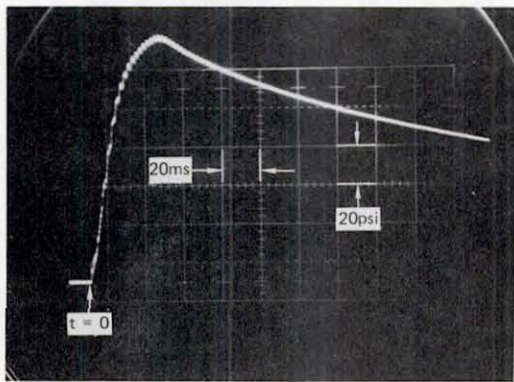
(a) Test 145, 18 gm Blue Dot, 2 Vents   (b) Test 146, 18 gm Blue Dot, 1 Vent
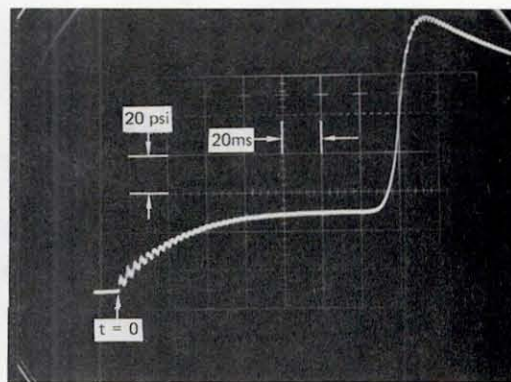
MP-7556-48

FIGURE A-2 CHAMBER PRESSURE FOR INITIAL PROPELLANT TESTS

This second combustion of the primary combustion products is undesirable because it occurs outside the charge canister and therefore its rise time is not controlled by the controlled venting process. For this reason, the second combustion was eliminated by removing most of the oxygen from the closed volume before the test. This was done by pressurizing the closed chamber using nitrogen to a pressure of 15 psig (30 psia) and then venting it to the atmosphere. This process was repeated three times. In theory, each time the process is repeated, the amount of oxygen in the system is reduced 50%. (This is true because pure nitrogen in an amount equal to the original air in the system is being added, the system is assumed to mix, and then half the mixture is removed by venting to the atmosphere.) Thus, after the process has been repeated three times, the oxygen has been reduced from the 20% found in pure air to about 2.5%, a small percentage.

Figure A-3 shows the chamber pressure for two propellant tests (Tests 145 and 149) that were identical except for chamber atmosphere. Test 145 had an air atmosphere and Test 149 had a nitrogen atmosphere. The large effect of atmosphere can be seen by comparing the records.

Figure A-4 compares the chamber pressure for Test 133, performed using 0.042 lb of PETN in an air atmosphere, with that for Test 149, performed using 0.040 lb of Blue Dot and a nitrogen atmosphere. The two records are in very good agreement. This indicates that the propellant burned rapidly compared to the time of venting, that all the propellant was involved in the reaction, and that the secondary combustion of the carbon monoxide and hydrogen products did not occur.

To verify and demonstrate the advantage of propellant (which allows use of a smaller canister than is possible with an equal size charge of explosive), we replaced the 2.375-in.-O.D. and 1.5-in.-I.D. canister used in the previous tests with a 2-ft-length of a 1.31-in.-O.D. and 0.81-in.-I.D. canister. This canister is small enough so that we can place three inside the 4-in.-diameter line source. Early tests with the 2.375-in.-O.D. charge canister had shown that the 0.042-lb charge used in the previous tests was about the limit using PETN before the
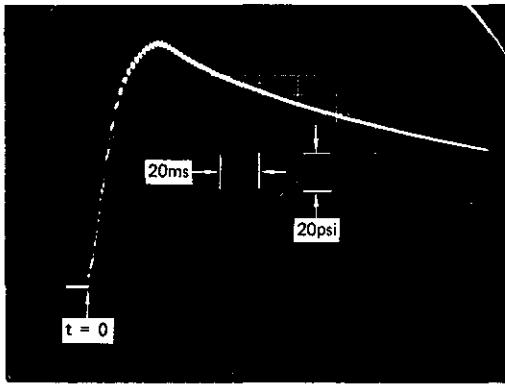
(a) Test 145, Air Atmosphere   (b) Test 147, Nitrogen Atmosphere
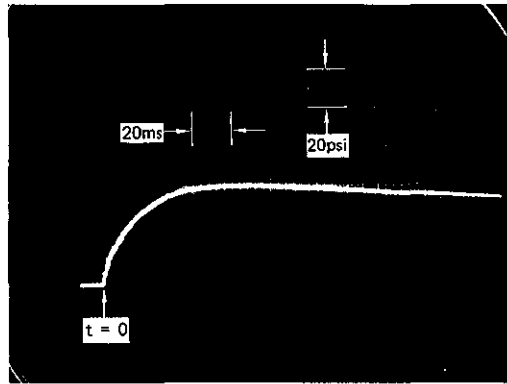
MP-7556-49

FIGURE A-3   EFFECT OF CHAMBER ATMOSPHERE ON CHAMBER PRESSURE FOR
               PROPELLANT TESTS

Both tests with 18 gm Blue Dot and 2 vents
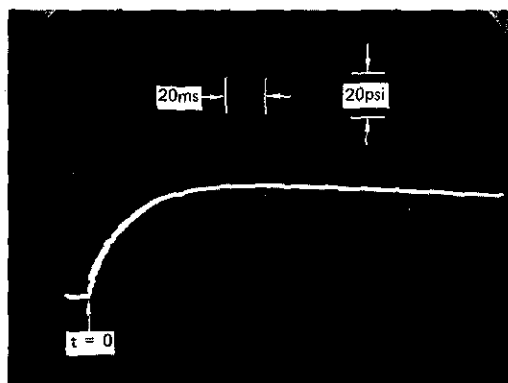
(a) Test 133, 19 gm PETN, 2 Vents,
    Air Atmosphere
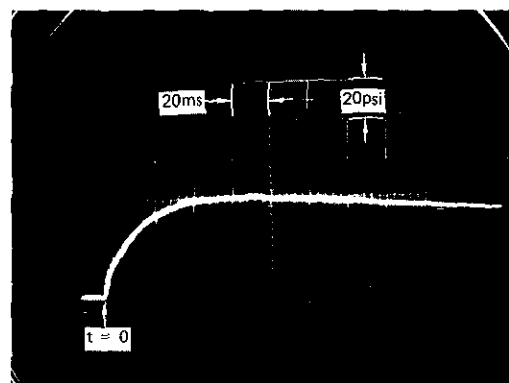
(b) Test 149, 18 gm Blue Dot, 2 Vents,
    Nitrogen Atmosphere

MP-7556-50

FIGURE A-4   COMPARISON OF CHAMBER PRESSURE FOR EXPLOSIVE VERSUS
    PROPELLANT TESTS

canister would rupture. Test 152 was conducted in the smaller, 1.31-in.-O.D. canister using 0.080 lb of Blue Dot with a nitrogen atmosphere. No damage to the canister was observed. Figure A-5 shows the chamber pressure for Test 152. The peak pressure was 115 psi, as expected, twice that for the test with 0.042 lb of PETN [Figure A-1(a)]. (Note that the vertical scale for Figure A-5 is twice that of previous figures.) Thus, in a canister with less than one-third the volume of the original canister, we contained almost twice the amount of charge possible in the original canister. (Both canisters have similar radius-to-thickness ratios.)

We can use the above information to estimate the charge that could be used in both the 1/3-scale and full-scale line source canisters. All three canisters have similar radius-to-thickness ratios and, therefore, similar strengths. The 1/3-scale line source canister has about 25 times the volume of the 1.31-in.-O.D. canister; therefore, it should contain 0.08 lb times 25, or 2 lb of propellant. The full-scale line source canister has 200 times the volume of the 1.31-in.-O.D. canister; therefore, it should contain 0.8 lb times 200, or 16 lb of propellant. However, the result of the full-scale test showed that in order to use these scaled values of charge amount, because the burn rate of the propellant does not scale, we must either use a slower burning propellant or distribute the propellant more uniformly within the canister. (In the tests described here the propellant was concentrated in the center of the canister to allow greater confinement and thus a faster burn rate.)

In summary, propellants provide a repeatable and practical method of pressurizing the bladder. Propellants allow the use of much smaller canisters together with the use of larger charge amounts that would be possible with explosives.

---

* The exact dimensions of these canisters are given in Section II.

A-11
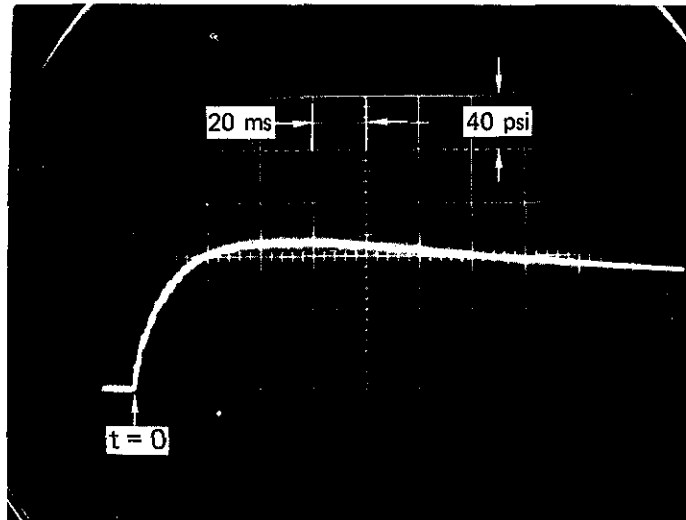
MP-7556-51

FIGURE A-5 CHAMBER PRESSURE FOR PROPELLANT TEST WITH
1.31-INCH-O.D. CANISTER AND 36 gm BLUE DOT

Test 152, 2 vents (0.095-in.-dia)

Appendix B

SOIL PROPERTY TESTS

At the start of the current program, we selected a test site and
performed a soil exploration. Five 21-ft-deep holes were bored with
an auger. A 3-in.-diameter, 36-in.-long Shelby Tube was used to obtain
samples at depths of 3 to 6 ft, 10 to 13 ft, and 18 to 21 ft. The
sampling procedure was to first bore the hole to the given depth, drive
the Shelby Tube into the ground to take a sample, advance the hole with
the auger to the next given sample depth, and so on.

Examination of the soil samples and of the soil that rose on the
auger indicated the upper 21 ft of soil to be a fairly uniform deposit
of dark grey, stiff clay containing some caliche. A few randomly
oriented lenses of sand or silt 1 to 6 inches thick were found through-
out the 21-ft-depth. These lenses were particularly concentrated
between the 10-ft and 12-ft depth. The water table was found at the
11-ft depth.

Terra Tek, Inc., of San Jose, California, characterized the soil
by performing the following laboratory tests on the soil samples: five
unconfined compression tests; three consolidation tests; and a set of
three consolidated, undrained triaxial tests. The test results are
described below.

Unconfined Compression Tests

Five unconfined compression tests were performed to measure the
unconfined strength of the soil. Figure B-1 through B-5 show the
results from these tests. Figure B-6 shows a composite plot of vertical
stress versus vertical strain for the five tests. The unconfined
compressive strength averaged 50 psi at a depth of 3 ft, 25 psi at a
depth of 10 ft, and 35 psi at a depth of 18 ft.

B-1
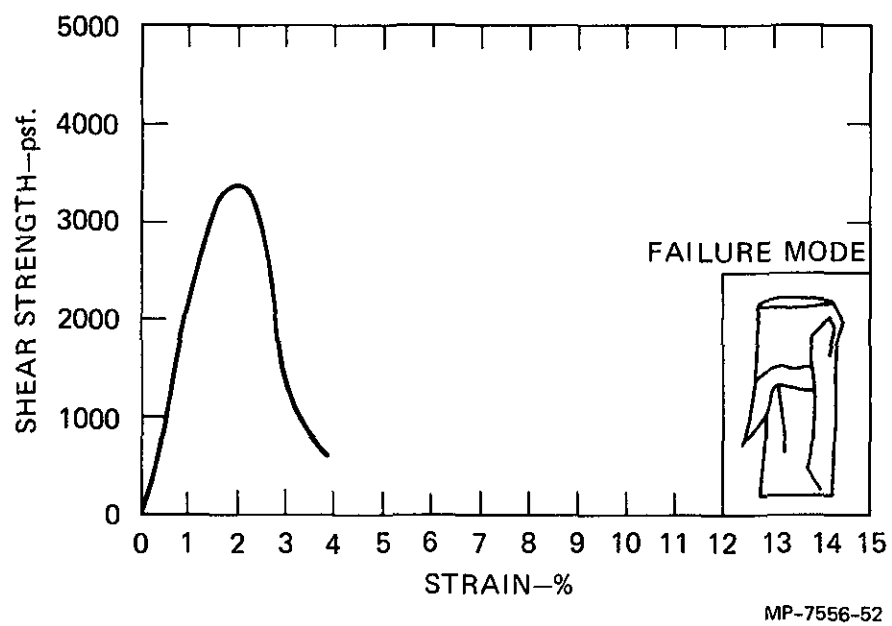
FIGURE B-1   UNCONFINED COMPRESSION TEST ON SAMPLE 1 (3-ft depth)

MP-7556-52
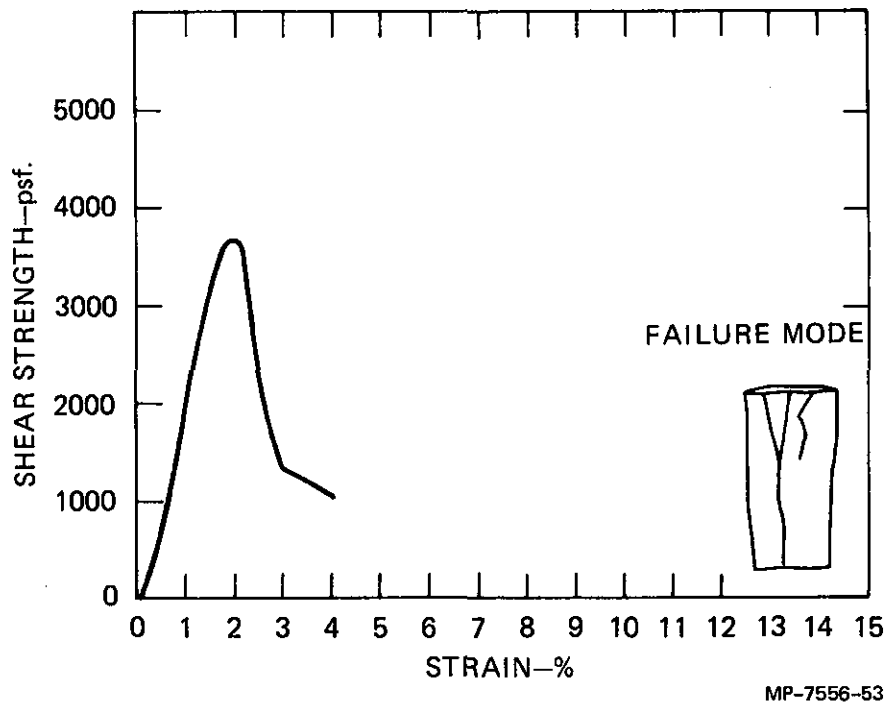
FIGURE B-2 UNCONFINED COMPRESSION TEST DATA ON SAMPLE 2 (3-ft depth)
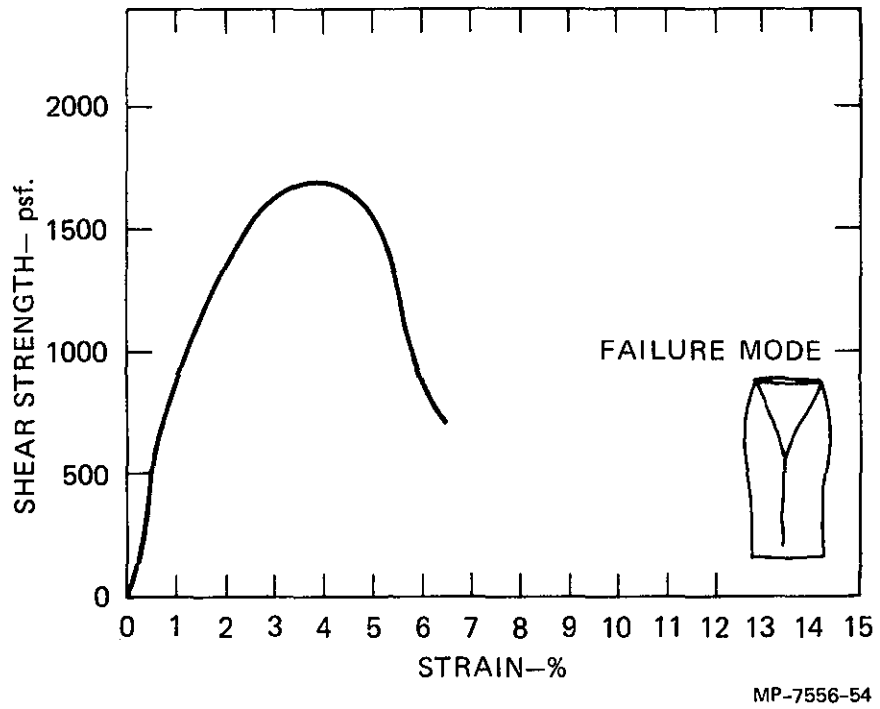
FIGURE B-3 UNCONFINED COMPRESSION TEST ON SAMPLE 3 (10-ft depth)

MP-7556-54
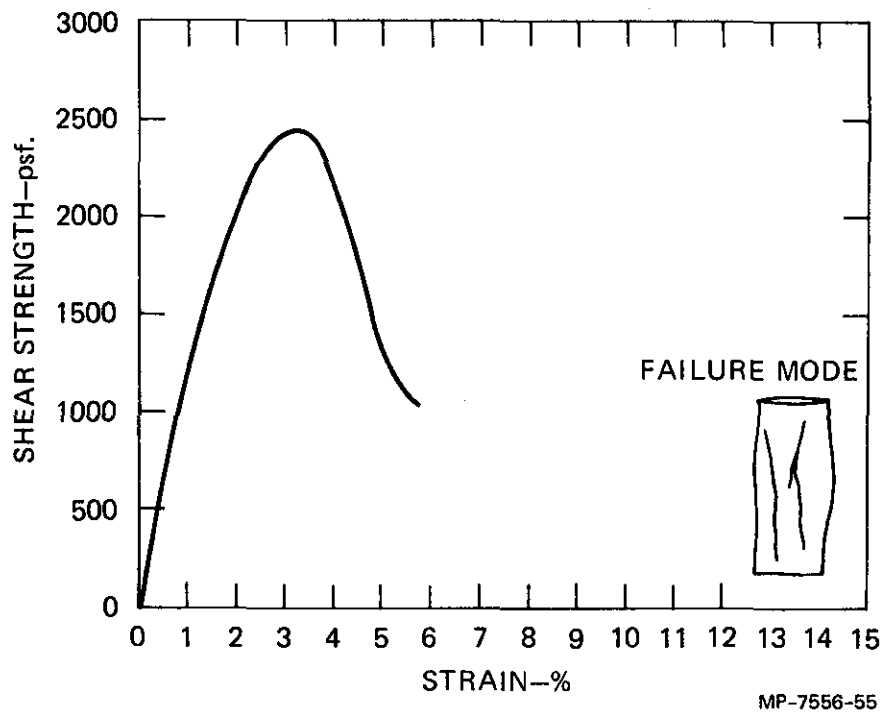
FIGURE B-4   UNCONFINED COMPRESSION TEST ON SAMPLE 4 (18-ft depth)
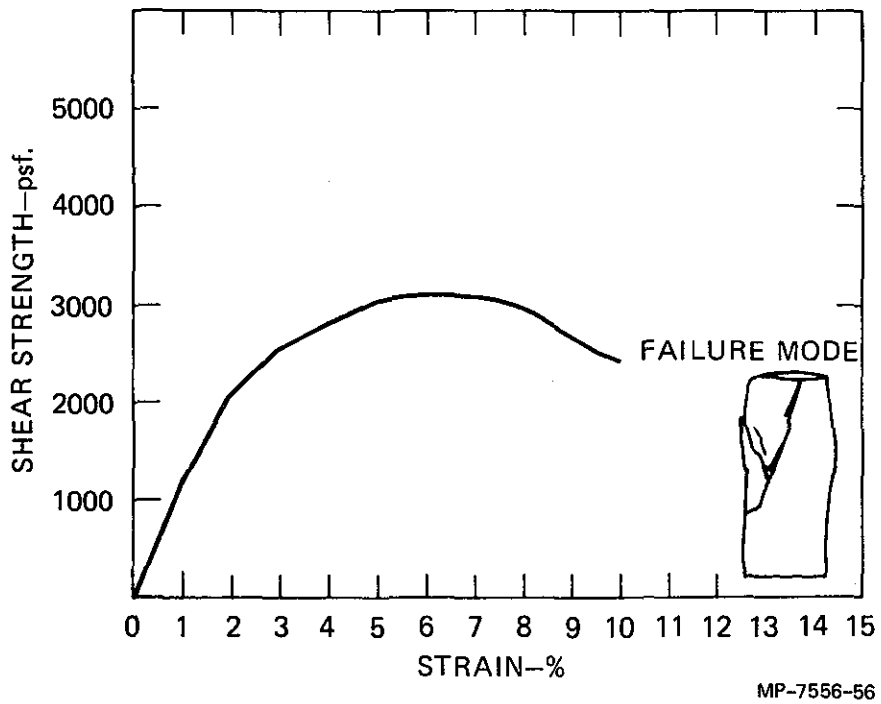
FIGURE B-5   UNCONFINED COMPRESSION TEST ON SAMPLE 5 (18-ft depth)

VERTICAL STRESS (psi) vs VERTICAL STRAIN — percent

3-ft Depth

18-ft Depth

10-ft Depth

MP-7556-57
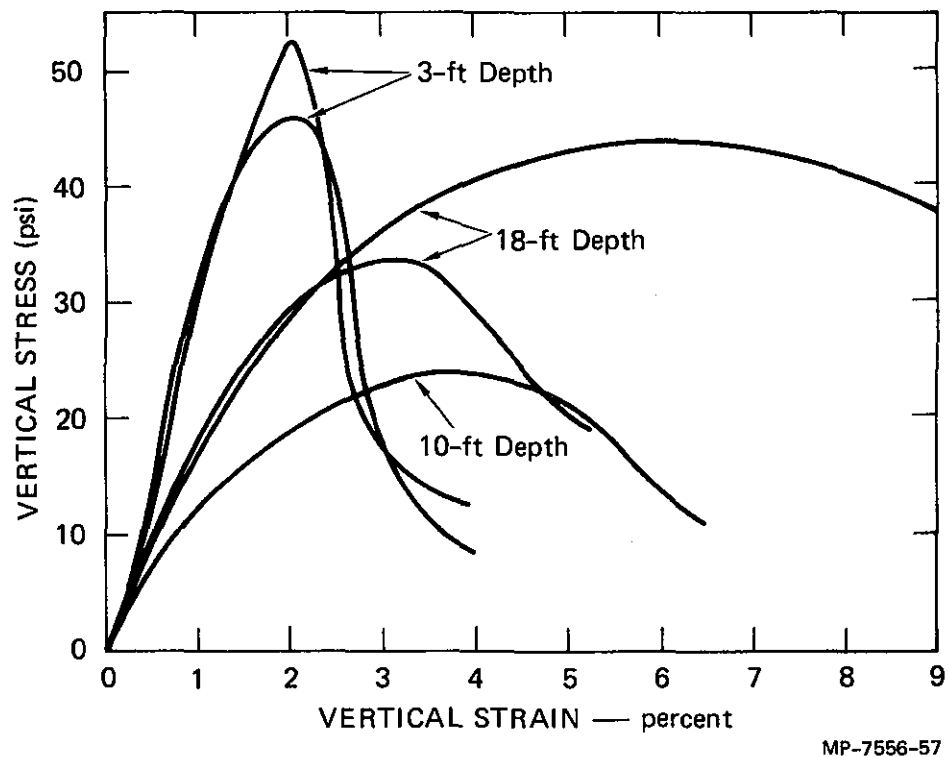
FIGURE B-6   SUMMARY OF UNCONFINED COMPRESSION TEST RESULTS

Comparison of the test results from the five tests showed the soil at the 3-ft depth was about three times as stiff in unconfined compression as that at the 10-ft depth, and about twice as stiff as that at the 18-ft depth (Figure B-6). The soil at the 3-ft depth also showed about one-half the ductility of that at the 10-ft and 18-ft depths.

Consolidation Tests

Three consolidation tests (one for each sample depth) were performed to measure the compressibility of the soil. A soil specimen was placed inside a steel ring, and porous stones were placed on the bottom and the top of the specimen. Pressure was then applied to the specimen through a loading head, with the porous stones allowing the free escape of the porewater. A dial indicator measured the downward movement of the loading head.

We allowed a one-day time interval between load increments for drainage of the porewater. The data from one test is shown in Figure B-7, where vertical strain is plotted as a function of time for each load increment. By considering only the final strain after each day of loading, we can plot vertical strain versus vertical stress from these data. Figure B-8 shows this plot for all three consolidation tests. Figure B-9 then shows the standard plot of void ratio versus the log of the vertical stress for the three consolidation tests. The trend in the data is one of increasing compressibility with increasing depth.

Consolidated, Undrained Triaxial Compression Tests

A set of three consolidated, undrained triaxial tests were performed on samples taken at the 10-ft depth to measure the strength and stress-strain relation for the soil. In these tests, a cylindrical 6-in.-long soil specimen is first capped with a porous stone at one end. The specimen is then enclosed within a thin rubber membrane and is placed inside a triaxial testing machine with the porous stone downward. The machine is filled with a fluid. Applying pressure to the fluid subjects the specimen to a hydrostatic compressive stress, σ_3. An initial
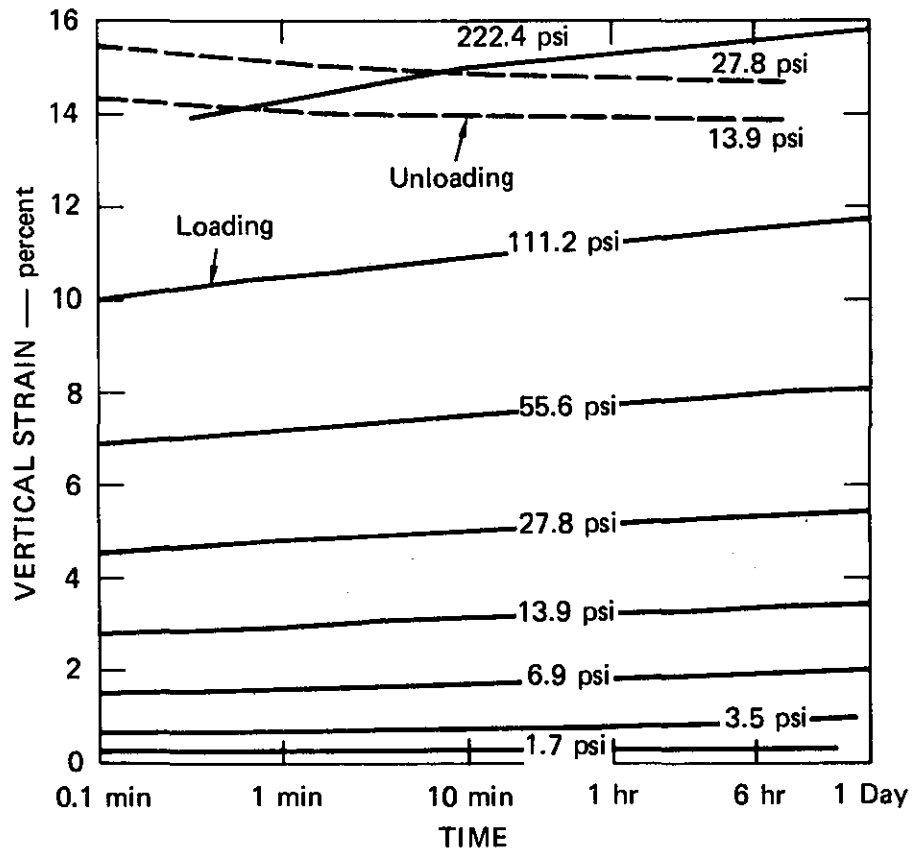
FIGURE B-7   DATA FROM TYPICAL CONSOLIDATION TEST SAMPLE 6 (18-ft depth)
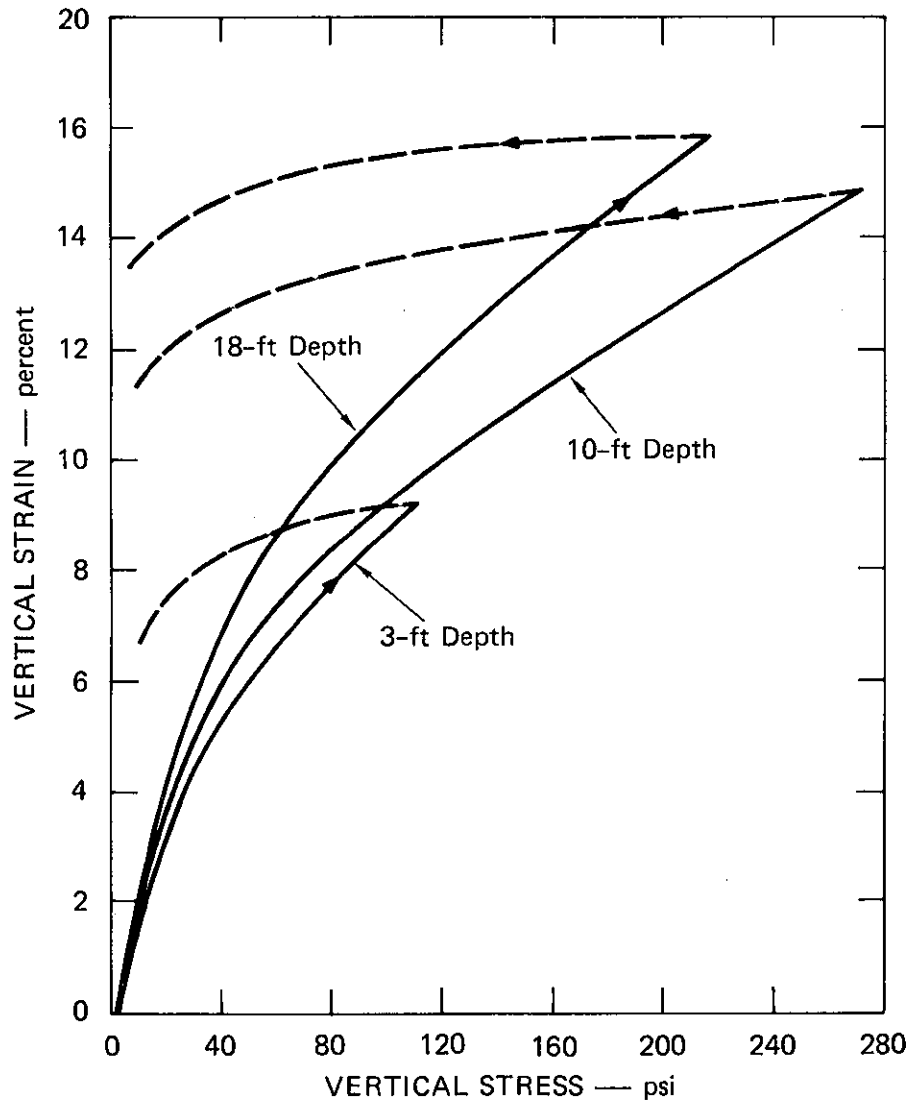
FIGURE B-8   SUMMARY OF CONSOLIDATION TEST RESULTS, VERTICAL STRAIN VERSUS
VERTICAL STRESS
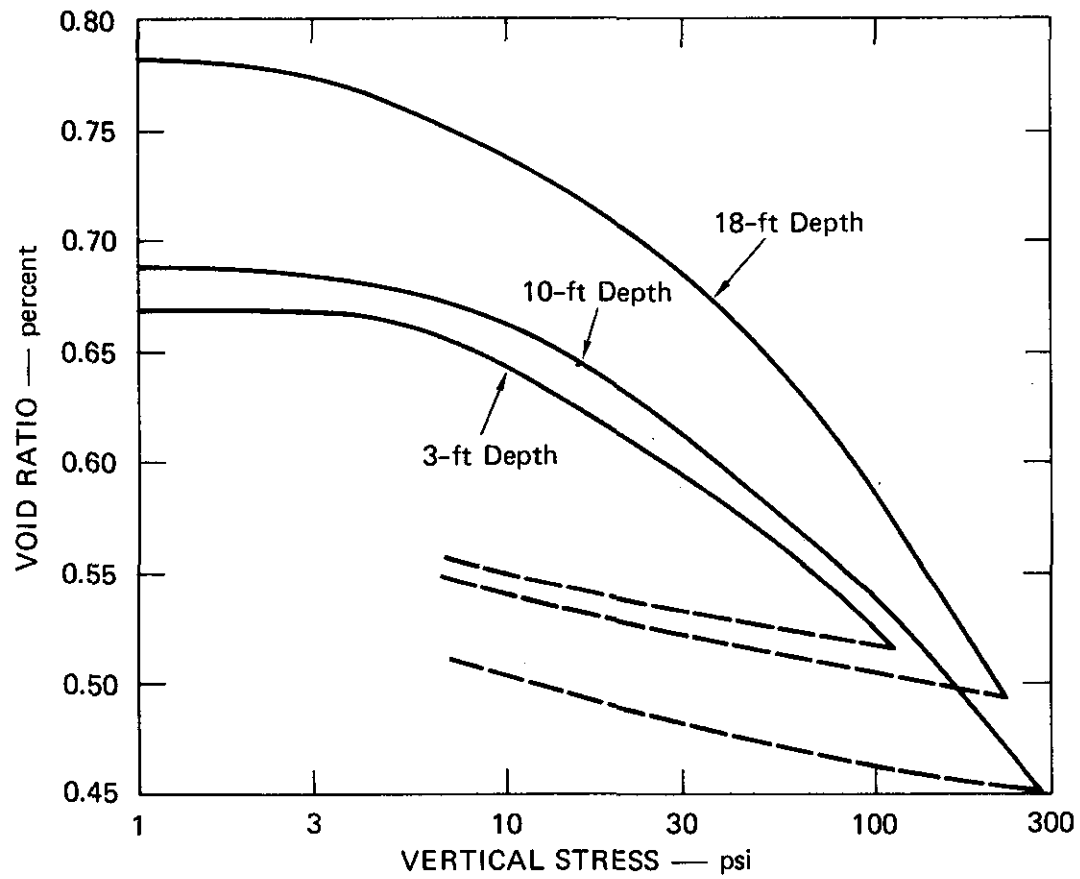
MA-7556-60

FIGURE B-9   SUMMARY OF CONSOLIDATION TEST RESULTS, VOID RATIO VERSUS
VERTICAL STRESS

B-11

porewater pressure, u_o, it also applied to the specimen through a line leading to the porous stone at the base of the specimen. (The porous stone and line are completely saturated with water.) Drainage of porewater either into or out from the sample is monitored by a burette connected in series with this line.

The specimen is allowed to consolidate under a constant σ_3 and u_o until no further drainage of porewater is observed. (The consolidation time was 8 days for these tests.) Once the consolidation process is complete, the line leading to the burette is close to prevent further drainage and the specimen is loaded by applying an additional vertical stress, $\Delta\sigma_1$, through a piston at the top of the machine. The vertical displacement of this piston is increased at a constant rate until failure of the specimen occurs. During the test, the additional vertical stress is measure along with the vertical displacement of the piston and the change in the porewater pressure, Δu.

Table B-1 gives the specimen data and testing conditions for the three tests. All three tests were performed with an initial porewater pressure, u_o, equal to 50 psi. The confining pressure, σ_3, was 60 psi, 80 psi, and 110 psi for Specimens 1, 2, and 3, respectively. The effective stress during consolidation, $\bar{\sigma}_3$ (the consolidation pressure), is determined by subtracting the porewater pressure, u_o, from the confining pressure, σ_3. Thus the consolidation pressure was 10 psi, 30 psi, and 60 psi for Specimens 1, 2, and 3, respectively.

Tables B-2 through B-4 give the data from the three triaxial tests. The vertical strain is calculated by dividing the strain dial reading by the sample length. The additional vertical stress, $\Delta\sigma_1$, is calculated by dividing the vertical load, measured by a proving ring, by the cross-sectional area of the specimen. (The cross-sectional area is corrected using the measured vertical strain and assuming a constant specimen volume.) The change in porewater pressure, Δu, is measured directly. The effective confining stress, $\bar{\sigma}_3$, is calculated by subtracting the porewater pressure u_o + u from the confining pressure, σ_3. The effective vertical stress, $\bar{\sigma}_1$, is calculated by adding the additional vertical stress, $\Delta\sigma_1$, to the effective confining stress, $\bar{\sigma}_3$.

Table B-1

SPECIMEN[*] DATA AND TESTING CONDITIONS FOR CONSOLIDATED UNDRAINED TRIAXIAL COMPRESSION TESTS

	Specimen 1	Specimen 2	Specimen 3
Initial Data			
Height (in.)	6.00	6.00	6.00
Diameter (in.)	2.853	2.852	2.840
Dry Unit Weight (pcf)	110.0	110.1	107.1
Water Content (%)	19.1	19.3	22.0
Saturation (%)	79	84	95
Final Data			
Height (in.)	4.80	5.10	5.52
Diameter (in.)	3.093	2.977	2.92
Dry Unit Weight (pcf)	117.0	115.8	110.2
Water Content	20.7	20.2	21.4
Saturation	100	100	99
Testing Conditions			
Consolidation Pressure, σ_3 (psi)	10	30	60
Confining Pressure, σ_3 (psi)	60	80	110
Internal Pressure, u (psi)	50	50	50
Parameter B (before axial loading)	0.91	0.79	0.76
Consolidation/Saturation (days)	8	8	8
Rate of Strain (in/min.)	0.00981	0.00795	0.00558

[*] Gray, white mottled, sandy, silty clay, highly calcareous; all specimens from undisturbed core samples.

Table B-2

CONSOLIDATED UNDRAINED TRIAXIAL COMPRESSION
TEST DATA ON SAMPLE 6
(10 ft - 10.5 ft depth)

2.8530	DIAMETER (in.)
6.0000	LENGTH (in.)
60.0000	CONFINING PRESSURE $\bar{\sigma}_3$(psi)
50.0000	INTERNAL PRESSURE (psi)
1.9100	PROVING RING CONSTANT (lbs/div)
10390.0000	INITIAL SR - 4 READING
31.2800	MICRO INCHES/PSI
6.3928	ORIGINAL AREA (in.^{2})
0.0098	STRAIN RATE (in./min)

STRAIN DIAL (in.)	STRAIN (%)	CORRECTED AREA (in^2)	PR. DIAL (div)	$\Delta\sigma_1$ (psi)	SR—4 (micro-in)	ΔU (psi)	$\bar{\sigma}_3$ (psi)	$\bar{\sigma}_1$ (psi)
.000	00.0000	6.3920	.0	.0	10390	-.0	10.0	10.0
.006	.1000	6.3990	15.8	4.7	10333	1.6	8.3	13.0
.012	.2000	6.4050	25.0	7.4	10301	2.8	7.1	14.6
.018	.3000	6.4120	30.0	8.9	10278	3.5	6.4	15.3
.030	.5000	6.4240	36.0	10.7	10240	4.7	5.2	15.9
.060	1.0000	6.4570	44.7	13.2	10220	5.4	4.5	17.7
.090	1.5000	6.4900	51.2	15.0	10209	5.7	4.2	19.2
.120	2.0000	6.5230	57.7	16.8	10217	5.5	4.4	21.3
.150	2.5000	6.5560	63.4	18.4	10219	5.4	4.5	23.0
.180	3.0000	6.5900	69.9	20.2	10238	4.8	5.1	25.3
.210	3.5000	6.6240	75.0	21.6	10250	4.4	5.5	27.1
.240	4.0000	6.6590	81.5	23.3	10272	3.7	6.2	29.6
.300	5.0000	6.7290	91.0	25.8	10315	2.3	7.6	33.4
.330	5.5000	6.7640	95.0	26.8	10331	1.8	8.1	34.9
.360	6.0000	6.8000	98.3	27.6	10352	1.2	8.7	36.3
.390	6.5000	6.8370	101.5	28.3	10367	.7	9.2	37.6
.420	7.0000	6.8730	104.6	29.0	10387	.0	9.9	38.9
.450	7.5000	6.9110	107.0	29.5	10397	-.2	10.2	39.7
.480	8.0000	6.9480	109.3	30.0	10412	-.7	10.7	40.7
.510	8.5000	6.9860	111.9	30.5	10424	-1.0	11.0	41.6
.540	9.0000	7.0250	114.0	30.9	10432	-1.3	11.3	42.3
.570	9.5000	7.0630	116.3	31.4	10446	-1.7	11.7	43.2
.600	10.0000	7.1030	119.0	31.9	10453	-2.0	12.0	44.0
.660	11.0000	7.1820	122.9	32.6	10469	-2.5	12.5	45.2
.720	12.0000	7.2640	127.0	33.3	10488	-3.1	13.1	46.5
.780	13.0000	7.3480	130.9	34.0	10508	-3.7	13.7	47.7
.840	14.0000	7.4330	134.3	34.5	10518	-4.0	14.0	48.6
.900	15.0000	7.5200	138.5	35.1	10535	-4.6	14.6	49.8
.960	16.0000	7.6100	141.8	35.5	10551	-5.1	15.1	50.7
1.020	17.0000	7.7020	145.0	35.9	10563	-5.5	15.5	51.4
1.080	18.0000	7.7960	148.2	36.3	10577	-5.9	15.9	52.2
1.140	19.0000	7.8920	151.1	36.5	10588	-6.3	16.3	52.8
1.200	20.0000	7.9910	153.3	36.6	10598	-6.6	16.6	53.2

Table B-3

CONSOLIDATED UNDRAINED TRIAXIAL COMPRESSION
TEST DATA ON SAMPLE 7
(10.5 ft - 11 ft depth)

2.8520   DIAMETER (in.)
6.0000   LENGTH (in.)
80.0000   CONFINING PRESSURE $\bar{\sigma}_3$(psi)
50.0000   INTERNAL PRESSURE (psi)
1.9100   PROVING RING CONSTANT (lbs/div)
10390.0000   INITIAL SR - 4 READING
31.2800   MICRO INCHES/PSI
6.3883   ORIGINAL AREA (in.^{2})
0.0080   STRAIN RATE (in./min)

STRAIN DIAL (in.)	STRAIN (%)	CORRECTED AREA (in^2)	PR. DIAL (div)	$\Delta\sigma_1$ (psi)	SR—4 (micro—in)	ΔU (psi)	$\bar{\sigma}_3$ (psi)	$\bar{\sigma}_1$ (psi)
.000	00.0000	6.3880	.0	.0	10390	-.0	30.0	30.0
.006	.1000	6.3940	24.0	7.1	10323	2.1	27.8	35.0
.012	.2000	6.4010	45.5	13.5	10249	4.5	25.4	39.0
.018	.3000	6.4070	59.8	17.8	10186	6.5	23.4	41.3
.030	.5000	6.4200	80.2	23.8	10120	8.6	21.3	45.2
.060	1.0000	6.4520	114.3	33.8	10050	10.8	19.1	52.9
.090	1.5000	6.4850	140.2	41.2	10048	10.9	19.0	60.3
.120	2.0000	6.5180	157.8	46.2	10078	9.9	20.0	66.2
.150	2.5000	6.5520	169.5	49.4	10121	8.5	21.4	70.8
.180	3.0000	6.5850	177.1	51.3	10158	7.4	22.5	73.9
.210	3.5000	6.6200	183.5	52.9	10192	6.3	23.6	76.6
.240	4.0000	6.6540	188.5	54.1	10227	5.2	24.7	78.8
.270	4.5000	6.6890	192.0	54.8	10249	4.5	25.4	80.3
.300	5.0000	6.7240	195.3	55.4	10272	3.7	26.2	81.7
.333	5.5500	6.7630	198.8	56.1	10302	2.8	27.1	83.3
.360	6.0000	6.7960	201.6	56.6	10314	2.4	27.5	84.2
.390	6.5000	6.8320	204.2	57.0	10333	1.8	28.1	85.2
.420	7.0000	6.8690	208.0	57.8	10348	1.3	28.6	86.4
.480	8.0000	6.9430	211.7	58.2	10380	.3	29.6	87.9
.540	9.0000	7.0200	216.7	58.9	10403	-.4	30.4	89.3
.600	10.0000	7.0980	222.0	59.7	10430	-1.2	31.2	91.0
.660	11.0000	7.1770	224.0	59.6	10454	-2.0	32.0	91.6
.720	12.0000	7.2590	225.1	59.2	10474	-2.6	32.6	91.9
.780	13.0000	7.3420	227.3	59.1	10494	-3.3	33.3	92.4
.840	14.0000	7.4280	227.8	58.5	10511	-3.8	33.8	92.4
.900	15.0000	7.5150	228.0	57.9	10530	-4.4	34.4	92.4

Table B-4

CONSOLIDATED UNDRAINED TRIAXIAL COMPRESSION
TEST DATA ON SAMPLE 8
(11 ft - 11.5 ft depth)

2.8400 DIAMETER (in.)
6.0000 LENGTH (in.)
110.0000 CONFINING PRESSURE $\bar{\sigma}_3$ (psi)
50.0000 INTERNAL PRESSURE (psi)
1.9100 PROVING RING CONSTANT (lbs/div)
10390.0000 INITIAL SR - 4 READING
31.2800 MICRO INCHES/PSI
6.3347 ORIGINAL AREA (in.^{2})
0.0056 STRAIN RATE (in./min)

STRAIN DIAL (in.)	STRAIN (%)	CORRECTED AREA (in^2)	PR. DIAL (div)	$\Delta\sigma_1$ (psi)	SR—4 (micro–in)	ΔU (psi)	$\bar{\sigma}_3$ (psi)	$\bar{\sigma}_1$ (psi')
.000	00.0000	6.3340	.0	.0	10390	-.0	60.0	60.0
.006	.1000	6.3410	25.5	7.6	10361	.9	59.0	66.7
~~.013~~	~~.2166~~	~~6.3480~~	~~53.5~~	~~16.0~~	~~10310~~	~~2.5~~	~~57.4~~	~~73.5~~
.012	.2000	6.3470	53.5	16.0	10310	2.5	57.4	73.5
.018	.3000	6.3530	77.0	23.1	10225	5.2	54.7	77.8
.030	.5000	6.3660	115.0	34.5	10103	9.1	50.8	85.3
.060	1.0000	6.3980	171.2	51.1	9829	17.9	42.0	93.1
.090	1.5000	6.4310	203.5	60.4	9647	23.7	36.2	96.6
.120	2.0000	6.4630	224.0	66.1	9558	26.5	33.4	99.5
.150	2.5000	6.4970	237.9	69.9	9519	27.8	32.1	102.0
.180	3.0000	6.5300	250.0	73.1	9513	28.0	31.9	105.0
.210	3.5000	6.5640	259.0	75.3	9530	27.4	32.5	107.8
.240	4.0000	6.5980	266.0	77.0	9545	27.0	32.9	109.9
.270	4.5000	6.6330	272.5	78.4	9573	26.1	33.8	112.3
.300	5.0000	6.6680	276.1	79.0	9600	25.2	34.7	113.8
.330	5.5000	6.7030	277.3	79.0	9621	24.5	35.4	114.4
.360	6.0000	6.7390	279.0	79.0	9639	24.0	35.9	115.0
.390	6.5000	6.7750	281.1	79.2	9653	23.5	36.4	115.6
.420	7.0000	6.8110	282.6	79.2	9669	23.0	36.9	116.1
.480	8.0000	6.8850	283.9	78.7	9668	23.0	36.9	115.6

Figure B-10 shows a plot of the effective stress paths in $\bar{\sigma}_1 - \bar{\sigma}_3$ versus $\bar{\sigma}_3$ space for the three tests. A line bounding these stress paths has a slope, ω, between 60° and 64° and an x-intercept, σ_u, representing the unconfined compressive strength, between 12 and 14 psi. This line represents a yield surface, since a point on this line represents the limiting value of effective stress for the given $\bar{\sigma}_3$. For the same reason, the yield point on each stress path can be defined as the point where the stress path becomes tangent to the yield surface. The yield points are shown by the solid circles in Figure B-10.

Figure B-11 is a plot of both the principal stress difference, $\bar{\sigma}_1 - \bar{\sigma}_3$, and the change in porewater pressure, Δu, versus axial strain for the triaxial test on Sample 2 with a consolidation pressure of 30 psi. Again the yield point, taken from Figure B-10, is shown by the solid circle. Note that the axial strain increases greatly when the principal stress difference increases above the yield point.

To aid in the interpretation of the yield criterion given in $\bar{\sigma}_1 - \bar{\sigma}_3$ versus $\bar{\sigma}_3$ space, it is useful to show how this yield criterion maps into a Mohr envelope in τ (shear stress) versus $\bar{\sigma}_n$ (effective normal stress) space. The yield function in $\bar{\sigma}_1 - \bar{\sigma}_3$ versus $\bar{\sigma}_3$ space is given by

$$\bar{\sigma}_1 = (1 + \tan \omega)\, \bar{\sigma}_3 + \sigma_u \qquad\qquad (B\text{-}1)$$

In τ versus $\bar{\sigma}_n$ space, yield occurs when the Mohr circle representing the state of stress in the body comes in contact with the yield envelope given by

$$\tau = c + \tan \phi \; \bar{\sigma}_n \qquad\qquad (B\text{-}2)$$

where ϕ is the angle of internal friction and c is the cohesion of the soil. The maximum and minimum principal stresses at yield are $\bar{\sigma}_1$ and $\bar{\sigma}_3$, respectively. Shear stress, τ, and effective normal stress, $\bar{\sigma}_n$, on the yield plane of the specimen are related to $\bar{\sigma}_1$ and $\bar{\sigma}_3$ by

$$\tau = \left(\frac{\bar{\sigma}_1 - \bar{\sigma}_3}{2}\right) \cos \phi \qquad\qquad (B\text{-}3)$$

B-17

$$\phi = \sin^{-1}\left[\frac{\tan \omega}{2 + \tan \omega}\right]$$
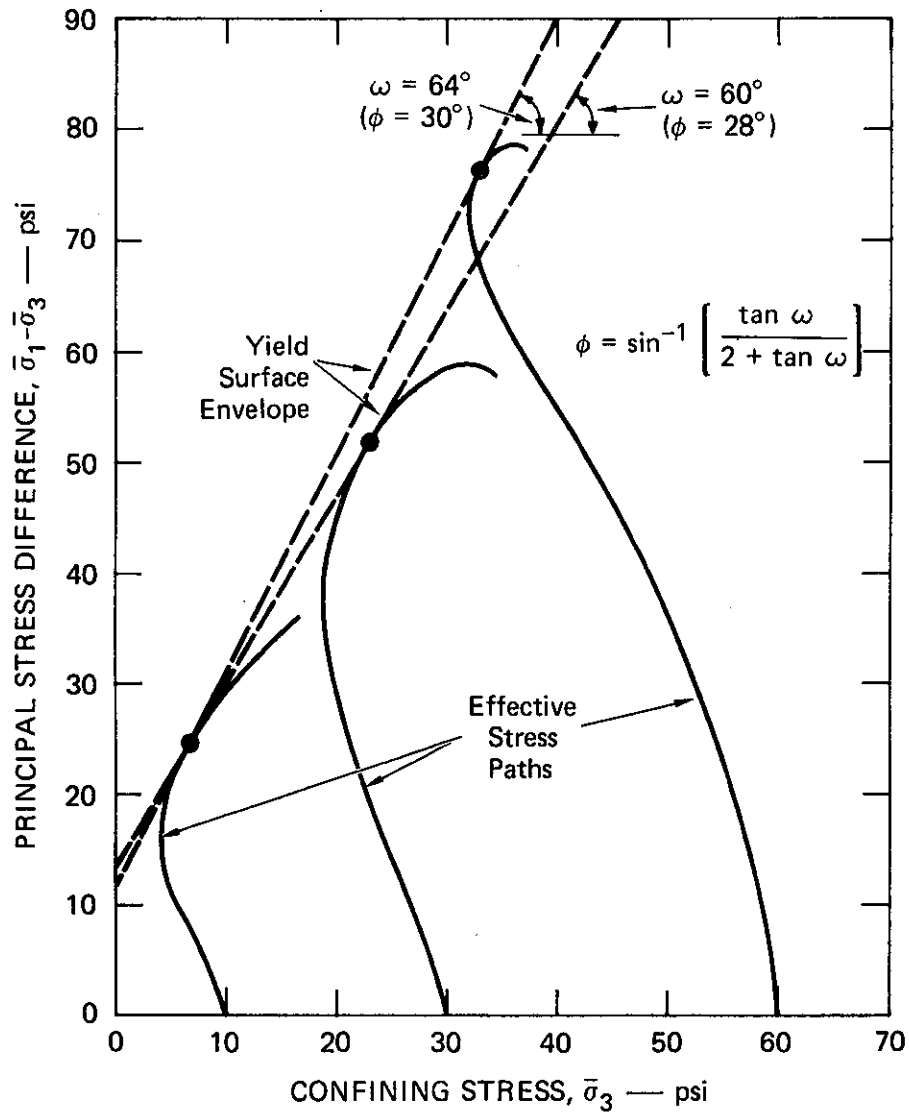
FIGURE B-10 EFFECTIVE STRESS PATHS FROM CONSOLIDATED UNDRAINED TRIAXIAL
COMPRESSION TESTS (Depth 10 ft to 11.5 ft)

MA-7556-61

B-18
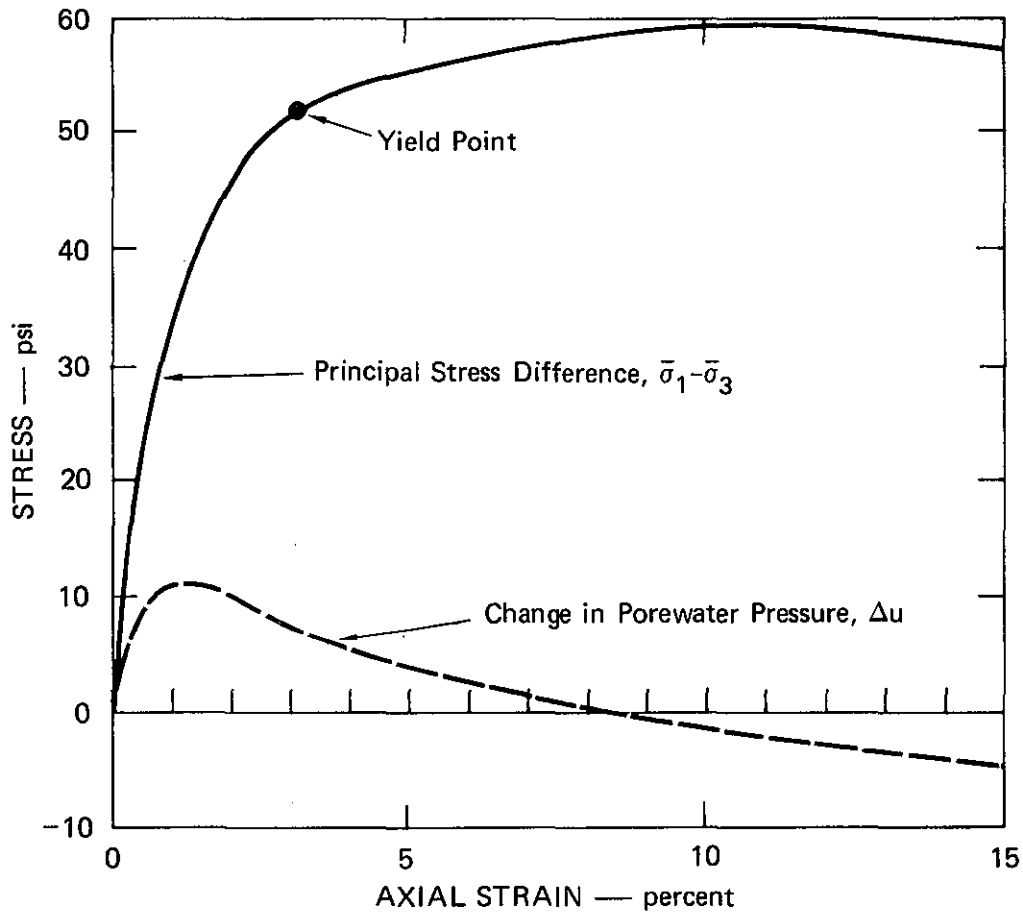
FIGURE B-11 PRINCIPAL STRESS DIFFERENCE AND CHANGE IN POREWATER PRESSURE VERSUS AXIAL STRAIN FOR A TYPICAL CONSOLIDATED UNDRAINED TRIAXIAL COMPRESSION TEST

(Sample No. 2; 10-1/2 to 11-ft depth; consolidation pressure of 30 psi)

and

$$\bar{\sigma}_n = \bar{\sigma}_3 + (1 - \sin \phi) \left(\frac{\bar{\sigma}_1 - \bar{\sigma}_3}{2} \right) \tag{B-4}$$

Substituting these expressions in Eq. (B-2) yields

$$\bar{\sigma}_1 = \left(\frac{1 + \sin \phi}{1 - \sin \phi} \right) \bar{\sigma}_3 + c \left(\frac{2 \cos \phi}{1 - \sin \phi} \right) \tag{B-5}$$

A comparison of this result with Eq. (B-1) shows that for these two yield functions to be equivalent, the following relations must hold

$$\phi = \sin^{-1} \left(\frac{\tan \omega}{2 + \tan \omega} \right) \tag{B-6}$$

$$c = \left(\frac{1 - \sin \phi}{2 \cos \phi} \right) \sigma_u \tag{B-7}$$

Values of $\omega = 64°$ and $\bar{\sigma}_u = 12$ psi give $\phi = 30°$ and $c = 3.4$ psi when inserted into Eqs. (B-6) and (B-7).

Figure B-12 shows the Mohr envelope for the three tests. Mohr circles have been constructed for each of the yield point stress states. The envelope has a slope of 30° and y- intercept of 3 psi. These values are consistent with the values of ϕ and c given by Eqs. (B-6) and (B-7).
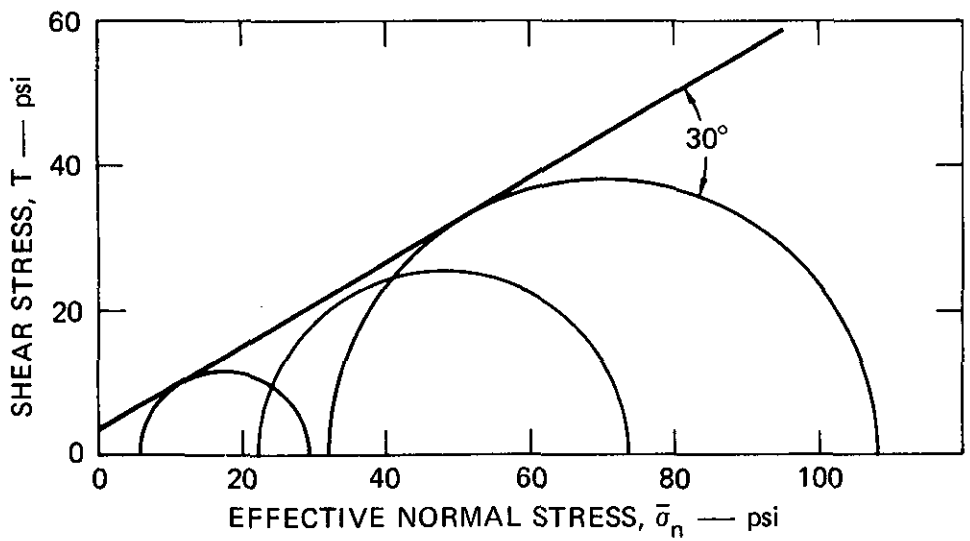
FIGURE B-12 MOHR'S ENVELOPE FROM CONSOLIDATED UNDRAINED TRIAXIAL
COMPRESSION TEST

(Depth 10 ft to 11.5 ft)

Appendix C

ACCELERATION BASELINE CORRECTION

Since the actual ground motion in the tests is recorded in terms
of acceleration-time histories, the corresponding velocity and
displacement-time histories must be obtained by integeration. Very
small errors in the acceleration-time history, arising from either
instrument error or errors in the digitizing process, can cause sub-
stantial errors in velocity and displacement. To minimize these errors,
we applied an acceleration baseline correction to each record. The
adjustment procedure uses a first-degree polynominal to correct the
acceleration baseline. The two coefficients are chosen by a standard
method, consisting of minimizing the square of the velocity over the
duration of the record. This method is explained below.

The corrected acceleration, $\ddot{x}_c(t)$, is given by

$$\ddot{x}_c(t) = \ddot{x}_r(t) - c_o - c_1 t \qquad (C-1)$$

where $\ddot{x}_r(t)$ is the recorded acceleration and the c's are unknown
coefficients. The corrected velocity, $\dot{x}_c(t)$, is then written by
integrating Eq. (C-1). Thus

$$\dot{x}_c(t) = \int_o^t \ddot{x}_r(\tau)d\tau - c_o t - \frac{1}{2} c_1 t^2 + v_o \qquad (C-2)$$

where v_o is the initial velocity (equal to zero in our application).
As stated above, coefficients c_o and c_1 are found by minimizing $\dot{x}_c^2(t)$
with respect to c_o and c_1 over the duration of the record, T. Thus,
we can write two equations:

$$\frac{\partial}{\partial c_o} \int_o^T \dot{x}_c^2(t)dt = 0 \qquad (C-3)$$

C-1

and

$$\frac{\partial}{\partial c_1} \int_o^T \dot{x}_c^{\ 2}(t)dt = 0 \qquad (C\text{-}4)$$

By substituting $\dot{x}_c$ (t) from Eq. (C-2) into Eqs. (C-3) and (C-4), we obtain

$$\frac{\partial}{\partial c_o} \int_o^T \left(\int_o^t \ddot{x}_r(\tau)d\tau - c_o t - \frac{1}{2} c_1 t^2 \right)^2 dt = 0 \qquad (C\text{-}5)$$

and

$$\frac{\partial}{\partial c_1} \int_o^T \left(\int_o^t \ddot{x}_r(\tau)d\tau - c_o t - \frac{1}{2} c_1 t^2 \right)^2 dt = 0 \qquad (C\text{-}6)$$

By taking the partial derivatives, we obtain

$$\int_o^T 2t \left(\int_o^t \ddot{x}_r(\tau)d\tau - c_o t - \frac{1}{2} c_1 t^2 \right) dt = 0 \qquad (C\text{-}7)$$

and

$$\int_o^T t^2 \left(\int_o^t \ddot{x}_r(\tau)d\tau - c_o t - \frac{1}{2} c_1 t^2 \right) dt = 0 \qquad (C\text{-}8)$$

Rearrangement and integration gives

$$2c_o \int_o^T t^2 dt + c_1 \int_o^T t^3 dt = \int_o^T 2t \left(\int_o^t \ddot{x}_r(\tau)d\tau \right) dt \qquad (C\text{-}9)$$

and

$$c_o \int_o^T t^3 dt + \frac{1}{2} c_1 \int_o^T t^4 dt = \int_o^T t^2 \left(\int_o^t \ddot{x}_r(\tau)d\tau \right) dt \qquad (C\text{-}10)$$

Performing the remaining integration using integration by parts on the right-hand side gives

$$\frac{2}{3} c_o T^3 + \frac{1}{4} c_1 T^4 = t^2 \int_o^t \ddot{x}_r(t)dt - \int_o^t t^2 \ddot{x}_r(t)dt \qquad \text{(C-11)}$$

and

$$\frac{1}{4} c_o T^4 + \frac{1}{10} c_1 T^5 = \frac{1}{3} T^3 \int_o^t \ddot{x}_t(t)dt - \int_o^t \frac{t^3}{3} \ddot{x}_r(t)dt \ . \qquad \text{(C-12)}$$

These two linear equations can be solved for the two unknown coefficients c_o and c_1. Equation (C-1) can then be used to calculate the corrected acceleration-time history.

Appendix D

ELASTIC-PLASTIC ANALYSIS OF A PRESSURIZED CYLINDRICAL HOLE

To estimate the elastic-plastic response around a single source, we consider an infinite body with a pressurized cylindrical hole, as shown in Figure D-1. The radius of the cavity is a_s, and the internal pressure is P_s. As P_s is increased, yielding will occur starting at the cavity wall. A plastic region will be formed and extend to a radius R when P_s has reached its peak. The rest of the body will remain elastic.

Fundamental Equations

The following equations are valid in both the elastic and plastic regions:

Equilibrium

$$\frac{d\sigma_r}{dr} + \frac{\sigma_r - \sigma_\theta}{r} = 0 \tag{D-1}$$

Strain-Displacement

$$\varepsilon_r = \frac{du}{dr} \ , \ \varepsilon_\theta = \frac{u}{r} \tag{D-2}$$

Compatibility

$$\frac{d\varepsilon_\theta}{dr} + \frac{\varepsilon_\theta - \varepsilon_\theta}{r} = 0 \tag{D-3}$$

D-1

Elastic Zone

Plastic Zone

P_s

a_s

R
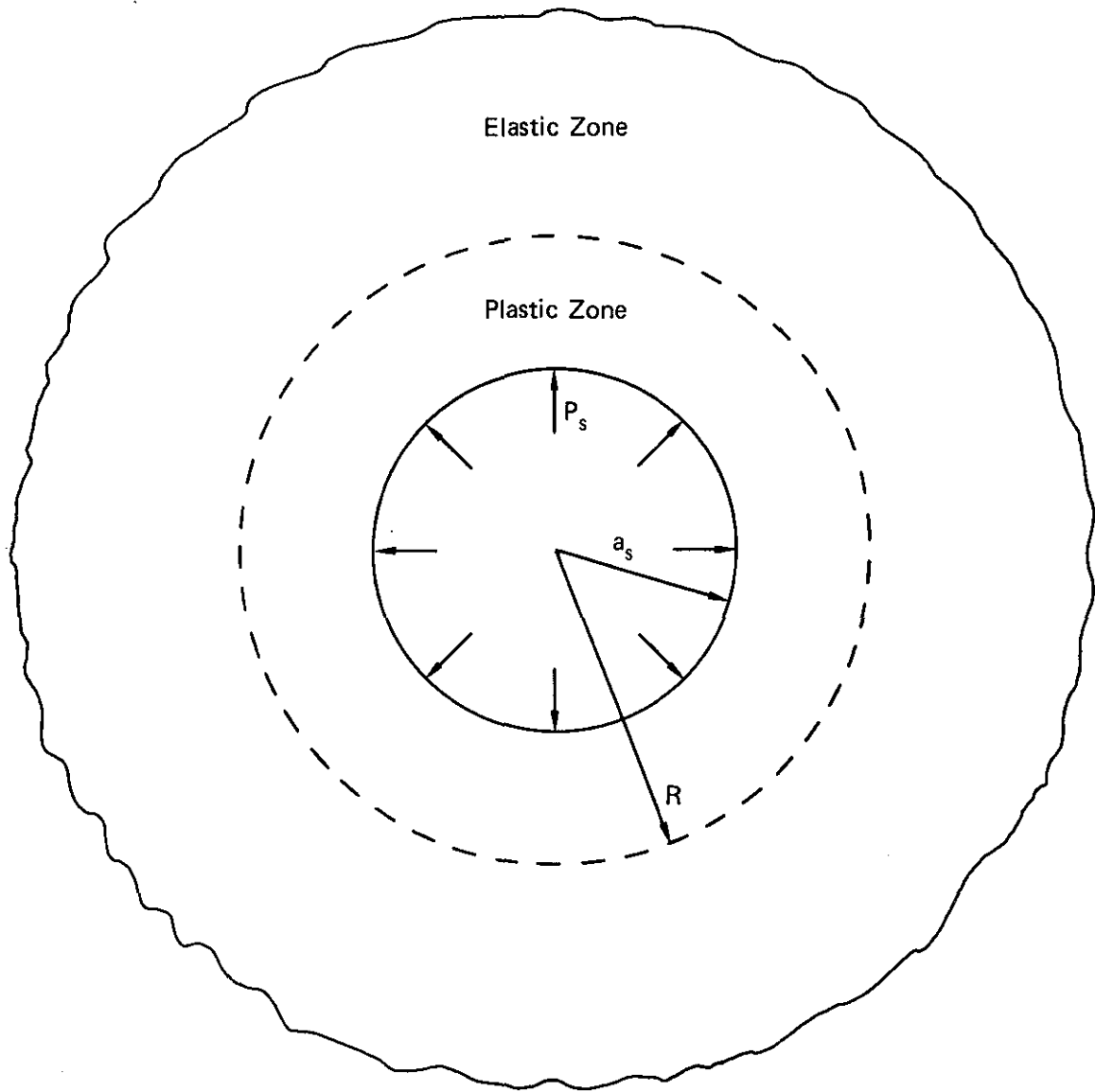
FIGURE D-1   PRESSURIZED CAVITY IN AN INFINITE MOHR-COULOMB SOLID

Stress-Strain

$$\varepsilon_r = \frac{1}{E'} [\sigma_r - \nu' \sigma_\theta] + \varepsilon_{rp} \qquad \text{(D-4)}$$

$$\varepsilon_\theta = \frac{1}{E'} [\sigma_\theta - \nu' \sigma_r] + \varepsilon_{\theta p}$$

$$\varepsilon_z = 0$$

where a plane strain condition is assumed to hold and therefore

$$E' = \frac{E}{(1-\nu^2)} \; , \quad \nu' = \frac{\nu}{1-\nu} \qquad \text{(D-5)}$$

E and ν are the Young's Modulus and Poisson's ratio, respectively; and ε_{rp} and $\varepsilon_{\theta p}$ are the radial and circumferential plastic strains, respectively.

Mohr-Coulomb Yield Criterion

The Mohr-Coulomb yield criterion is assumed to be valid. Since we expect σ_r to be greater than σ_θ (with compressive stress positive), this criterion may be expressed as

$$F = \sigma_r - N_\varphi \sigma_\theta - \sigma_u = 0 \qquad \text{(D-6)}$$

where

$$N_\varphi = \frac{1 + \sin \varphi}{1 + \sin \varphi}$$

σ_u is the unconfined compressive strength of the material, and φ is the angle of internal friction.

Analysis of the Elastic Zone

The elastic and plastic regions may be treated separately, as shown in Figure D-2, where a fictitious boundary at $r = R$ has been introduced. The stresses in the elastic region may be written as (see Timoshenko and Goodier)[*]

$$\sigma_r = P_R \frac{R^2}{r^2} \quad , \quad \sigma_\theta = - P_R \frac{R^2}{r^2} \tag{D-8}$$

where P_R and R are unknown. We may eliminate P_R by making use of the fact that the stresses must satisfy the yield condition

$$\sigma_r - N\sigma_\theta = \sigma_u$$

at $r = R$. The stresses now become

$$\sigma_r = \frac{\sigma_u}{1 + N_\varphi} \frac{R^2}{r^2} \quad , \quad \sigma_\theta = - \frac{\sigma_u}{1 + N_\varphi} \frac{R^2}{r^2} \tag{D-9}$$

The strains and displacement may be obtained through Eqs. (D-2) and (D-4) with $\varepsilon_{rp} = 0$ and $\varepsilon_{\theta p} = 0$.

Analysis of the Plastic Zone

In the plastic zone, the material is assumed to be elastic-perfectly plastic; thus, the stresses must satisfy the yield condition

$$\sigma_\theta = (\sigma_r - \sigma_u)/N_\varphi \tag{D-10}$$

throughout the plastic zone. Substituting this into the equilibrium equation and making use of the boundary condition

$$\sigma_r = P_s \text{ at } r = a_s ,$$

---

[*]S. A. Timoshenko and J. N. Goodier, *Theory of Elasticity* (McGraw-Hill Book Company, New York, 1951).
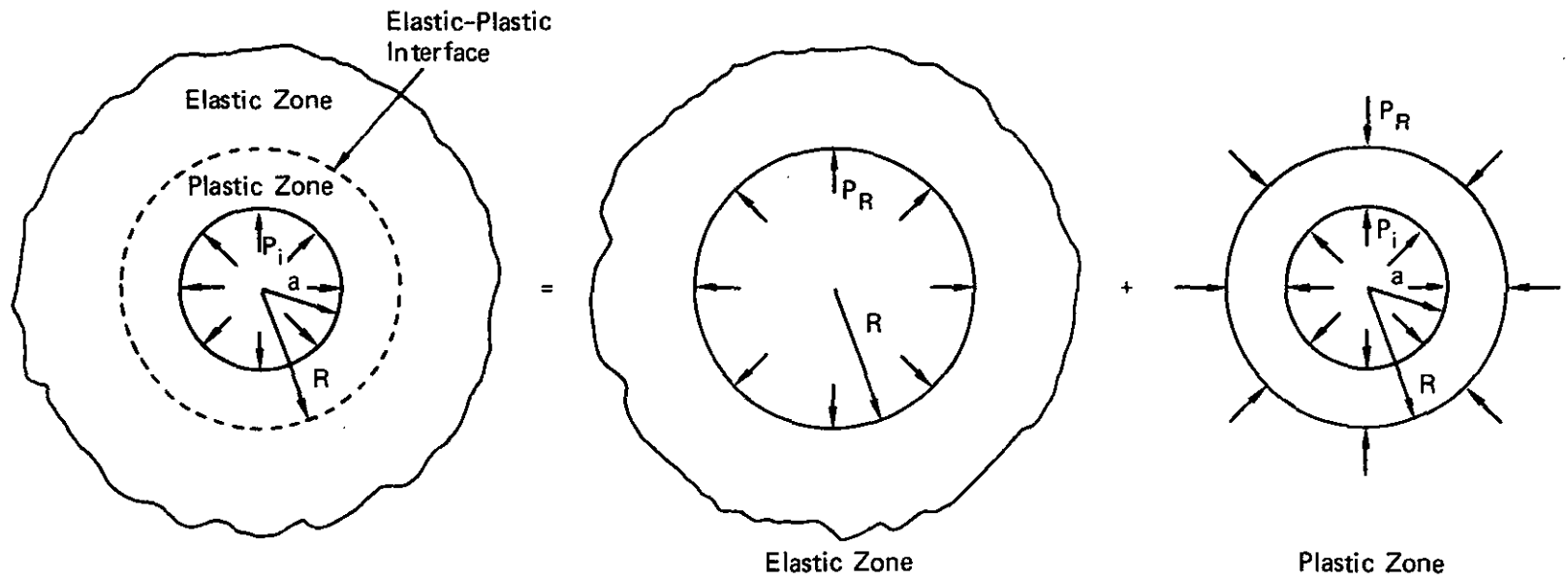
FIGURE D-2   ELASTIC AND PLASTIC ZONES CONSIDERED SEPARATELY

we obtain the stresses in the plastic zone as

$$\sigma_r = -\frac{\sigma_u}{N_\varphi - 1} + \left[P_s + \frac{\sigma_u}{N_\varphi - 1} \right] \left(\frac{r}{a_s} \right)^{-\left(\frac{N_\varphi - 1}{N} \right)} \qquad (D\text{-}11)$$

$$\sigma_\theta = -\frac{\sigma_u}{N_\rho - 1} + \frac{1}{N_\varphi} \left[P_s + \frac{\sigma_u}{N_\varphi - 1} \right] \left(\frac{r}{a_s} \right)^{-\left(\frac{N_\varphi - 1}{N_\varphi} \right)}$$

To obtain the elastic-plastic radius R, we make use of the continuity of radial stress across the elastic-plastic boundary; that is,

$$\sigma_r \text{ elastic zone} = \sigma_r \text{ plastic zone at } r = R \ ,$$

which yields

$$\frac{R}{a} = \left\{ \frac{N_\varphi + 1}{2N_\varphi} \left(1 + (N_\varphi - 1) \frac{P_s}{\sigma_u} \right) \right\}^{\left(\frac{N_\varphi}{N_\varphi - 1} \right)} \qquad (D\text{-}12)$$

To obtain the strains and displacement in the plastic region, we use the flow rule associated with the Mohr-Coulomb yield criterion (D-6). The flow rule gives the plastic strain rates as

$$\dot{\varepsilon}_{rp} = \dot{\lambda} \frac{\partial f}{\partial \sigma_r} = \dot{\lambda}$$

$$\qquad (D\text{-}13)$$

$$\dot{\varepsilon}_{\theta p} = \dot{\lambda} \frac{\partial f}{\partial \sigma_\theta} = -N_\varphi \dot{\lambda}$$

or

$$\dot{\varepsilon}_{\theta p} = -N_\varphi \dot{\varepsilon}_{rp} \ . \qquad (D\text{-}14)$$

Since we assume the loading to be monotonic, we may integrate Eq. (D-14) to obtain

$$\varepsilon_{\theta p} = -N_\varphi \varepsilon_{rp} \ . \qquad (D\text{-}15)$$

We note that Eq. (D-15) indicates that the material is not incompressible since

$$\varepsilon_{rp} + \varepsilon_{\theta p} \neq 0 \quad . \tag{D-16}$$

In fact, as plastic flow takes place, the material increases in volume. A discussion of this phenomenon may is given by Drucker and Prager.[*]

From Eqs. (D-4), (D-11), and (D-15), we may write the strains in the plastic zone as

$$\varepsilon_r = \frac{1}{E'} \left\{ - (1 - \nu') \frac{\sigma_u}{N_f - 1} + \left(1 - \frac{\nu'}{N_\varphi}\right)\left(P_s + \frac{\sigma_u}{N_\varphi - 1}\right)\left(\frac{r}{a_s}\right)^{-\left(\frac{N_\varphi - 1}{N_\varphi}\right)} \right\}$$
$$+ \varepsilon_{rp} \tag{D-17}$$

$$\varepsilon_\theta = \frac{1}{E'} \left\{ - (1 - \nu') \frac{\sigma_u}{N_\varphi - 1} + \left(\frac{1}{N_\varphi} - \nu'\right)\left(P_s + \frac{\sigma_u}{N_\varphi - 1}\right)\left(\frac{r}{a_s}\right)^{-\left(\frac{N_\varphi - 1}{N_p}\right)} \right\}$$
$$- N_\varphi \varepsilon_{rp}$$

where ε_{rp} remains to be determined. Substituting these expressions into the compatibility equation (D-3) and making use of the fact that the plastic strain must vanish at the elastic-plastic boundary, that is,

$$\varepsilon_{rp} = 0 \text{ at } r = R \ ,$$

gives

$$\varepsilon_{rp} = \frac{1}{E'} \frac{1}{2N_\varphi^2} \left\{ 2(1 + \nu')N_\varphi - (2\nu' + 1)N_\varphi^2 - 1 \right\} \ \chi$$

$$\left(P_s + \frac{\sigma_u}{N_\varphi - 1}\right) \left\{ \left(\frac{r}{a}\right)^{-\left(\frac{N_\varphi - 1}{N_\varphi}\right)} - \left(\frac{R}{a_s}\right)^{-\left(\frac{N_\varphi - 1}{N_\varphi}\right)} \left(\frac{R}{r}\right)^{\left(\frac{N_\varphi + 1}{N_\varphi}\right)} \right\} \tag{D-18}$$

[*]D. C. Drucker and W. Prager, "Soil Mechanics and Plastic Analysis on Limit Design," Quarterly of Applied Mathematics, Vol. 10, No. 2, pp. 157-165 (July 1952).

Substituting this expression for ε_{rp} into Eq. (D-17) we obtain the strains ε_r and ε_θ in the plastic zone in terms of the source pressure and radius, the distance from the source, and the soil material properties. The radial displacement in the plastic zone is then given by

$$u = r \, \varepsilon_\theta \qquad\qquad (D-19)$$

Appendix E

STRESS, STRAIN, AND DISPLACEMENT AROUND A PRESSURIZED ELLIPTICAL HOLE

Analytical Solution

To estimate elastic response around the array, consider the static plane strain problem of a pressurized elliptical hole with major radius a and minor radius b as shown in Figure E-1. The ellipse is defined in the z plane by

$$\frac{x^2}{a^2} + \frac{y^2}{b^2} = 1 \tag{E-1}$$

The ellipse and the region around it is mapped from a circle and the region within it by the function

$$z = R(\frac{1}{\zeta} + m\zeta), \quad R > 0, \quad |\zeta| \le 1 \tag{E-2}$$

where

$$z = x + iy = re^{i\theta}, \quad \zeta = \xi + i\eta = \rho e^{i\gamma} \tag{E-3}$$

$$R = \frac{a + b}{2}, \quad m = \frac{a - b}{a + b} \tag{E-4}$$

As γ ranges from 0 to $-\pi/2$, θ ranges from 0 to $+\pi/2$, as shown in the figure. The stress functions for a pressurized ellipse are[*,†]

$$\Phi_1(\zeta) = - PRm\zeta \tag{E-5}$$

$$\Psi_1(\zeta) = - PR\left[\zeta + \frac{m\zeta(\zeta^2 + m)}{1 - m\zeta^2}\right] \tag{E-6}$$

---

[*] I. S. Sokolnikoff, Mathematical Theory of Elasticity (McGraw-Hill, New York, 1956), pp. 292-295.

[†] Since response is entirely elastic, the pressure P is associated with the elastic pressure P_e discussed in Section IV.

E-1
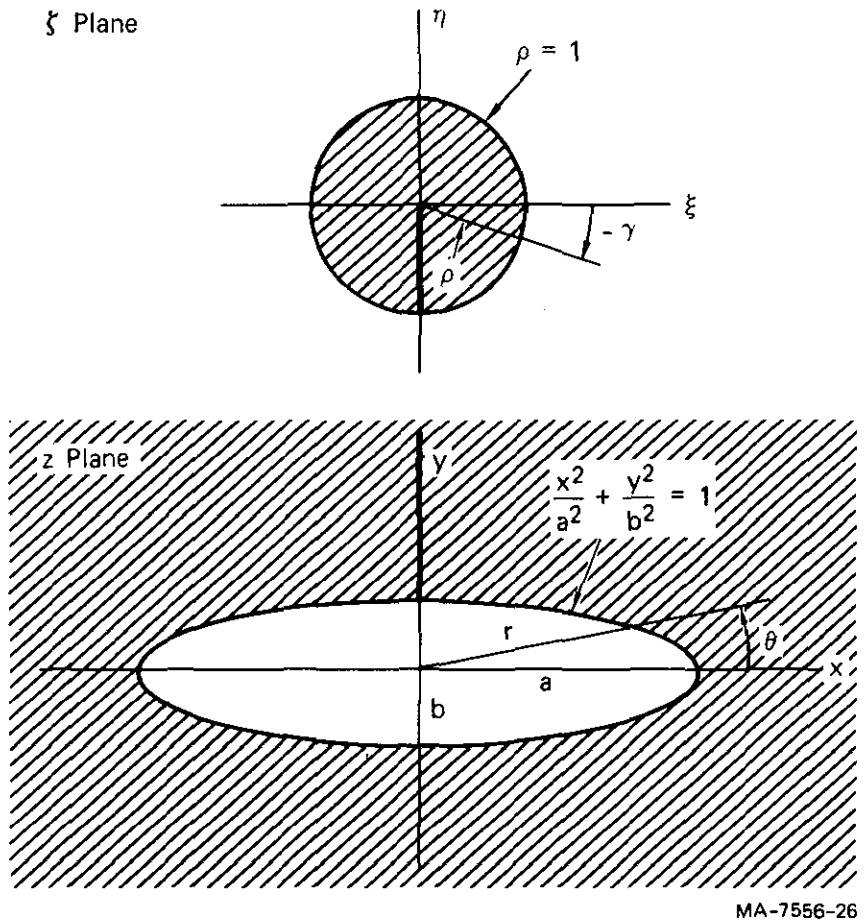
FIGURE E-1   MAPPING OF CIRCULAR AREA ONTO AREA EXTERNAL
TO AN ELLIPTICAL HOLE

Stresses and displacements are found from the general formulas:

$$\sigma_x + \sigma_y = 4\mathcal{R}[\Phi'(z)] \tag{E-7}$$

$$\sigma_x - \sigma_y + 2i\tau_{xy} = 2[\bar{z}\Phi''(z) + \Psi'(z)] \tag{E-8}$$

$$2\mu(u_x + iu_y) = \kappa\Phi(z) - z\overline{\Phi'(z)} - \overline{\Psi(z)} \tag{E-9}$$

where

$$2\mu = \frac{E}{1 + \nu} \; , \quad \kappa = 3 - 4\nu \quad \text{(plane strain)} \tag{E-10}$$

and

$$\Phi[z(\zeta)] \equiv \Phi_1(\zeta) \; , \qquad \Psi[z(\zeta)] \equiv \Psi_1(\zeta) \tag{E-11}$$

Therefore,

$$\Phi'(z) = \frac{d\Phi_1}{d\zeta}\frac{d\zeta}{dz} = \frac{-\zeta^2}{R(1-m\zeta^2)} \; \frac{d\Phi_1}{d\zeta} \tag{E-12}$$

and so forth.

Substitution of the stress functions in Eqs. (E-5) and (E-6) into Eqs. (E-7) and (E-8) gives the desired expressions for stresses:

$$\sigma_y + \sigma_x = \frac{4P}{D}(f \cos 2\gamma - f^2) \tag{E-13}$$

$$\sigma_y - \sigma_x = \frac{2P}{D^3}\left\{-3Mf^2(1 - f^2) + [Mf(1 - f^4) + 4f^2(1 - f^2)] \cos 2\gamma \right.$$
$$\left. +[Mf^2(1 - f^2) - 2f(1 - f^4)] \cos 4\gamma\right\} \tag{E-14}$$

$$\tau_{xy} = \frac{P}{D^3}\left\{[MF(1 - 6f^2 + f^4) + 4f^2(1 + f^2)] \sin 2\gamma \right.$$
$$\left. +[Mf^2(1 + f^2) - 2f(1 + f^4)] \sin 4\gamma\right\} \tag{E-15}$$

in which

$$D = 1 - 2f \cos 2\gamma + f^2, \qquad f = m\rho^2, \qquad M = \frac{1 + m^2}{m} \qquad \text{(E-16)}$$

Displacements are similarly found, by using Eq. (E-9):

$$u_y = \frac{PR}{2\mu} \left\{ - \left[(1 + 2m)\rho + mQ(1 + \rho^2 + m\rho^2) \right] \sin \gamma + Q \sin 3\gamma \right\} \qquad \text{(E-17)}$$

$$u_x = \frac{PR}{2\mu} \left\{ \left[(1 - 2m)\rho + mQ(1 + \rho^2 - m\rho^2) \right] \cos \gamma - Q \cos 3\gamma \right\} \qquad \text{(E-18)}$$

in which

$$Q = m\rho(1 - \rho^2)/D \qquad \text{(E-19)}$$

Numerical Results

It is convenient to calculate these quantities along ρ, γ contours. These map onto ellipses (ρ = constant) and hyperbolas (γ = constant) in the z plane, given in parametric form by expanding Eq. (E-1) as follows:

$$\frac{x}{R} = (m\rho + \frac{1}{\rho}) \cos \gamma, \qquad \frac{y}{R} = (m\rho - \frac{1}{\rho}) \sin \gamma \qquad \text{(E-20)}$$

Tabulations of z-contours, displacements, and stresses for m = 0.8 are given in Tables E-1, E-2, and E-3. The displacement data are plotted in the z-plane in Figure E-2. Also shown in Figure E-2 are the locations of the accelerometers in the array tests reported in the main text. These are plotted by taking the end of the ellipse, x/R = 1.8, to coincide with the 15-ft half-length of the array. Corresponding dimensions in feet are given as a second set of coordinates in the figure.

Displacement in the y direction is plotted in Figure E-3 as a function of distance y from the array for several contours γ = const. A structure to be tested would be placed at about y/R = 0.8 (about 7 ft for the 30-ft array). Contours corresponding to a 10 x 10 ft structure placed with its closest side at this range are drawn in Figures E-2 and E-3. The centerline of the structure lies on the γ = 0° curve, as shown in both figures. Either side of the structure is on the dashed contour in Figure E-3. The front and rear of the structure are the lines at y = 7 and 17 ft. The closeness of centerline and side contours in Figure E-3 shows

E-4

Table E-1   ELLIPSE/HYPERBOLA CONTOURS FOR m = 0.8

γ \ ρ		1	0.9	0.8	0.7	0.6	0.5	0.4	0.3	0.2
0°	x/R	1.80	1.83	1.89	1.99	2.15	2.40	2.82	3.57	5.16
	y/R	0	0	0	0	0	0	0	0	0
-15°	x/R	1.74	1.77	1.83	1.92	2.07	2.32	2.72	3.45	4.98
	y/R	0.05	0.10	0.16	0.22	0.31	0.41	0.56	0.80	1.25
-30°	x/R	1.56	1.59	1.64	1.72	1.86	2.08	2.44	3.09	4.47
	y/R	0.10	0.20	0.31	0.43	0.59	0.80	1.09	1.55	2.42
-45°	x/R	1.27	1.29	1.34	1.41	1.52	1.70	1.99	2.53	3.65
	y/R	0.14	0.28	0.43	0.61	0.84	1.13	1.54	2.19	3.42
-60°	x/R	0.90	0.92	0.95	0.99	1.07	1.20	1.41	1.79	2.58
	y/R	0.17	0.30	0.53	0.75	1.03	1.39	1.89	2.68	4.19
-75°	x/R	0.47	0.47	0.49	0.51	0.56	0.62	0.73	0.92	1.34
	y/R	0.19	0.38	0.59	0.84	1.15	1.55	2.11	2.99	4.68
-90°	x/R	0	0	0	0	0	0	0	0	0
	y/R	0.20	0.39	0.61	0.87	1.19	1.60	2.18	3.09	4.84

Table E-2   DISPLACEMENTS AROUND PRESSURIZED ELLIPSE FOR m = 0.8
(Normalized to PR/2μ)

γ \ ρ		1	0.9	0.8	0.7	0.6	0.5	0.4	0.3	0.2
0°	u_x	−0.60	−0.62	−0.57	−0.51	−0.45	−0.38	−0.30	−0.23	−0.15
	u_y	0	0	0	0	0	0	0	0	0
−15°	u_x	−0.58	−0.43	−0.36	−0.32	−0.28	−0.24	−0.20	−0.15	−0.10
	u_y	0.67	0.51	0.38	0.28	0.21	0.16	0.12	0.09	0.06
−30°	u_x	−0.52	−0.32	−0.18	−0.08	−0.02	0.00	0.01	0.01	0.01
	u_y	1.30	1.17	1.00	0.82	0.65	0.50	0.37	0.26	0.17
−45°	u_x	−0.42	−0.25	−0.09	0.03	0.12	0.16	0.17	0.15	0.11
	u_y	1.84	1.72	1.56	1.38	1.17	0.95	0.74	0.54	0.35
−60°	u_x	−0.30	−0.17	−0.05	0.06	0.14	0.19	0.21	0.20	0.15
	u_y	2.25	2.14	1.99	1.82	1.61	1.37	1.11	0.84	0.56
−75°	u_x	−0.16	−0.09	−0.02	0.04	0.09	0.12	0.14	0.13	0.10
	u_y	2.51	2.40	2.26	2.08	1.89	1.65	1.37	1.06	0.73
−90°	u_x	0	0	0	0	0	0	0	0	0
	u_y	2.60	2.49	2.35	2.19	1.99	1.75	1.47	1.15	0.79

Table E-3 STRESSES AROUND PRESSURIZED ELLIPSE FOR m = 0.8
(Normalized by Internal Pressure P; Tension is Positive)

γ	ρ	1	0.9	0.8	0.7	0.6	0.5	0.4	0.3	0.2
0°	σ_x	-1.00	2.46	1.77	1.17	0.76	0.48	0.28	0.15	0.06
	σ_y	17.00	4.91	2.43	1.41	0.86	0.52	0.30	0.16	0.07
	τ_{xy}	0	0	0	0	0	0	0	0	0
-15°	σ_x	1.42	0.60	0.05	0.03	0.09	0.11	0.09	0.06	0.03
	σ_y	-0.58	1.30	1.88	1.54	1.05	0.66	0.38	0.20	0.08
	τ_{xy}	-1.00	-1.47	-0.70	-0.14	+0.06	0.10	0.08	0.05	0.02
-30°	σ_x	-0.17	0.14	0.07	-0.12	-0.22	-0.20	-0.14	-0.08	-0.03
	σ_y	-0.97	-0.64	-0.10	+0.34	0.52	0.49	0.36	0.21	0.10
	τ_{xy}	-0.16	-0.56	-0.78	-0.69	-0.46	-0.24	-0.10	-0.03	-0.01
-45°	σ_x	-0.57	-0.27	-0.10	-0.07	-0.11	-0.15	-0.15	-0.11	-0.06
	σ_y	-0.99	-0.92	-0.73	-0.46	-0.19	-0.00	+0.09	0.09	0.05
	τ_{xy}	-0.05	-0.21	-0.40	-0.52	-0.52	-0.43	-0.29	-0.16	-0.07
-60°	σ_x	-0.71	-0.47	-0.26	-0.13	-0.06	-0.04	-0.04	-0.04	-0.02
	σ_y	-1.00	-0.97	-0.90	-0.78	-0.60	-0.41	-0.24	-0.12	-0.04
	τ_{xy}	-0.02	-0.09	-0.19	-0.29	-0.35	-0.36	-0.30	-0.21	-0.10
-75°	σ_x	-0.76	-0.55	-0.36	-0.18	-0.05	0.02	0.05	0.05	0.03
	σ_y	-1.00	-0.99	-0.96	-0.89	-0.79	-0.64	-0.47	-0.29	-0.14
	τ_{xy}	-0.01	-0.03	-0.08	-0.13	-0.17	-0.19	-0.18	-0.14	-0.07
-90°	σ_x	-0.78	-0.58	-0.38	-0.21	-0.06	+0.04	0.09	0.09	0.05
	σ_y	-1.00	-0.99	-0.97	-0.92	-0.84	-0.71	-0.54	-0.35	-0.18
	τ_{xy}	0	0	0	0	0	0	0	0	0
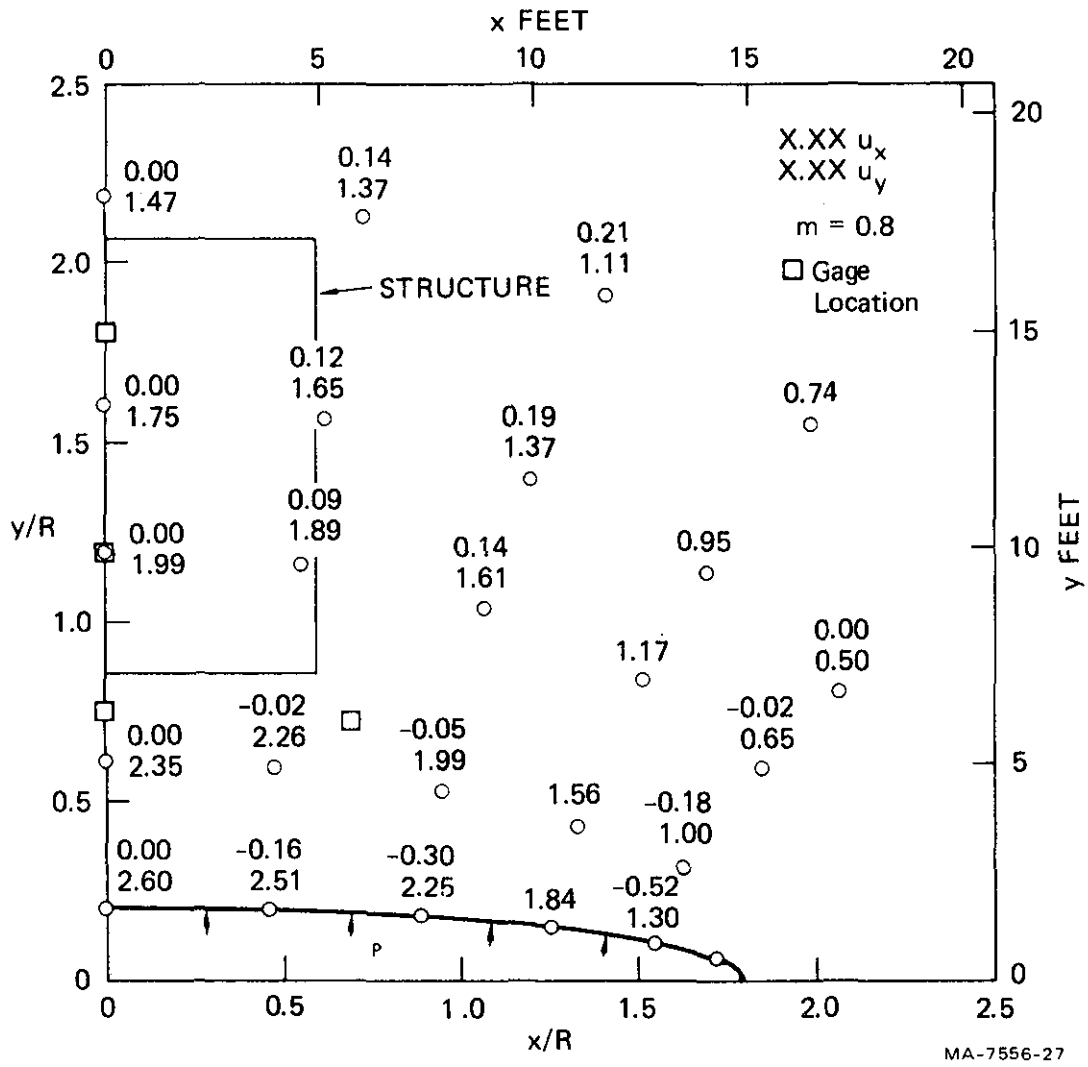
FIGURE E-2   DISPLACEMENTS AROUND PRESSURIZED ELLIPSE
(Normalized to PR/2μ)

MA-7556-27
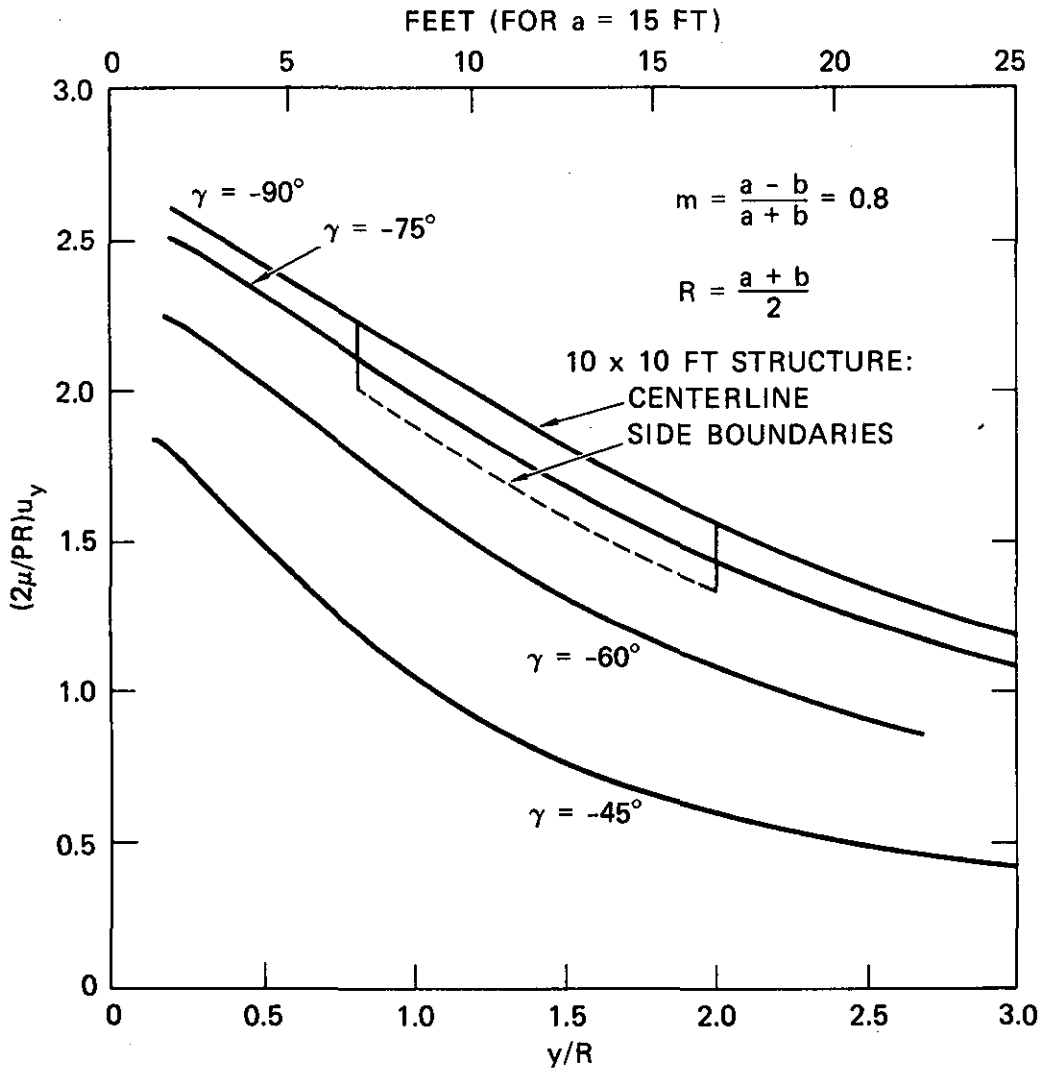
FIGURE E-3   DISPLACEMENT ALONG y-AXIS VERSUS y

that displacements are very nearly uniform across the width of the structure. The largest variation in displacement is from front to rear. On the centerline, the normalized displacement is 2.24 at the front and 1.55 at the rear, a difference of 31% of the larger value. This difference is caused by the soil strain under the action of the loading pressure P; that is, by the strain corresponding to the stresses in Table E-3. This soil strain will induce compressive stress in the structure and perhaps some slipping and certainly shearing in the soil as the soil and structure interact.

This situation is similar to, but not identical with, the soil strain and displacement relation for a P-wave incident on the structure. In both instances, the force that moves the soil is from normal stress. By contrast, for an S-wave induced by base rock motion, displacements are constant in horizontal planes so there is no variation across the structure. In this instance the force that moves the soil is from shear stress, so that for any finite imbedment depth of the structure, stresses and perhaps slipping will result because of the strain change between the soil free-field and the structure. All these soil-structure interactions are a subject of great concern for earthquake engineering of structures.

The difference between the soil strain for the array simulation and for a P-wave is in the time phasing between displacement and strain. If motion in both consisted entirely of free wave motion, the phasing would be the same for both. The difference in phasing is a maximum when the simulation motion is produced by a quasi-static stress system (i.e., when the array dimension is small compared with the wavelength of motion frequency, as assumed for simplicity in this appendix). In this case, the displacement and strain are in phase in the simulation because all quantities increase and decrease together in a quasi-static manner. For a P-wave, the displacement u_y and strain ε_y are not in phase because stress, and hence strain, is equal to the wave impedance ρc (density times wave velocity) times the particle velocity $\dot{u}_y$. Thus, for a steady sinusoidal wave train, the strain and particle velocity lag 90° behind the displacement.

For many frequencies of interest, the magnitude of the soil strain in the array simulation is in the same range as that in a P-wave train. In the extreme case of quasi-static motion, the displacement and strain can be related by the pressurized ellipse calculation. Near the ellipse on the minor axis, where a structure would be placed, the displacement, from Eq. (E-17) with $\gamma = -90°$ and $\rho = 1$, is

$$u_y = (1 + 2m) \frac{PR}{2\mu} = 2.6 \frac{PR(1 + \nu)}{E} \tag{E-21}$$

The strain, from Hooke's law in plane strain and the stresses in Table E-3, is

$$\varepsilon_y = \frac{1}{E}[(1 - \nu^2)\sigma_y - \nu(1 + \nu)\sigma_x]$$

$$= \frac{1}{E}[(1 - \nu^2)P - \nu(1 + \nu)(0.78P)] \tag{E-22}$$

with compressive strain now taken positive. The ratio is

$$\frac{\varepsilon_y}{u_y} = \frac{(1 - \nu^2) - \nu(1 + \nu)(0.78)}{2.6(1 + \nu)R} = \frac{1 - 1.78\nu}{2.6R}$$

$$= 0.22/R \approx 0.86/L \tag{E-23}$$

in which we have taken $\nu = 1/4$ and $R = (a + b)/2 \approx a/2 = L/4$. For the array tests described in the main text, the array length is $L = 30$ ft so that the soil strain is $\varepsilon_y/u_y = 0.86/30$ ft $= 0.029$ per foot of displacement.

For a P-wave train of frequency $\omega = 2\pi f$ (again neglecting the free surface, as in the ellipse solution) the displacement is

$$u_y = U \sin \omega \left(\frac{y}{c} - t\right) \tag{E-24}$$

in which U is the peak displacement and c is the dilational wave velocity.

E-11

The strain is

$$\varepsilon_y = \frac{du_y}{dy} = \frac{\omega}{c} \cdot U \cos \omega \left(\frac{y}{c} - t\right) \qquad (E-25)$$

This demonstrates the previous statement that the strain lags the displacement by 90°. The ratio of peak strain to peak displacement is

$$\frac{|\varepsilon_y|}{|u_y|} = \frac{\omega}{c} \qquad (E-26)$$

In the experiments, the observed wave speed was c = 1000 fps. For the dominant frequency of 8.7 Hz in the experiments, a P-wave strain-to-displacement ratio would therefore be

$$\frac{|\varepsilon_y|}{|u_y|} = \frac{2\pi(8.7 \text{ Hz})}{1000 \text{ fps}} = 0.055 \text{ per foot} \qquad (E-27)$$

This is within a factor of two of the 0.029 per foot ratio for the ellipse calculation.

These ratios would differ for other frequencies, of course, but at the 30-ft array size, 8.7 Hz is near the central frequencies of interest for a 1/3-scale test. For larger scale experiments the central frequency would be lower and the array length would be longer by the same amount. Eqs. (E-23) and (E-26) therefore show that the strain-to-displacement ratios for both the array and a P-wave would be reduced by the same amount. We conclude that the ratios from the array simulation and from P-waves will always be of the same order in amplitude—the main difference is in phase. As the frequency is increased, the loading ellipse becomes large compared with the wavelength and the simulation motion approaches that of a P-wave in both phase and amplitude.

Limitations of the Elastic Ellipse Idealization

The plane strain pressurized ellipse analysis is intended to give a first order interpretation of array response in the limit as the pulse duration becomes long compared with the wave transit time across the

length of the array. The calculation neglects (1) dynamic response, important for higher frequencies, (2) the presence of the soil free surface, (3) the finite depth of the array, and (4) inelastic soil response. More complete theoretical analyses that treat all of these shortcomings, both individually and in appropriate groups as theoretical complexity is increased, are being performed with a finite element elastic-plastic code.

An indication of the need to include inelastic response is seen by inspection of the stresses in Table E-3. In the region of high stress concentration near the ends of the ellipse (small γ, ρ near unity), the stresses are several times larger than the internal pressure P. These stresses will induce a plastic zone that will change the shape of the elastic-plastic boundary from the ellipse assumed here, and will also introduce shear stresses at the boundary. Nevertheless, we expect that the net motion and stresses in the region in which a structural test model would be placed will be similar to the estimates here because the structure test region is remote from these plastic zones.